High-Sensitivity Field Emission Magnetometers and other applications of Field Emission Technologies

Paul J. French

Department of Electronic and Electrical Engineering
University College London

A thesis submitted to University College, University of London for the degree of Doctor of Philosophy

2008

UMI Number: U591244

All rights reserved

INFORMATION TO ALL USERS
The quality of this reproduction is dependent upon the quality of the copy submitted.

In the unlikely event that the author did not send a complete manuscript
and there are missing pages, these will be noted. Also, if material had to be removed,
a note will indicate the deletion.

UMI U591244
Published by ProQuest LLC 2013. Copyright in the Dissertation held by the Author.
Microform Edition © ProQuest LLC.
All rights reserved. This work is protected against
unauthorized copying under Title 17, United States Code.

ProQuest LLC
789 East Eisenhower Parkway
P.O. Box 1346
Ann Arbor, MI 48106-1346

Abstract

The feasibility and development of a field emission based anisotropic vector magnetometer is presented. Within this scope current magnetic sensing technology is investigated and compared. The advantages of, and need for, a field emission based magnetic sensor are then discussed. Background theory, simulation, fabrication, testing, and future developments of field emission magnetometers are presented. The possible applications of field emission to other technologies are also investigated.

The magnetic sensing device presented uses a sharp field emitting tip with a radius of the order of 100nm which is fabricated using standard silicon processing techniques on highly n-doped silicon. Under a vacuum level of 10^{-6} mBar and at room temperature, a potential applied to a surrounding gate electrode extracts from this tip a beam of electrons which is incident upon two separate anode electrodes. In the absence of an external magnetic field the electron current incident on each of these two electrodes is equal, while in the presence of a magnetic field the Lorenz force skews the beam towards one of the electrodes, resulting in a differential current which is proportional to the magnetic field.

Acknowledgements

I would like to thank my supervisors Dr. Tony Kenyon and Dr. David Garner for taking me on as one of their students, and for their dedicated supervision and guidance during my time at UCL. My sincerest thanks also go to Dr. Hubert Blanchard of LEM for making the CASE-studentship possible and for his guidance and practical assistance.

In addition I am grateful to Mir Mokhtari and Tony Blackburn of INNOS for processing our devices. I am indebted to Trevor and Jim in our workshop for building the testing apparatus; and to Kevin Lee of LCN for bonding our devices and providing advice on device processing. I am also appreciative of the help, suggestions and support from good friends Alastair Smith of Cambridge University and David Johnston, formerly of Essex University.

For my Mother

Love, Light and Happiness

Contents

High-Sensitivity Field Emission Magnetometers and other applications of Field Emission Technologies

Abstract i

Chapter 1. Introduction 1

1.1. Outline of thesis 1

1.2. Summary review of magnetic sensor technology 3

1.3. The field emission magnetometer 13

1.4. Alternative field emission magnetometer designs 20

1.5. References 22

Chapter 2. Field emission 26

2.1. Theoretical description 26

2.1.1. The Fowler Nordheim equation 28

2.1.2. Determination of tip radius 34

2.2. Factors governing device operation 43

2.2.1. Vacuum requirements 43

2.2.2. Stochastic processes: Ion bombardment and cathode tip changes 45

2.3. Applications of field emission 53

2.4. References 56

Chapter 3. Experimental setup and Magnetometer Evolution 61

3.1. Experimental setup 61

3.2. Fabrication overview 66

3.3. Failure analysis and device improvement 70

3.3.1. Fabrication issues 74

3.3.2. Cathode tip structure and stability 77

3.4. References 86

Chapter 4. Simulations **90**
4.1. Overview of Device Optimisation 90
4.2. Supporting Numerical Simulations 91
4.2.1. Laplace equation for crossed electric and magnetic fields 91
4.2.2. Electron distribution and ray tracing 95
4.3. Analytical Model and Preliminary Optimisation 100
4.3.1. Electron beam width under quiescent magnetic fields 102
4.3.2. Analytical calculation of the Lorentz Force Equation 109
4.4. Sensitivity and Range 113
4.5. References 116

Chapter 5. Experimental Results and Discussion **118**
5.1. Demonstrating field emission 118
5.2. Maximising anode current under quiescent magnetic fields 123
5.3. Demonstrating magnetic field detection 127
5.4. References 132

Chapter 6. Conclusions **133**
6.1. Achievements of this work 133
6.2. Future work 137
6.3. References 148

Appendix A. **150**
A.1. Matlab scripts 150
A.2. Publications arising from this thesis 153

Chapter 1

Introduction

1.1. Outline of thesis

Chapter one gives a literature review of current magnetic sensor technology giving the principle operation of these devices. A gap in the market for a vacuum magnetic sensor is presented and the two types of vacuum magnetic sensor are described: lateral and vertical designs. This thesis concentrates on lateral designs for ease of construction and ease of integration with standard CMOS processing [1 - 3].

Chapter two discusses the theoretical description of field emission, basing the theory presented on the Fowler-Nordheim model of field emission, about which there is a large volume of literature [4 - 9]. The Fowler Nordheim equation is given with a description of *Fowler Nordheim coordinates*, allowing for calculation of tip cathode emitter radius which is compared against electron micrograph images of devices for conformation of apex sizes.

The hardware infrastructure, fabrication process and limits of fabrication are given in chapter three. Device evolution between two generations of devices manufactured over this project is presented, highlighting fabrication and device improvements over the course of the project, and ending with a short study on cathode stability, considered the most important aspect of the device.

The simulations in chapter four show the development and optimisation of a quantitative model of the devices. The electromagnetic package SimIon [10] solves the underlying electrostatics and electron trajectories within the device over different magnetic field strengths. Ballistic electron trajectories are modelled in the action stage of the vacuum magnetic sensor, where the device is simulated under zero and non-zero magnetic fields.

Parameter optimisation follows to ensure maximum sensitivity, range and resolution, with minimum power consumption, a high degree of linearity and little or no scaling.

Experimental and theoretical results are compared in chapter five, with field emission demonstrated with emphasis on emission stability and uniformity over time under zero magnetic fields. Device magnetic sensitivity is also shown, with differential anode currents measured for an applied magnetic field. This recorded device sensitivity is of the highest order for a lateral field emission magnetometer of its type.

The conclusion and ideas for future work are presented in chapter six, where it is argued that the project is a success, though requires more work if it is to be considered for industrial exploitation.

1.2. Summary review of magnetic sensor technology

The intention here is to review the foundation of how common magnetometers operate, with emphasis on how the vacuum magnetic sensor may fill a gap in the market: Vector or scalar devices, range, sensitivity, accuracy, resolution, offset, size, temperature dependence, cost, and compatibility with silicon VLSI are the primary factors in current magnetometer technologies. A comparison of the most common magnetic sensors available on the market is shown in figure 1.1, where these primarily operate on a few principles and have been placed in order of increasing sensitivity: quantum mechanical effects (SQUID, Optically-Pumped and Nuclear procession), Fiber-Optic, Search-Coil (or Fluxgate), Magnetoresistance (which can further be classified into two groups: ferromagnetic and semiconductor magnetoresistors), the Hall Effect, and field emission technologies.

Further classifications of these devices are defined by arbitrary application-ranges that devices operate within. Such ranges typically considered are *Low Field (smaller than 100 pT)*, *Medium Field or Earth Field (100 pT to 1 mT)*, and *High Field (greater than 1 mT)*.

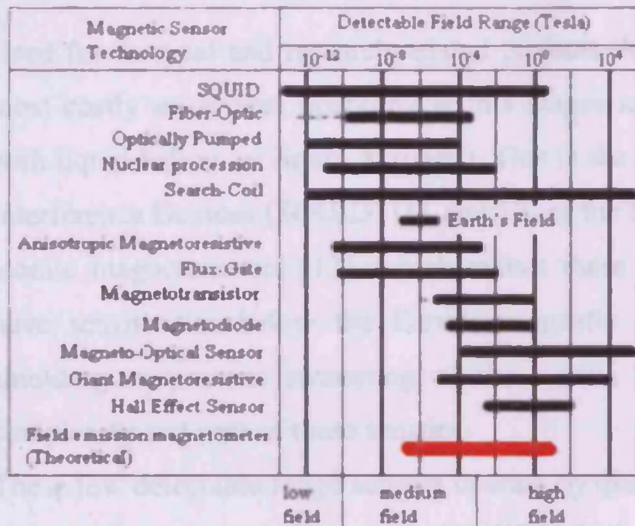

Figure 1.1. Common magnetic field detection technologies, from [11].

As seen from above, the range for theoretical field emission magnetometer indicates that these devices operate at the medium to high range of the magnetic fields, though they are potentially the lowest in cost, rivalling alternative magnetometers that operate at the same ranges. Calculations for the theoretical upper limit range are shown in section (1.3) while the lower limit on theoretical range is based on conservative estimates of what electrical currents may be sensed without being lost in noise. The achievable magnetic field range of the device involves an optimisation of device geometry and input bias voltages. For this reason the field range shown is an estimate of the magnetic field range of this magnetometer, with the possibility of increasing this range by further research.

Although not shown in the above figure, the field emission magnetometer also has the potential to be the smallest of the devices listed, and is a vector sensing magnetometer that is compatible with silicon VLSI, unlike the numerous sensors listed. The reasons for this will become apparent within the research that follows.

Low Field Magnetometers (B < 100 pT)

Used for medical and research-related projects, low field magnetometers tend to be the most costly as devices operating at this magnetic field range require cooling (typically with liquid helium or liquid nitrogen). This is the case for the Superconducting Quantum Interference Devices (SQUID) [11 and 12] or the Spin Exchange Relaxation Free (SERF) atomic magnetometers [13], which makes these devices bulky. Because these devices have sensitivities below the Earth's magnetic field they typically require magnetic shielding to prevent swamping of the signal, further adding to the required bulk, complexity and cost of these sensors.

These low detectable range sensors operate by quantum mechanical effects. Such devices include: the vector sensing sensor SQUID, which operates by a signal's phase difference from two Josephson junctions created by superconductors [11]; the SERF atomic magnetometers that rely on measuring the Larmor precession of spin-polarized atoms within a magnetic field, producing the gyromagnetic ratio for the material used [13][1]; the fiber optic magnetometers that use mechanical vibration due to the Lorentz force on an optical reflective surface to superpose two or more laser beams (interferometric magnetic detection) [14]. Optically-Pumped magnetometers operate by the Zeeman Effect, where applied magnetic fields change the spectra of atomic energy levels [15]. Nuclear precession devices operate by making use of nuclear magnetic resonance of the atom's nucleus (typically hydrogen is used), where a polarizing current in an inductor creates a magnetic field around a hydrogen-rich fluid causing the hydrogen protons to align with the magnetic field. After the polarizing current is switched off the spinning protons realign with the Earth's magnetic field. It is this precession of proton spin that induces a small exponentially decaying AC signal in the inductor coil, whose frequency is proportional to the flux of any external magnetic field [16]

The final low field magnetometer considered is Search-Coil (or Fluxgate) [11 and 17], which operate on Faraday's law of induction where a voltage is produced that is proportional to a magnetic field applied to a coil of wire. The sensitivity of this sensor is

[1] SERF atomic magnetometers are not mentioned within figure 1.1 because they have not yet been established, being only being recently developed (2002). Recent research has, however, indicated that the sensitivity of SERF magnetometers has surpassed SQUID devices, as reported in Nature [13].

dependent upon numerous factors such as the area of coil, number of turns, the permeability of core material, and the rate change of magnetic flux through the coil, thus limiting these devices to AC magnetic fields or static fields where the sensor is moved through the magnetic field [11]. The Fluxgate is a variant of the search coil consisting of measurement and reference (or drive) coils wrapped around a common ferromagnetic core [11]. A reference signal is driven through the reference coil at a given frequency that causes the core to oscillate between saturation points. The measurement coil picks up the reference signal plus any external magnetic field present. Comparison and filtering of the two signals allows the external magnetic field to be measured. Although inexpensive and wide ranging, major issues with these devices are susceptibility to AC magnetic fields, large size, and performance further limited by temperature dependence and the electronic components used.

Medium Field or Earth Field Magnetometers (100 pT < B < 1 mT)

Typically used for navigation and vehicle detection, medium field sensors tend to be cheaper to use and manufacture than low field sensors, though they often have greater linearity error and poorer resolution than low field sensors.

After Hall sensors [11 p. 11, 17 and 18], magnetoresistors [11 p. 9, 19, and 20] are the most common type of sensor, with two subsections of magnetoresistor: ferromagnetic and semiconductor. Both technologies are based on types of resistor where the resistance changes under the influence of magnetic fields. A Wheatstone bridge configuration is typically used with magnetoresistors allowing for both magnitude and direction along an axis to be measured [17].

Ferromagnetic magnetoresistors

Ferromagnetic magnetoresistors are based on thin ferromagnetic metal (Permalloy) films that exhibit anisotropic resistivity within magnetic fields. When a magnetic field is applied, the internal magnetic moments of the permalloy are aligned with the magnetic field, changing the path of the bias current flowing through the device and hence the resistance.

Although ferromagnetic magnetoresistors are typically found in highly sensitive low field applications, they are prone to flipping after the sensor has been used and it is often necessary to reset the magnetic domain of the Permalloy by the application of a reset/set magnetic field. The application of this can sometimes flip the orientation of the device [11]. This also requires the sensor to have a reset coil which can add considerable bulk to a device.

Semiconductor magnetoresistors

These magnetoresistors are typically constructed from a thin plate or film of high mobility semiconductor and are patterned as a resistive strip. This type of magnetometer is essentially a resistor which is dependent on the angle of the applied magnetic field (hence these are anisotropic) due to the magnetic part of the Lorentz force [11 p. 9] (figure 1.2, left). Although mentioned here, devices that use the Lorentz force typically operate in the higher field range and are discussed further in the next section. The magnetic part of the Lorentz force causes deflection of the charge carriers relative to their paths. The micro-deflection of the electrons' free path between collisions is responsible for the increase in resistance with the application of a magnetic field.

Because the reaction of this type of magnetoresistive device is fast to exposure to DC or AC magnetic fields, is small in size (of the order of 5 mm^2 surface area by 2.5 mm in depth), is inexpensive, has a range of typically ± 600 μT (where the Earth's field is typically 50 μT), and low linearity error (approximately 0.1 % of drive voltage) this type of device, specifically the HMC1053 by Honeywell [20] is the most suitable device for a reference sensor throughout this project. Due to the semiconductor magnetoresistor's dependence on temperature (linearity is assured up to 85° C) this device is used at room temperature; specifically this device is used to measure the Earth's magnetic fields for non-biasing testing of the field emission magnetometer.

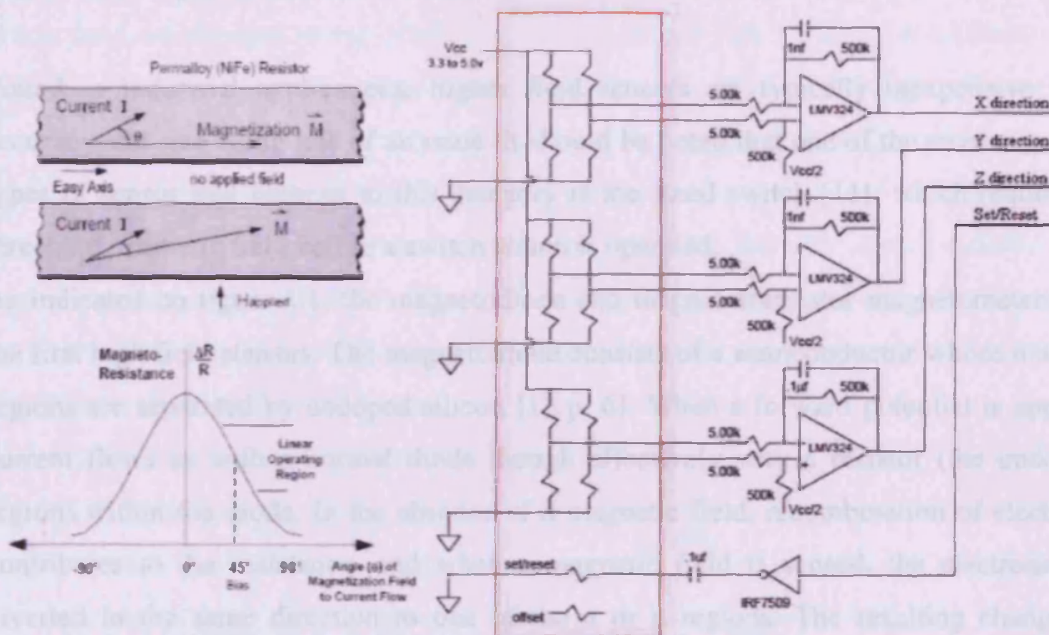

Figure 1.2. The HMC1053 magnetoresistor sensor (right) using the Wheatstone bridge configuration manufactured by Honeywell, from [20]. A seen, the HMC1053 is biased at half the magneto-resistive at fabrication allowing for a full swing over the linear range out put to be made.

High Field Magnetometers (B > 1 mT)

Found in industrial applications, higher field sensors are typically inexpensive with accuracy and size being less of an issue. It should be noted that one of the most common types of sensor that belongs to this category is the Reed switch [11], which requires a threshold magnetic field before a switch action is operated.

As indicated on figure 1.1, the magnetodiode and magnetotransistor magnetometers are the first high field sensors. The magnetodiode consists of a semiconductor whose n and p regions are separated by undoped silicon [11 p. 6]. When a forward potential is applied current flows as with a normal diode though effectively with a resistor (the undoped region) within the diode. In the absence of a magnetic field, recombination of electrons contributes to the resistance, and when a magnetic field is sensed, the electrons are diverted in the same direction to one of the n or p regions. The resulting change in resistance causes an indicating voltage across the diode which is proportional to the magnetic field [11].

The magnetotransistor works similarly to the npn-transistor and the magnetodiode, though this magnetometer has two collectors. As with the magnetodiode, a magnetic fields causes an imbalance in electron flows towards one of the collectors (no magnetic fields causes no difference in collector currents). The voltages created by this imbalance are fed to a differential amplifier, the output of which is proportional to the applied magnetic field [11]. Other established high end magnetometers are the magneto-optical sensor, the giant magnetoresistance and the Hall effect device: The magneto-optical sensor functions by applying the Faraday effect. Light is polarised in the direction of the applied magnetic field, through a medium that exhibits the Faraday effect. The rotation of the polarisation of light will be proportional to the angle of the magnetic field, and it is this rotation of polarisation that is measured to give the magnetic field [11].

Smaller in magnetic field range to the magneto-optical sensor is the giant magnetoresistance device. This functions like anisotropic magnetoresistive devices (in that a change in resistance in an applied magnetic field), except that this type of magnetometer uses the quantum mechanical effect of spin to measure changes in the resistance of a ferromagnetic material.

The most common though most limitind in range is the Hall effect senosr [11, 17 and 18] where the Lorentz force is exploited. This is defined in figure 1.3 as the total force (F in equation 1.1) exerted on a charged particle (e) by the particle accelerating through an electric field, plus the force exerted on the electron in a magnetic field (out of the page, B_z or B as $B_x = B_y = 0$ in all experiments) resulting in the gyration of radius, R of the electron path. As seen from figure 1.3, positively charged particles move clockwise and negatively charged particles move counter-clockwise for a magnetic field pointing out of the plane. Through this text this convention is used and the charged particle considered is the electron which is denoted by e:

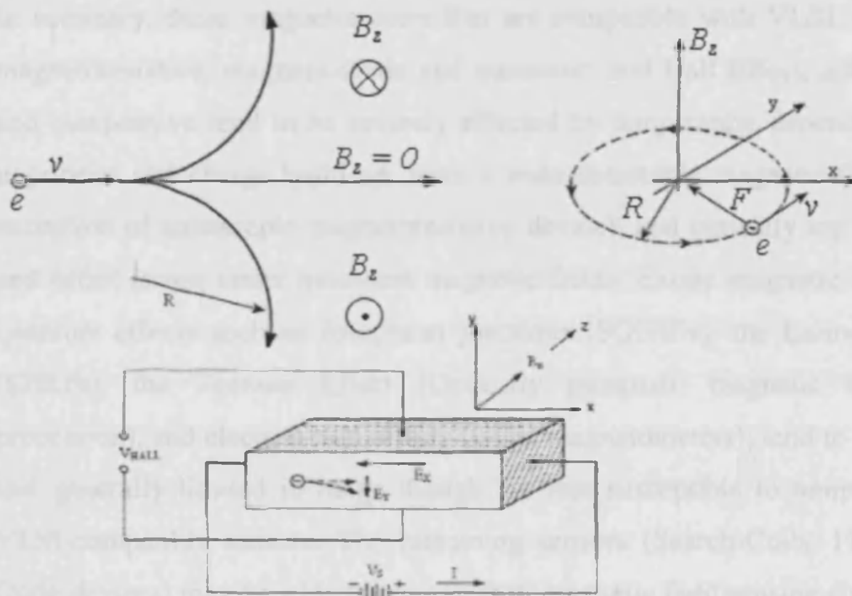

Figure 1.3. The Lorentz force is composed of the force exerted on a charged particle accelerated within an electric field, from [11].

The total force exerted on the particle is given by:

$$F = e(E + vxB\sin\theta) \quad \text{Eq. 1.1}$$

Where F is the force (Newtons), E is the electric field that accelerates the electron (Volts per meter), B is the magnetic field (Tesla) that is applied to the sensing device at an angle θ (it is the angular component equation 1.1 that makes devices that function on the Lorentz force anisotropic), e is the electron charge (Coulombs), and v is the velocity (meters per second).

Also seen in figure 1.3 (bottom) is the Hall magnetotransistor that utilises the Lorentz force by setting up a potential difference across a semiconductor, creating a flow of current. When any magnetic field is present the flow of electrons is deflected to one of the adjacent sides of the device in accordance with equation (1.1) creating a voltage across the adjacent sides (V_{HALL}) which is proportional to the applied magnetic field.

In summary, those magnetometers that are compatible with VLSI, namely, anisotropic magnetoresistive, magneto-diode and transistor, and Hall Effect, although small in size and inexpensive tend to be severely effected by temperature dependence due to doping impurities and charge build up, have a wide detectable magnetic field range (with the exception of anisotropic magnetoresistive device), and typically are susceptible to noise and offset issues under quiescent magnetic fields. Exotic magnetic sensors that rely on quantum effects such as Josephson junctions (SQUIDs), the Larmor precession effect (SERFs), the Zeeman Effect (Optically pumped), magnetic resonance (Nuclear procession), and electron spin effects (Giant magnetometers); tend to be bulky, expensive and generally limited in range though are less susceptible to temperature effects then VLSI-compatible sensors. The remaining sensors (Search-Coils, Fluxgates and Fiber-Optic devices) may be wide ranging in their magnetic field sensing characteristics and are inexpensive, but they are bulky and as such not compatible with VLSI, and are highly temperature dependent (particularly Search-Coils and Fluxgates).

This leaves a gap in the market for an inexpensive, physically small, wide ranging magnetometer relative to temperature and magnetic field ranges, high sensitivity, low noise and offset under zero magnetic fields, and is compatible with VLSI. It is thought that the field emission magnetometer may meet these requirements [3].

1.3. The Field Emission magnetometer

The application of field emission to commercial devices is known as vacuum microelectronics [8 and 9], a relatively new field in which field emission is utilised in a micron-sized device under vacuum. Use of field emission microelectronic magnetometers is very young commercially - at the time of writing no commercial field emission magnetometer exists - though has shown promise on theoretical grounds and in a number of preliminary experiments [25 - 33].

The nature of field emission is considered passive relative to the other types of emission, i.e. thermal, photoelectric and secondary emission where energy is added to a cathode to obtain electrons (hence these methods are active). In field emitting devices electrons are extracted from a surface by quantum tunnelling (a cathode tip) under a high electric field, thus these devices require far less energy than other types of emission [4 - 9]. In the context of the Field Emission magnetometer[2], a gate electrode surrounding a cathode tip causes a high electric field across the gate and cathode. Electrons are extracted by field emission from the cathode tip, the radius of which is of the order of 100 nm and is made from highly n-doped silicon [1 - 3]. These electrons are then accelerated towards a split anode where the current on each of the anodes is equal under quiescent magnetic fields. An external magnetic field across the sensor causes the emitted electron-beam to skew in accordance with the Lorentz force in accordance with equation (1.1), resulting in a differential anode current which is proportional to the magnetic field.

---

2 By analogy to thermionic valve terminology, the emitting tip is referred to as the cathode and the detection stage is referred to as the anode.

The field emission magnetometer, like magnetic sensors based upon the Hall Effect, is dependent upon the Lorentz force. However, within a solid-state Hall effect device, the sensitivity is dependent upon the material properties and is ultimately limited by the carrier mobility [2], whereas in a vacuum microelectronic device, the sensitivity is limited by the degree to which the electron beam is collimated and by the anode-cathode length [1 - 3], both of which are dependent on the geometry of the device. Other advantages of the field emission magnetometer over solid-state devices are: A broad measurement range, where field emission magnetometer geometry dictates measurable range; temperature independence, where, unlike solid-state devices that are reliant on carrier mobility (which changes with temperature), field emission magnetometers measure percentage changes of electrical current within a vacuum, making them indepeandent of temperature; low noise, where because of the nature of solid-state devices, i.e. temperature dependence, mechanical stresses and high power consumption, the field emission magnetometer offers far less noise, and small offset under zero magnetic fields. Because of the nature of the field emission magnetometer fabrication, i.e. the cathode is aligned with the anode as shown in figure 1.4(a), any offset under quiescent magnetic conditions is minimal.

The vacuum magnetic sensor is illustrated in figure 1.4(a), where the sensor is composed of three parts; emitting, action, and detection stages. The emitting stage comprises of the apex of a sharp cathode tip surrounded by the extraction gate. The action stage is the area between the emitting and detection stages, and is the area in which a magnetic field may interact with the emitted electron-beam (indicated by region l in figure 1.4). The detection stage is responsible for attracting electrons, producing a proportional current difference over an applied magnetic field.

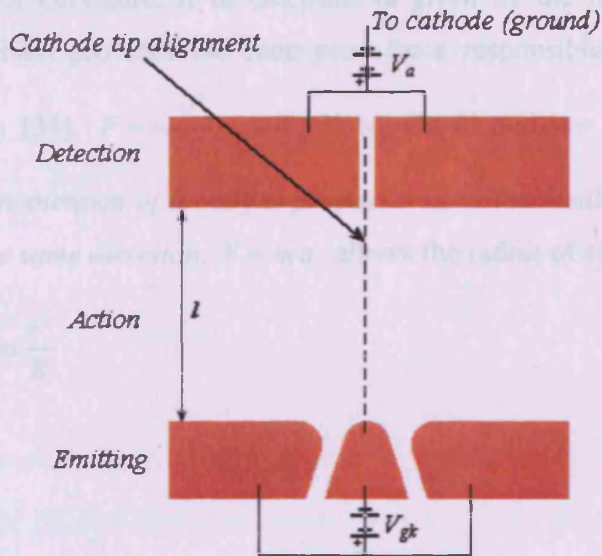

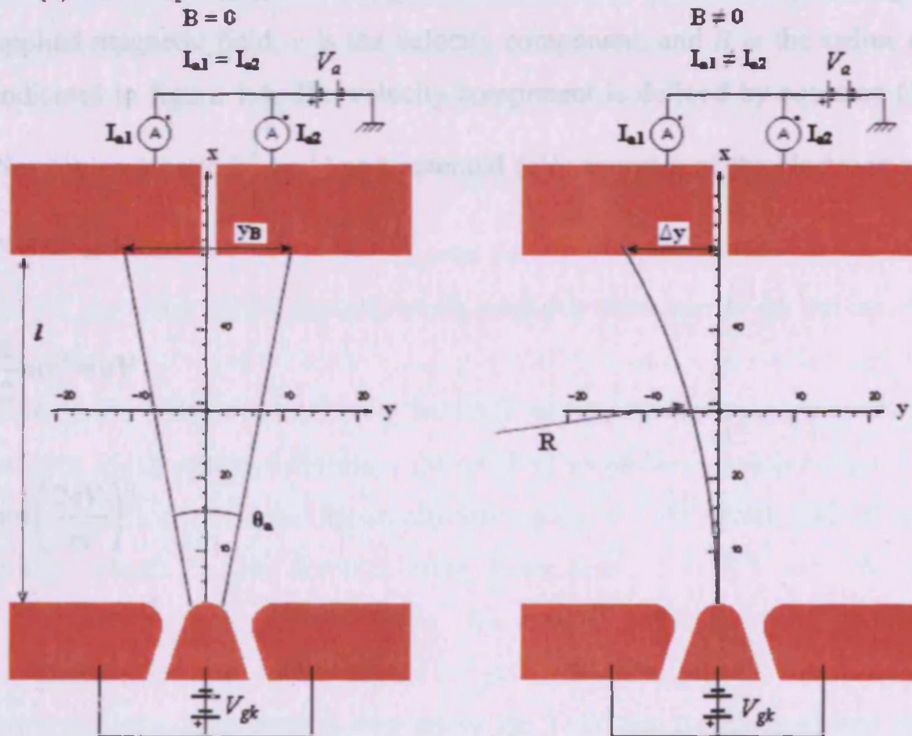

Figure 1.4. No magnetic field results in a balance of anode-currents (left), while a magnetic field present results in a proportional change in anode-currents (right). The cathode is held at ground potential, and the total emitting angle, θ_e, represents the e-beam spread.

Applying equation (1.1) to figure 1.4(b, right side) shows that under a magnetic field B_z, the radius of curvature, R of electrons is given by the magnetic part of the Lorentz equation which provides the centripetal force responsible for R. Equating centripetal acceleration [34], $F = m\frac{v^2}{R}$, with Newton's second law for motion, i.e. *The rate of change of momentum of a body is proportional to the resultant force acting on the body and is in the same direction,* $F = m\,a$, allows the radius of curvature to be found[3]:

$$F = e\,v\,B = m\frac{v^2}{R}$$

$$R = \frac{m\,v}{e\,B} \qquad \text{Eq. 1.2}$$

Where the e and m is the charge and mass of the electron respectively, $B = B_z$ is the applied magnetic field, v is the velocity component, and R is the radius of curvature as indicated in figure 1.4. The velocity component is defined by equation (1.3), where the Newtonian kinetic ($\frac{1}{2}mv^2$) and potential (eV) energies of the electrons are equated and rearranged:

$$\frac{1}{2}mv^2 = eV$$

$$v = \left(\frac{2eV}{m}\right)^{\frac{1}{2}} \qquad \text{Eq. 1.3}$$

[3]Calculated on the assumption that Newtonian mechanics is applicable, and that the external magnetic field is perpendicular to the field emission magnetometer, otherwise the angular part of equation (1) must be included.

Here V is the accelerating voltage between the anode and gate region and is given by, $V = V_a - V_g$, throughout this text. Substituting equation (1.3) into (1.2) gives the radius of curvature in terms of the applied electric field across the anode-gate region:

$$R = \frac{m\,v}{e\,B} = \frac{1}{B}\left(\frac{2mV}{e}\right)^{\frac{1}{2}}$$

Eq. 1.4

$$R \approx \frac{4x10^{-6}\sqrt{V}}{B} \qquad \textit{Metres}$$

As seen, the radius of curvature is proportional to the momentum of the electron $(m\,v)$ and inversely proportional to the sensed magnetic field (B). Equation (1.4) also shows the electron path will become unstable if the electrons radius of curvature is smaller than the anode-cathode distance, i.e. instability results if $R < l$, defining the upper limit of the magnetic field which can be sensed.

In accordance with equation (1.4), substitution of the anode-cathode length for the range allows for the upper range to be calculated, i.e. $B_{ur} \approx \frac{4x10^{-6}\sqrt{V}}{l}$ (S.I. units used in this calculation, otherwise all other figures use eV), which is indicated in figure 1.5 which shows the effect of a large and small magnetic field across the device on the radius of curvature.

Due to the inverse relationship between anode-cathode length and measurable range, smaller anode-cathode distances give rise to larger measurable ranges. Using a typical voltage difference for the anode-cathode region, V = 100 Volts, and the smallest feasible anode-cathode length possible from fabrication[4], l = 0.5 μm, the upper limit of measurable range is approximately[5] $B_{ur} \approx 70$ T, assuming the magnetic field is only applied to the action region and not the gate-cathode region.

Although this upper limit is well above the 2 mT that the experimental apparatus is able to achieve, a linear relationship between device operation and applied magnetic field is

---

[4]Further discussed in chapter 3, fabrication.

[5] This upper limit is used in figure 1.1.

shown in the chapters that follow over the range of magnetic fields that are available in the laboratory.

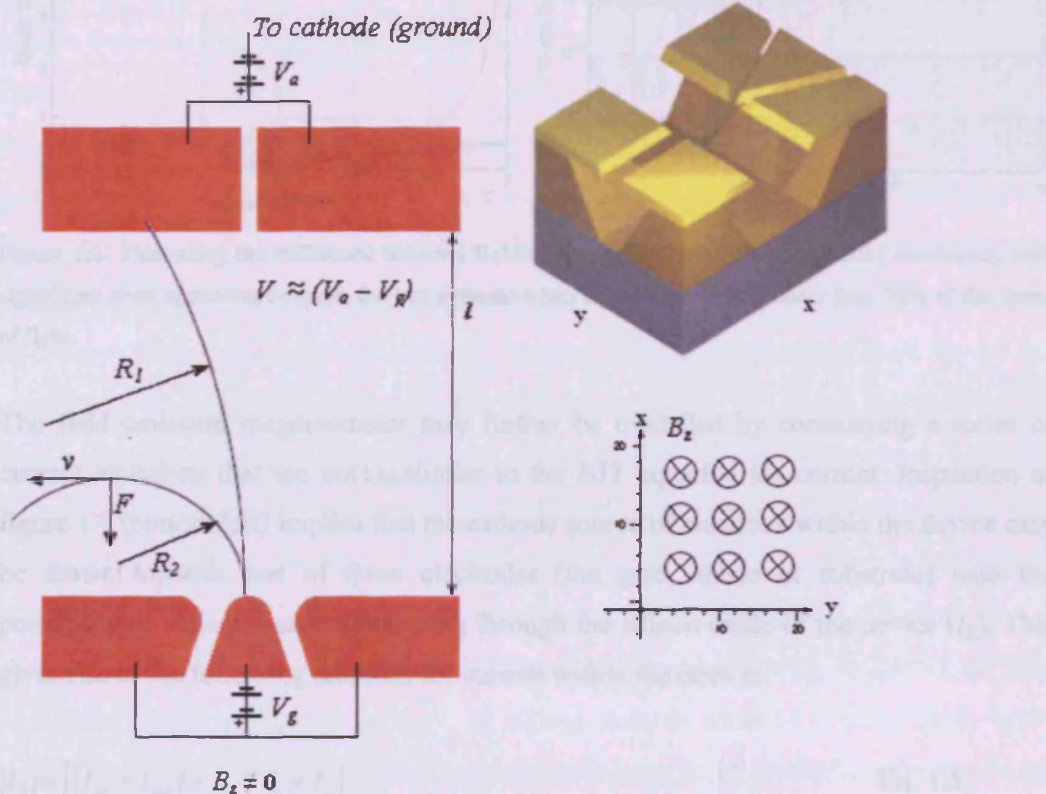

Figure 1.5. Magnetic fields applied to the device result in cycloid electron paths, where larger magnetic fields result in electron orbits that are smaller than the device length (R_2).

In the context of calculating the optimum factors for this magnetometer, figure 1.6 shows electron kinetic energy as a function of velocity and indicates that Newtonian mechanics are sufficient for post-emission electron optics presented here [17]. As expected the relativistic electrons require an infinite amount of energy at the speed of light, *c*, while the Newtonian relation continues as there is no limit on the electrons speed. For velocities of $3\text{x}10^8$ m/s and under (approximately 20% of *c*) classical and relativistic calculations give the same values of required kinetic energy.

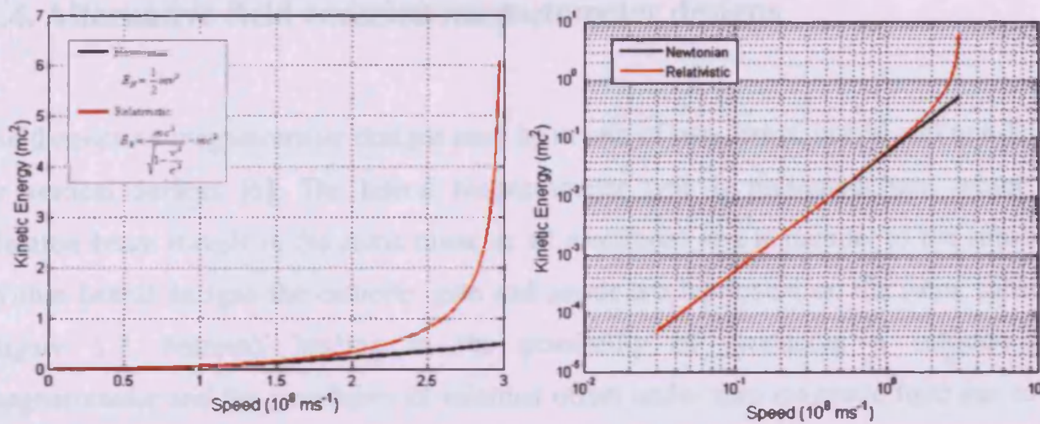

Figure 1.6. Illustrating the difference between Relativistic (red) and Newtonian (black) mechanics, with significant error appearing between the two systems when an electron travels faster than 30% of the speed of light.

The field emission magnetometer may further be modelled by considering a series of current equations that are not dissimilar to the BJT equation for current. Inspection of figure 1.4 (bottom left) implies that the cathode source of electrons within the device may be drawn towards one of three electrodes (the gate, anode or substrate) with the possibility of leakage current occurring through the silicon oxide of the device (I_L). This gives rise to the following relations for current within the device:

$$|I_k| = \left|(I_{a1} + I_{a2}) + I_g + I_s + I_L\right| \qquad \text{Eq. 1.5}$$

With all emitted electrons drawn to the anode under, $V_a > V_g$, and all emitted electrons drawn to the gate for, $V_a < V_g$. This shows the biasing condition of the device for two cases of the anode voltage. Using Gomer's [7] conventions for devices of this type, the anode current approximately equals the cathode current when the anode voltage is twice as great as the gate voltage though this clearly depends upon device geometry, otherwise the gate current is approximately the cathode current.

1.4. Alternative field emission magnetometer designs

Field emission magnetometer designs may be in one of two forms, lateral and non-lateral or vertical devices [6]. The lateral magnetometer type is presented here, where the electron-beam travels in the same plane as all electrodes and is parallel to the substrate. Within lateral designs the cathode, gate and anode are fabricated on the same substrate (figure 1.7, bottom), leading to the possibility of producing a self-contained magnetometer and the possibility of minimal offset under zero magnetic field due to the cathode and anode being automatically aligned during fabrication (one photolithographic mask is used). This approach of lateral fabrication also allows for the possibility of reductions in the variance of emitted current as these structures tend to be more controlled with regards to geometry than vertical devices [13]. Lateral designs also allow for a number of different anode-cathode spacings in a spoke-like-structure, resulting in spatial variation in sensitivity and magnetic field range as appose to the fixed sensitivity and range as typically found with vertical devices (figure 1.7, top). Other advantages of lateral over non-lateral fabrication include the ability to integrate devices into ICs with control electronics on the same substrate, as well as allowing substrate to play a substantial role in electron trajectory, by setting lines of force of electric fields between the gate, cathode, anode and substrate where necessary (demonstrated in chapter five).
Research has shown that non-lateral devices give a smaller signal to noise ratio (SNR), requires greater operating voltages, are unable to be self contained in fabrication, require more steps to fabricate and may not be integrated onto an IC easily [1]. It is for these reasons that a lateral device is chosen over the vertical.

Vertical field emission example:

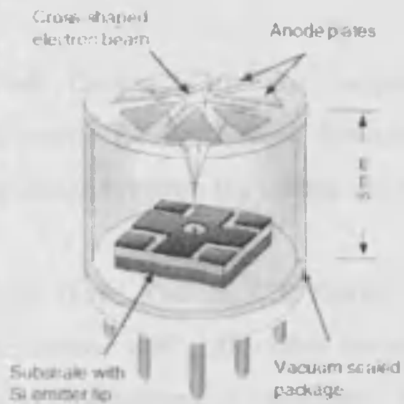

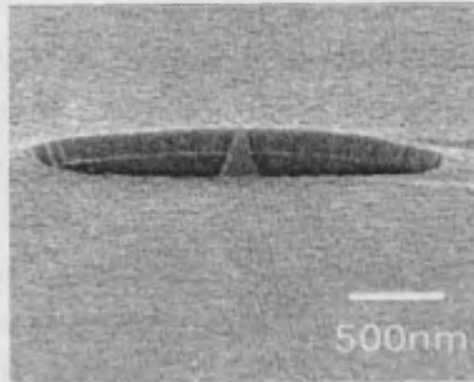

Lateral field emission example:

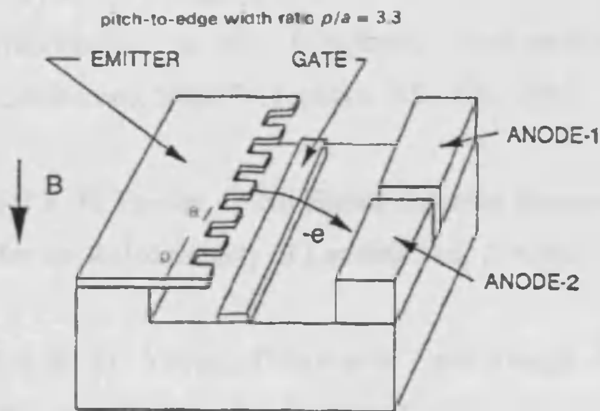

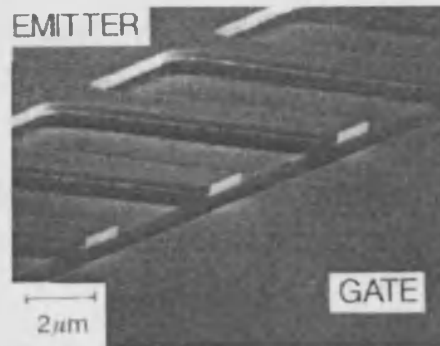

Figure 1.7. Showing an example of a vertical design (top) and lateral design (bottom) as reviewed by Busta, from [8]. Unless stated otherwise, all top layers are n-doped silicon.

1.5. References

[1] D. M. Garner, *Case for Support: Control of Electron Motion in Vacuum Microelectronic Devices: High Sensitivity Magnetic sensors and Other Applications*, correspondence between the companies involved in this CASE project, 2003

[2] G. Hui, D. M. Garner, P.J. French. *Design of a CMOS-Compatible Field-Emission Magnetic Sensor with Adjustable Sensitivity*, Technical Digest of the 16th International Vacuum Microelectronics Conference, 71-72, 2003.

[3] D. M. Garner and P. J. French, *Modelling of emitted distribution and electron trajectories in the thin-filmed field-emission triode*, Vacuum Microelectronics Conference, Issue 7-11, pages 135 - 136, 2003.

[4] R. H. Fowler, L. Nordheim, *Electron Emission in Intense Electric Fields*, Proceedings for the Royal Society of London, Vol. 119, pp. 173–181, 1928.

[5] R. D. Young, *Theoretical Total-Energy Distribution of Field-Emitted Electrons, Physical Review*, Vol. 113, No. 1, 1958.

[6] G. N. Fursey, *Field Emission in Vacuum Microelectronics 1st Ed.*, Springer, Jan 2005.

[7] R. Gomer, *Field Emission and Field Ionization,* Oxford University Press, London, 1961.

[8] H. Busta, *Review of Vacuum Microelectronics*, Amoco Research Centre, 1992.

[9] G.N. Fursey, *Field emission in vacuum micro-electronics*, Applied Surface Science 215 pp. 113–134, 2003.

[10] D. Dahl, *SIMION-3D version 7*, Idaho National Engineering and Environment Laboratory, 2000.

[11] M. J. Caruso, C. H. Smith, *A New Perspective on Magnetic Field Sensing, Magnetic sensors tutorial by Honeywell*, www.honeywell.co.uk, 2000.

[12] J. Clarke, *SQUIDs*, Scientific American 271, p. 46, 1994.

[13] I. K. Kominis, T. W. Kornack, J. C. Allred and M. V. Romalis, *A subfemtotesla multichannel atomic magnetometer*, Nature Letters to Nature Vol. 422, p. 596, 2003.

[14] D. Y. Kim, H. J. Kong, and B. Y. Kim, *Fiber-optic DC Magnetic Field Sensor with Balanced Detection Technique*, IEEE Photonics Technology Letters, Vol. 4, No. 8, August 1992.

[15] A. B. Evgeny and S. I. Vavilo, *Optically pumped atomic magnetometers after three decades*, Optical Engineering, Vol. 31, Issue 4, pp. 711-717, 1992.

[16] G. S. Waters, and P. D. Francis, *A Nuclear Precession Magnetometer, Journal Science Instrumentation*, Vol. 35 p. 88, 1958.

[17] H. D. Young and R. A. Freedman, *University Physics*, Addison-Wesley publishers, 2000.

[18] Z. B. Randjelovic, M. Kayal, R. Popovic, and H. Blanchard, *Highly Sensitive Hall Magnetic Sensor Microsystem in CMOS* Technology, IEEE Journal of Solid State Circuits, Vol. 37, No. 2, 2002

[19] B.B. Pant, *Magnetoresistive Sensors*, Scientific Honeyweller, Vol. 8, no.1, pp. 29-34, 1987.

[20] HMC1053 3-axis magnetoresistive magnetic sensor by Honeywell, www.ssec.honeywell.com/magnetic/datasheets/HMC105X.pdf

[21] K.-M.H. Lenssen, D.J. Adelerhof, H.J. Gassen, A.E.T. Kuiper, G.H.J. Somers, and J.B.A.D. van Zon, *Robust giant magnetoresistive sensors,* Sensors and Actuators A: Physical, 85(1-3):1–8, 2000.

[22] J.E. Lenz, *A review of magnetic sensors*, Proceedings of the IEEE, 78:973–989, 1990.

[23] S. Middelhoek, A. A. Bellekom, U. Dauderstadt, P. J. French, S. R Hout, W. Kindt, F. Riedijk, and M. J. Vellekoop, *Review Article on Silicon Sensors*, IOP publishing, 1995.

[24] http://www.magneticsensors.com/datasheets.html

[25] R.S. Popovic, J.A. Flanagan, and P.A. Besse, *The future of magnetic sensors,* Sensors and Actuators A – Physical, 56:39–55, 1996.

[26] M.I. Marques, P.A. Serena, D. Nicolaescu, and A. Correia, *Design of field emission based magnetic sensors*, Journal of Vacuum Science and Technology B, 18(2):1068–1072, 2000.

[27] M.I. Marques, P.A. Serena, D. Nicolaescu, and J. Itoh, *Analysis of a field-emission magnetic sensor with compensated electron-beam deviation*, Journal of Vacuum Science and Technology B, 17(2):788–791, 1999.

[28] Dan Nicolaescu and Valeriu Filip, *Modeling of a magnetic sensor based on vacuum field emission*, Applied Surface Science, 94/95:87–93, 1996.

[29] Dan Nicolaescu, Valeriu Filip, and Junji Itoh, *Field emitter magnetic sensor with steered focused electron beam*, Japanese Journal of Applied Physics Part 1, 40(4A):2173–2177, 2001.

[30] M.I. Marques, P.A. Sarena, D. Nicolaescu, and A. Correia, *Field emission magnetic sensors based on focusing devices*, Solid-State Electronics, 45:977–986, 2001.

[31] William J. Orvis, Charles F. McConaghy, Dino R. Ciarlo, Jick H. Yee, and EdW. Hee, *Modeling and fabricating micro-cavity integrated vacuum tubes*, IEEE Transactions on Electron Devices, 36(11):2651–2657, 1989.

[32] Jung-Hyeon Park, Hyung-Il Lee, Heung-Sik Tae, Jeung-Soo Huh, and Jung-Hee Lee, *Lateral field emission diodes using simox wafer*, IEEE Transactions on Electron Devices, 44(6):1018–1021, 1997.

[33] Soon-Soo Park, Dong-Il Park, Sung-Ho Hahm, Jong-Hyun Lee, Hyun-Chul Choi, and Jung-Hee Lee, *Fabrication of a lateral field emission triode with a high current density and high transconductance using the local oxidation of the polysilicon layer*, IEEE Transactions on Electron Devices, 46(6):1283–1289, 1999.

[34] J. Roth, *Industrial plasma engineering*, Vol. 1, Institute of physics publishing, 2000.

Chapter 2

Field emission

An investigation into field emission is made for semiconductors (specifically for n-doped Si). The principle of the field emission magnetometer is investigated, an in depth look into field emitters is made laying the foundations for a model of vacuum magnetic sensor devices though the hybridization of the analytical and numerical models.

2.1. Theoretical description

Field emission, a quantum mechanical process, is the only method that *pulls* electrons from a surface, i.e. this is the only method that lowers the work function of a material instead of applying energy to electrons so that they may overcome the potential barrier. The remaining methods of electron emission are by heat energy or thermionic emission [1 pp.159-162], where electrons gain enough kinetic energy from the heating of a cathode to overcome the potential barrier (utilised in thermionic valves). Electron emission by light energy or the photoelectric effect [1 pp.162-164] is also possible. Explained mathematically by Albert Einstein in 1905, electrons gain enough kinetic energy to overcome the potential barrier by absorption of electromagnetic radiation of a given frequency (utilised in solar cells). The forth method of liberating electrons from a surface material is by secondary emission [1 p.245], where electrons emitted by another one of the three methods mentioned strike an anode and may have sufficient energy to *push* other electrons from that anode. By this method, one electron would give rise to several electrons, assuming the initial electron has sufficient energy to do this (utilised in photon multipliers).

Field emission is the youngest of the methods of electron generation to be used commercially and the application of field emission to commercial devices is known as vacuum microelectronics, a relatively new field in which field emission is utilised within a typical micro-sized device under vacuum. Because of the nature of field emission, i.e. it is considered passive relative to the other types of emission, where the application of heat or light is not required, it may be utilised at the micro level where the ballistic transport of electrons from emitting cathodes are drawn towards collector electrodes. In the context of field emission vacuum magnetometers under vacuum-microelectronics, this project concerns itself with field emission from heavily n-type silicon semiconductors although thermionic emission is also considered as this constitutes unwanted emission.

2.1.1. The Fowler Nordheim equation

The process of field emission is not yet fully understood though a comprehensive model of field emission in which the tunneling of electrons through a surface potential barrier is described was developed by Fowler and Nordheim in 1928 [1 - 7]. The Fowler-Nordheim model satisfies a great deal of models carried out in the area of field emission and is used as the basis of field emission in this thesis.

The Fowler Nordheim model of field emission indicates the quantum mechanical process of electron emission, i.e. field emission or quantum tunnelling. Occurring when high electric fields are present on a conductive surface, where the emitted current density is a convolution between the electron supply within an emitter, i.e. the degree of conductivity of the emitting material, and the probability of emission, i.e. the electric field across the emitter. The electron supply is set during fabrication of the device where a high level of doping creates highly conductive emitting material, such as highly conductive n-doped (phosphorous) silicon in devices presented here, and although the conductivity, and hence electron supply, is considered constant throughout device testing irrespective of temperature [6]. The probability of emission is subject to the electric field which is itself is subject to device geometry, where electric fields of the order of 10^7 V/cm [6 p.45] are necessary for successful field emission. In order to achieve electric fields of this magnitude at relatively low gate-cathode potentials it is necessary to have the extraction gate close to the cathode tip, with additional field enhancement gained by the curvature of the cathode tip. This electric field enhancement is due to the curvature of the cathode tip because, unlike conducting spheres where any electric charge is evenly distributed, pointed tips (or areas of high curvature) concentrate the electric charge which effectively concentrates the electric field in these areas. Without pointed tips the electric fields required to generate field emission can cause the supporting dielectric (2 μm or 2×10^{-4} cm of silicon oxide for devices presented here) layer to break down as silicon oxide failure begins in the region of 10^6 V/cm [6 p. 45] where 10^7 V/cm is necessary for field emission.

Quantum tunnelling relies on the fact that electrons exhibit wave-particle like behaviour. The application of an electric field bending the potential barrier at the cathode-vacuum interface to such a degree that the probability of an electrons wave function to tunnel through the remaining potential barrier greatly increases. The effect of a high electric field at the apex of an emitter tip may be seen in figures 2.1, where the principle of field emission is shown with the relationship between the potential energy of an electron and distance from the material surface, i.e. potential barrier. The potential barrier is seen to severely deform under the presence of increasing electric fields, where under very high fields the barrier deforms to such an extant that the probability of an electron escaping to increase to the point where a large current density may be observed. Electrons that successfully escape have energies centred on the work function (Φ) in a Fermi–Dirac distribution [3] though all emitted electrons are assumed to have identical energies outside the crystal lattice.

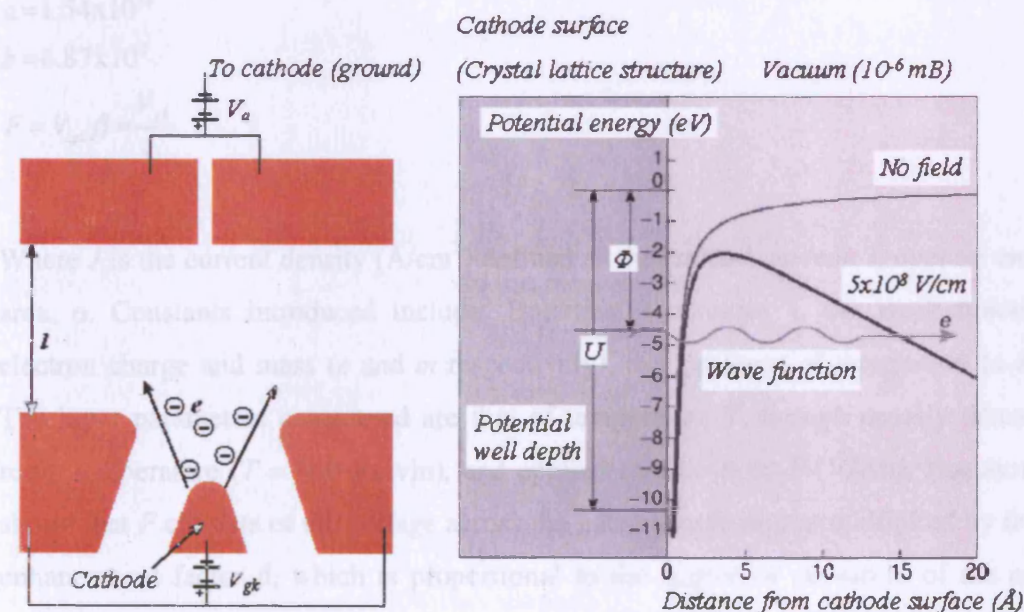

Figure 2.1. The schematic of the emitting stage of the field emission magnetometer (left), and bending of the potential barrier under an electric field (right, from [13 p. 115]).

Young [Young, 3] gives the electric current per unit area, i.e. current density, as the integration of the product of electron supply and transmission coefficient (the probability of emission), leading to the Fowler-Nordheim equation in terms of applied electric field and temperature [3 p.111]:

$$J(F,T)=\frac{aF^2}{\phi}\exp\left(\frac{-b\phi^{\frac{3}{2}}}{F}\right)\frac{\frac{3}{2}\pi kTb\phi^{\frac{3}{2}}/F}{\sin\left(\frac{3}{2}\pi kTb\phi^{\frac{3}{2}}/F\right)} \qquad \text{Eq. 2.1}$$

Valid for $0 < T < 1{,}700$ K and $F < 1\text{x}10^9$ V/cm

With:

$k=8.62\text{x}10^{-5}$

$\phi=4.52$

$a=1.54\text{x}10^{-6}$

$b=6.87\text{x}10^{7}$

$F=V_{gk}\beta\approx\frac{V_{gk}}{r_k}$

Where J is the current density (A/cm^2) defined as the emitted current, I, over an emission area, α. Constants introduced include: Boltzmanns constant k, the work function Φ, electron charge and mass (e and m respectively), and products of integration (a and b). The input parameters considered are that of temperature T, though usually taken to be room temperature (T = 300 Kelvin), and applied electric field F (V/cm). Equation (2.1) shows that F consists of the voltage across the gate-cathode region multiplied by the field enhancement factor β, which is proportional to the degree of curvature of the cathode apex and is approximately the reciprocal of the radius of the cathode area, r_k [5 p. 46]. Within this context device operation is thought to be strongly dependent on input voltage and geometry of the device.

A number of assumptions are introduced at this point that include, a constant work function of 4.52 eV for the material used (Silicon), when realistically research has indicated that the work function fluctuates around a mean of Φ with small variance defined by surface changes in morphology (crystal face orientation) and chemistry (bond formation) caused by the stochastic process of electron emission [6 and 9]. Other assumptions include the temperature range is close to room temperature, and due to this thermal emission is considered negligible, with thermal-field emission having effect at temperatures greater than 1,000 K [6 p. 45].

Figure 2.2 (top) shows the Thermal-Field current densities for a number of temperatures over typical gate-cathode range for devices of this type (up to 100 Volts) with an arbitrary field enhancement factor of 1×10^6 [10]. As seen all current densities are of the same order for low to moderate temperatures, i.e. for T around or below room temperature (300 K), otherwise for higher T (greater than 1000 K) the current density is multiplied by a temperature dependence factor; $\frac{\frac{3}{2}\pi kTb\phi^{\frac{3}{2}} / F}{\sin\left(\frac{3}{2}\pi kTb\phi^{\frac{3}{2}} / F\right)}$, which may be seen in figure 2.2 (bottom) showing the temperatures dependence of the Fowler Nordheim equation over T up to the melting point of silicon $T = 1{,}690$ K [27 p. 2581], with a fixed electric field, and as seen this factor is approximately unity for room temperatures within a small variance of 300 K, reaching a factor of thirty for higher temperatures reflecting that the Fowler-Nordheim equation is largely independent of temperature conditions for $T < 1{,}000$ K, i.e. the emitted electrons are said to be cold generated [2]. Other assumptions here include relatively large field emitters, i.e. of the order of 100 nm radius, no parasitic nano or submicron emission sites around the emitter surface, and joule heating effects are small due to low current density.

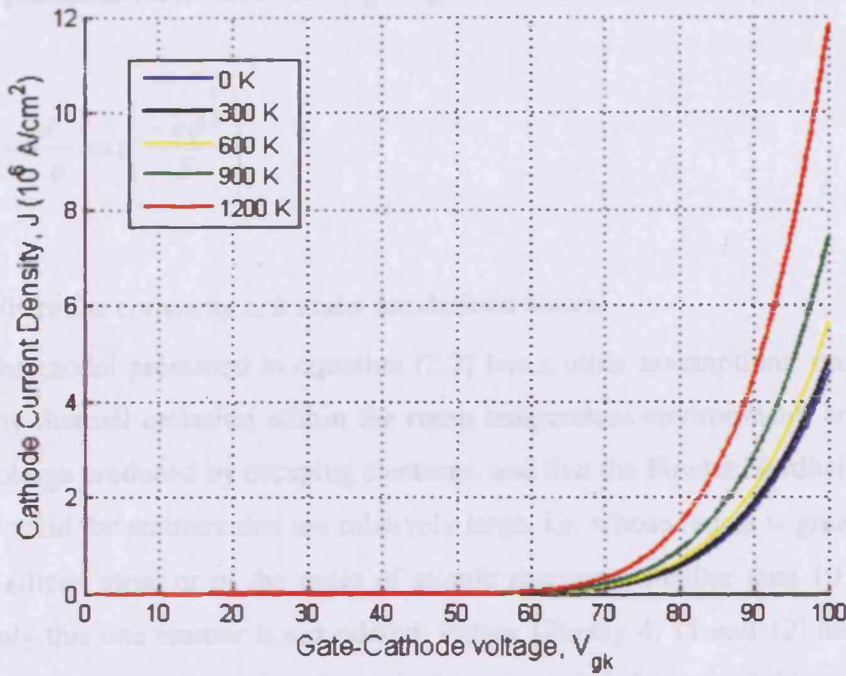

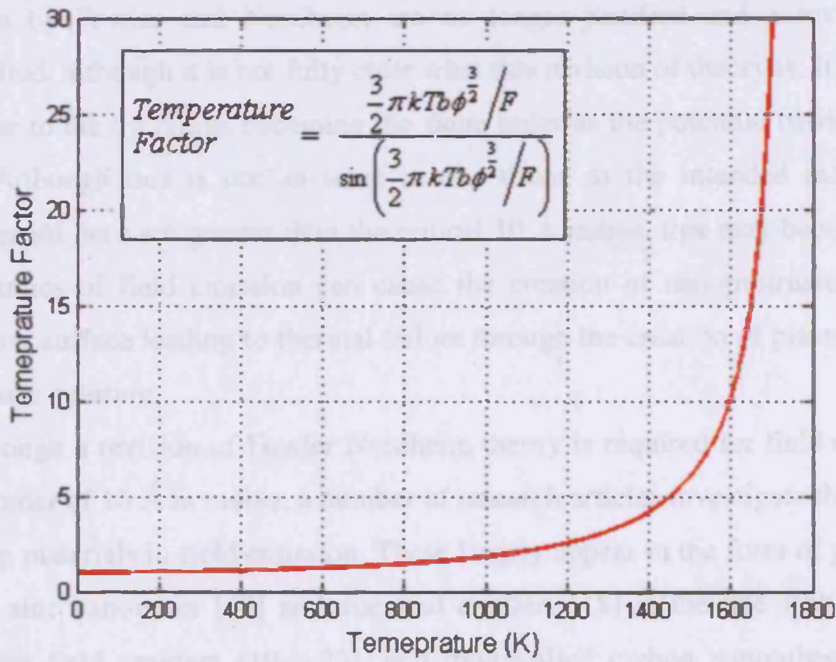

Figure 2.2. Electron current density over electric field for a number of temperatures (top), and temperature dependence factor over temperature with fixed electric field with temperature at constant field $F = 1\text{x}10^8$ V/cm (bottom).

The standard Thermal-Field equation may be further simplified with the temperature dependence factor set to unity giving the Fowler Nordheim equation used:

$$J \approx \frac{aF^2}{\phi} \exp\left(\frac{-b\phi^{\frac{3}{2}}}{F} \right) \qquad \text{Eq. 2.2}$$

Where the constants *a, b* and ϕ are defined above.

The model presented in equation (2.2) has a other assumptions, namely, the absence of any thermal emission within the room temperature environment, any changes in barrier voltage produced by escaping electrons, and that the Fowler Nordheim model of emission is valid for emitters that are relatively large, i.e. whose radius is greater than the radius of a silicon atom or of the order of atomic sharpness smaller than 10 Å or 1 nm, and that only this one emitter is considered. Fursey [Fursey 4, 11 and 12] has reviewed a number of articles that show that for cathode emitter tips that are of this order, the assumptions made by Fowler and Nordheim are no longer justified and a revision of theory is required, although it is not fully clear what this revision of theory is. It is thought that this is due to the tip radius becoming the same order as the potential barriers width [4 pp. 1-8]. Although this is not an issue in this thesis as the intended radii of cathode tips presented here are greater than the critical 10 Å radius, this may become an issue as the dynamics of field emission can cause the creation of nanoprotrusions on the cathode emitter surface leading to thermal failure through the creation of plasma around the gate-cathode aperture.

Although a revision of Fowler Nordheim theory is required for field emitters that are of the order of 10 Å in radius, a number of research articles investigate the use of atomically sharp materials in field emission. These largely appear in the form of porous silicon [14 - 16], zinc nanowires [17] and diamond emitters [18] in the late 1990's, then individual carbon field emitters [19 - 23], and multiwalled carbon nanotubes and carbon films relatively recently [24 – 25, published in 2002].

2.1.2. Determination of tip radius

The radius of the cathode tip, r_k, may be found from the Fowler-Nordheim equation [5] by first substituting the electric-field and current-density, i.e. $F = \beta V$ and $J = \frac{I}{\alpha}$ respectively, and then rearranging and solving:

$$\frac{I}{\alpha} = \frac{a(\beta V)^2}{\phi} \exp\left(\frac{-b\phi^{\frac{3}{2}}}{\beta V}\right)$$

Eq. 2.3

$$\ln\frac{I}{V^2} = \ln\left(\frac{a\alpha\beta^2}{\phi}\right) - \frac{b\phi^{\frac{3}{2}}}{\beta V}$$

The linearising of equation (2.3), i.e. plotting $\ln\frac{I}{V^2}$ against $\frac{1}{V}$, shows the above to be fairly linear, the result of which may be equated with a straight line with slope and intercept of $m = \frac{-b\phi^{\frac{3}{2}}}{\beta}$ and $c = \ln\left(\frac{a\alpha\beta^2}{\phi}\right)$ respectively, allowing for the field enhancement factor and effective emitting area to be found:

$$\beta = \frac{-b\phi^{\frac{3}{2}}}{m}$$

Eq. 2.4

$$\alpha = \frac{\phi \exp(c)}{a\beta^2}$$

Where the field enhancement factor, β is dimensionless and the resulting emitting area, α is in units cm^2. The radius (r_k) may then be found from the emitting area with validation for the tip area being made against electron micrographs of the cathode tip, where as stated above the emission radius is approximately equal to the radius of curvature of the cathode tip.

Although this approach is considered the most simplified method of data extraction and it is the most widely used, it is thought to give an answer to within 20% of the actual figure [5 p.47]. The error is due to the incorrect assumption that the electric field is constant on the emitter surface because the emission area and field enhancement factors are constant when in these factors are stochastic resulting in a constantly changing electric field across the emitter surface. Though the variance in factors is minimal if the vacuum level is high and the operating voltage is relatively low, i.e. possibilities of nanoprotrusions that cause thermal-field emission sites that lead to device breakdown are minimal. This is discussed further in the next subchapter, *Stochastic processes: Ion bombardment and cathode tip changes.*

An example is shown in figure 2.3 with the schematic of the Field Emission magnetometer circuit (left), a model of the field emitter tip (spherical cap on a conical shank is assumed by Fowler and Nordheim [2], right), a voltage sweep of the extraction gate with corresponding cathode current may be seen in figure 2.4 (top), with corresponding Fowler-Nordheim plot for this data (figure 2.4, bottom). In order to gain a high confidence interval (95% bands on the mean [26 p.69]), thirty samples are collected across a number of devices with very similar gate-cathode geometry, i.e. cathode aperture and height (relative to the gate) of, $a \approx 0.5\mu m$ and $h \approx 0\mu m$, allowing for quantitative statistical estimation of gate and cathode areas. A preliminary result of figure 2.4 suggests that the experiment is repeatable, i.e. although field emission is essentially based on probability, field emission has occurred during all thirty experiments, albeit at slightly different current densities though these differences appear to be small.

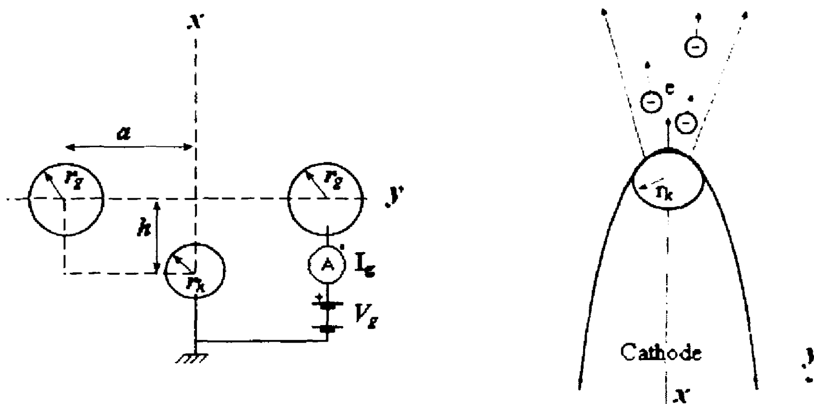

Figure 2.3.The schematic of the Field Emission magnetometer circuit (left) and a model of the field emitter tip used (right, spherical cap on a conical shank is assumed by Fowler and Nordheim).

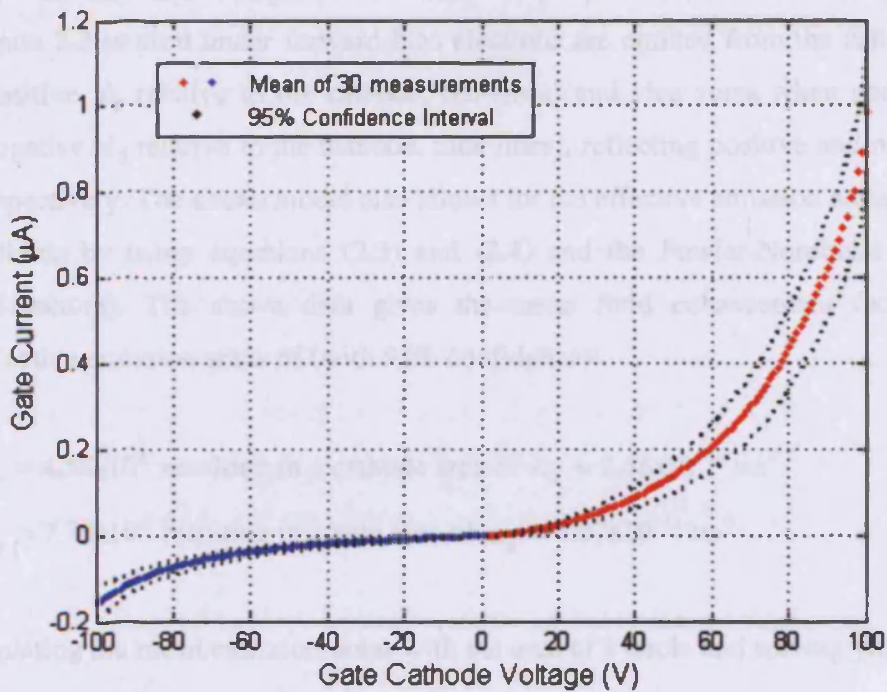

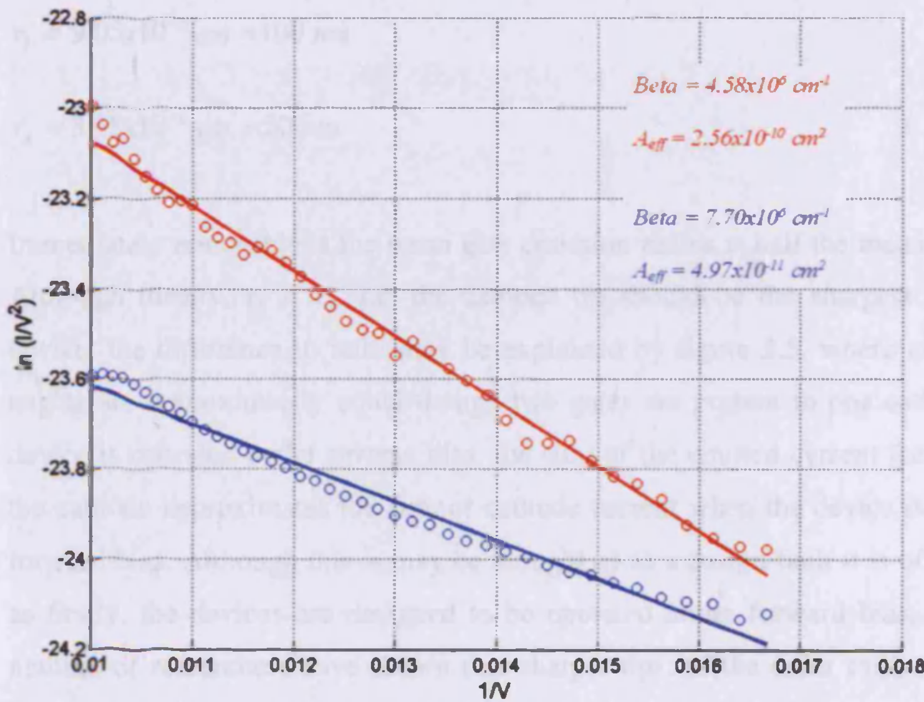

Figure 2.4. A voltage sweep for the extraction gate-cathode voltage (top) showing confidence interval bands of 95% centred on the mean of 30 samples for a number of devices. The corresponding Fowler Nordheim plot (bottom) carried out on the mean data allows for statistical estimation of cathode and gate areas (read and blue respectively).

As seen from above (top) and as described by equation (1.6), when the configuration of figure 2.3 is used under forward bias electrons are emitted from the cathode to the gate (positive V_g relative to the cathode, red lines) and vice versa when under reverse bias (negative V_g relative to the cathode, blue lines), reflecting positive and negative currents respectively. The above model also allows for the effective emission areas of the gate and cathode by using equations (2.3) and (2.4) and the Fowler-Nordheim plots in figure 2.4(bottom). The above data gives the mean field enhancement factors and mean effective emission areas of (with 95% confidence):

$\beta_k = 4.58x10^6$ resulting in a cathode area of $\alpha_k = 2.56x10^{-10}\ cm^2$

$\beta_g = 7.70x10^6$ resulting in a gate area of $\alpha_g = 4.97x10^{-11}\ cm^2$

Equating the mean emission-areas with the area of a circle and solving yields tip radii of:

$r_k = 9.05x10^{-6}\ cm \approx 100\ nm$

$r_g = 3.98x10^{-6}\ cm \approx 50\ nm$

Immediately noticeable is the mean gate emission radius is half the mean cathode radius. Although ideally, $r_k < r_g$, i.e. the cathode tip should be the sharpest area within the device, the difference in radii may be explained by figure 2.5, where cathode and gate angles are approximately equal though two gates are present to one cathode. When the device is operated under reverse bias, the sum of the emitted current from both gates to the cathode approximates the sum of cathode current when the device is operated under forward bias. Although this is may be thought of as a design fault it is of no significance as firstly, the devices are designed to be operated under forward bias, and secondly a number of researchers have shown that sharper tips, of the order to tens of nanometres lead to instability while tip radii of the order of hundreds of nanometres are far more stable [27 - 30].

Verification of the cathode tip size may be achieved by calculating the radius of curvature of the emitting cathode structure, r_c, which is analogous to the calculated radius of the emission area, and may be compared against the empirical radius of the emission area derived above, i.e. $r_c \approx r_k$.

In order to derive the radius of curvature, it is necessary to define the cathode surface parametrically around the cathode apex, calculate the degree of curvature (γ, which gives the "sharpness" of the cathode tip), and then find the corresponding radius of curvature which is the reciprocal of γ, the algorithm and proof of which is well documented [31 pp. 740 - 745]. This is achieved in figure 2.5 where the apex of the cathode tip may be approximated by an ellipse with a minor and major axis of $x_c = 0.5\ \mu m$ and $y_c = 0.7\ \mu m$ respectively, which then may be used to solve equation (2.5):

$$\gamma(t) = \frac{\left\| r'(t) \times r''(t) \right\|}{\left\| r'(t) \right\|^3} \qquad \text{Eq. 2.5}$$

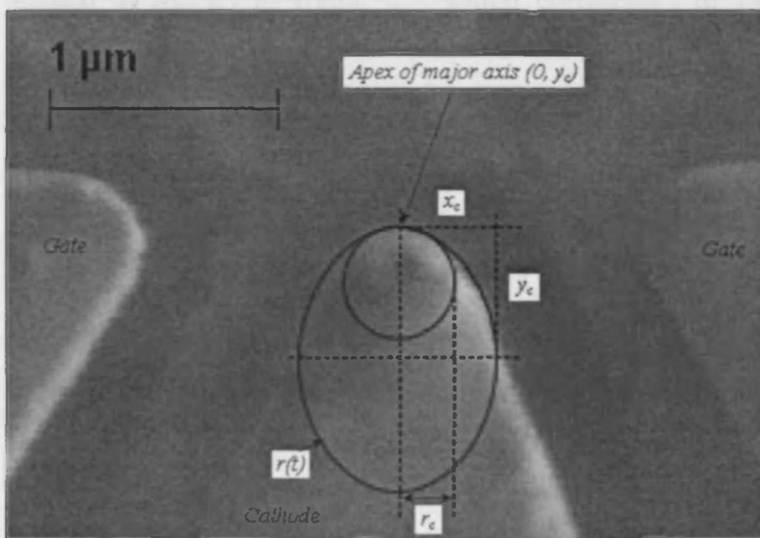

Figure 2.5. Model used to calculate the radius of curvature r_c, shown for a typical cathode structure.

Where (all numerical values are in microns):

$$r(t) = (0.5\cos(t))i + (0.7\sin(t))j \qquad (0 \langle t \langle 2\pi)$$
$$r'(t) = (-0.5\sin(t))i + (0.7\cos(t))j$$
$$r''(t) = (-0.5\cos(t))i + (-0.7\sin(t))j$$

Leading to:

$$r'(t) \times r''(t) = \begin{vmatrix} i & j & k \\ -0.5\sin(t) & 0.7\cos(t) & 0 \\ -0.5\cos(t) & -0.7\sin(t) & 0 \end{vmatrix} = |0.35\sin^2(t) + 0.35\cos^2(t)|k$$
$$\|r'(t) \times r''(t)\| = 0.35$$

And:

$$\|r'(t)\|^3 = \left(0.25\sin^2(t) + 0.49\cos^2(t)\right)^{\frac{3}{2}}$$

Substituting in the coordinate for the area of interest, i.e. the endpoint of the major axis located at (0, y_c) in figure 2.5 which correspond to $t = \frac{\pi}{2}$, gives the curvature and corresponding radius as:

$$\gamma\left(\frac{\pi}{2}\right) = \frac{0.35}{\left\|r'\left(\frac{\pi}{2}\right)\right\|^3}$$
$$\gamma \approx 3x10^6$$

$$r_c = \gamma^{-1}$$
$$r_c \approx 300\ nm$$

As seen, although the calculated radius of curvature is over three times as large as the empirical radius of emission area, it is of the same order, i.e. r_c = 300 nm and r_k = 100 nm, and as such allows electron micrographs to give reasonably accurate quantitative estimates of the emission area.

Discrepancies between these two sets of data arise because of a number of factors, the most predominant being the model used to approximate the cathode apex such as ellipses or parabolas appearing to be the most suitable around the cathode apex. Other reasons for discrepancies are a product of tip fabrication which includes non-uniform emission sites (unwanted micro or nano-protrusions) around the apex of the cathode tip, as well as work function changes, i.e. modifying adsorbents that cover the tips non-uniformly changing the work function. Because the nature of field emission is dynamic (as can the fabrication process of tip manufacture at the sub-micron level), these results may result in unintended emitter radii, with larger radii (greater than hundreds of nm) requiring higher electric fields to generate field emitted electrons, and smaller radii (smaller than tens of nm) resulting in potential run-away effects of thermal-field emission eventually leading to device breakdown, i.e. work function changes and the dynamics of stochastic adsorption-desorption feedback processes ending in tip destruction by melting [27] as occurred below:

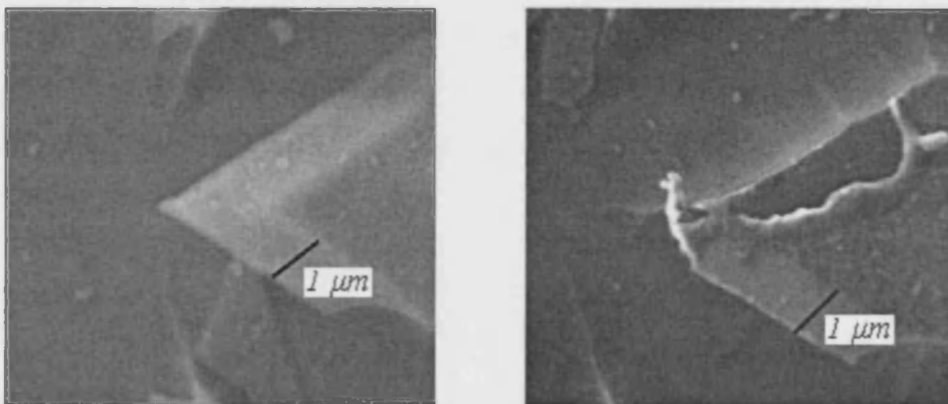

Figure 2.6. Electron micrographs of a cathode before (left) and after (right) tip destruction.

Assuming the emitting tip radius stays within this safety band, between tens and hundreds of nm, a safe level of current density is observed, and stochastic processes of tip change within this band are acceptable due to the device operating on fractional changes in detected anode current over an applied magnetic field. Because the anode current is dependent upon the position and orientation of the cathode tip, any changes in cathode tip direction over the lifetime of the device may result in difficulties in device operation.
Overall, the above results indicate these tip radii appear to be well above the critical 10 Å value for the Fowler Nordheim model to function [27] and may be supported by the electron micrographs in figure 2.5, where the cathode and gate emitting tips appear to confirm that emission areas are of this order. The cathode structure and stability is central to this project, where it is the source of electron emission and its location must be accurately aligned with the anode split in order to achieve accurate measurements for magnetic field detection. The structure and stability of the cathode is given in more detail in the next chapter.

2.2. Factors governing device operation

A number of factors affect emission characteristics of the apex of the cathode, primarily intrinsic properties considered here and extrinsic properties, considered in chapter 3, *Experimental setup and Magnetometer Evolution*, which are factors in device fabrication, preparation and usage that effect device stability.

2.2.1. Vacuum requirements

Vacuum requirements in field emission play a dominant role as illustrated in figure 2.7. Here the gate current is measured as a function of increasing pressure. As seen, there is an inverse relationship between gate current and pressure as expected, with a gradual decrease in gate current over increasing pressure. It is believed that this is due to a combination of the electron-gas-molecule collisions between electrons from the cathode to the gate, and the impingement rate of gas molecules on the emitter surface by adsorption [33]. Note also the gate current changes far less between the pressures of 10^{-6} and 10^{-5} mBar, indicating that electron-gas-molecule collisions and adsorption factors are an issue above 10^{-5} mBar, and that this may be the Molecular-Laminar flow transition point though this is unclear.

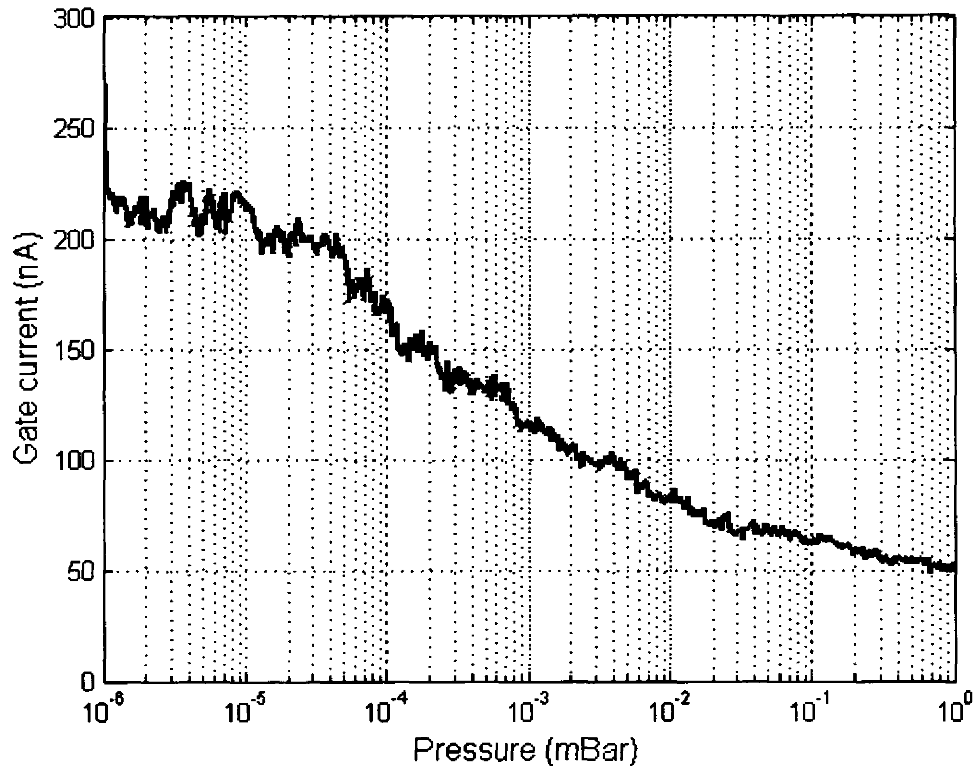

Figure 2.7. Showing the relationship between gate current and increasing pressure for the vacuum magnetic sensor.

Although the above graph is preliminary and more research is required, it does show that the inverse relationship between gate current and pressure may be used as a pressure sensor. Field emission based pressure sensors have been proposed by Busta [Busta, 35] and the author [French, 36]. Where the use of an anode-diaphragm is suggested, in which the pressure level modulates the anode with respect to the cathode which is fixed.

The small change in gate current between 10^{-6} and 10^{-5} mBar indicates that such a pressure gauge developed by the technology offered here would be used in a low vacuum environment and are comparable to Pirani gauges [35 p.5].

2.2.2. Stochastic processes:
Ion bombardment and cathode tip changes

Because of the complexity of plasma physics only an overview is given here, where the equations of plasma physics have been intentionally omitted. In addition to this simplified view of ion bombardment, it should be noted that this is technically a vacuum requirement issue (discussed above) due to the reliance of any ions created within the vacuum chamber being dependent upon the vacuum level as dictated by Maxwell-Boltzmann theory of gases [1 pp.34-53], although it is felt that this subject deserves greater coverage as it is the prelude to a model of cathode apex erosion and apex destruction for chapter 6.1, *Future work.*

The kinetic theory of gases [1 p.34] allows for the number of remaining molecules (per cubic volume) to be calculated in a vacuum of level P (mBar), where upon these molecules, after being struck by electrons from the cathode emitter, may be ionised effectively creating a plasma and will drawn towards the cathode. Because semiconductor surfaces are essentially rough at the atomic level (referring to surface states of incomplete bonds on the cathode tip surface [37 and 38]), impact of these ions on the cathode surface may cause adsorption, where ions bombard the cathode surface and may chemically bond at the surface changing the electrical characteristics of the field emitter apex. Alternatively these impacting ions may cause desorption, where ions with sufficient energy may knock out electrons by secondary emission, and knock out emitter material into the vacuum, i.e. sputtering [40].

The nature of the plasma created by the remaining molecules at vacuum level P and emitted electrons from the cathode depends on the type of materials, gases and the individual molecules ionization energy within the vacuum chamber. Where nitrogen is considered most prominent in this research as it constitutes 78% of the Earths atmosphere [1] and has a large volume of research associated with nitrogen based plasma.

In the context of physical cathode tip changes, researchers such as Brodie [Brodie, 38] and Miyamoto [Miyamoto, 39] and suggest that due to the anode-cathode distance relative to the gate-cathode distance (of the order of 100 μm and 1 μm respectively), Ions from the gate surface are predominately responsible for cathode-tip erosion and

destruction due to the increased energy of gate-ions in comparison to anode-ions. It is assumed electrons from the cathode are accelerated and drawn towards by the gate and have sufficient momentum to knock out outer electrons of a molecule by collision, this is dependant upon the molecules ionization energy which is typically 15.6 eV for nitrogen molecules [1]. Figure 2.8 shows a schematic overview of the relationship between parameters such as cathode tip geometry, vacuum level of the system, cathode-tip temperature and surrounding temperature of the system, to the effects of field-emission, ion-bombardment, tip-heating and plasma-effects. Although an in depth account of field emission with respect to fundamental parameters (gate-cathode voltage, work function and vacuum level) serves this model already in the above chapters, figure 2.8 gives an overview of the above situation and will be used as the basis for a further cathode tip apex modelling.

Within figure 2.8 the modules of the cathode-tip and surrounding area temperature fields require solutions to the partial differential equation, the Laplace equation, for heat conduction, the ion creation and ion bombardment modules require calculus methods applied to the Maxwell-Boltzmann theory of gases, including calculation of the number of ions striking the cathode surface, an estimation given by an integral over a given area around the cathode which is the product of emission current and the residual gas ionisation cross section, and the number of atoms sputtered from the cathode surface (estimated using similar methods). All of which may be based on data from a spectrum analysis of the cathode surface before and after cathode tip failure, and all of which must be fed back into the boundary conditions (conditions that represent the physical geometry of the device) into the system. It is within this context that the field emitter magnetometer utilises non-linear, dynamic systems that are subject to the rules of Chaos theory, i.e. highly dependant upon initial conditions and environmental conditions close to the cathode tip while the device is in use.

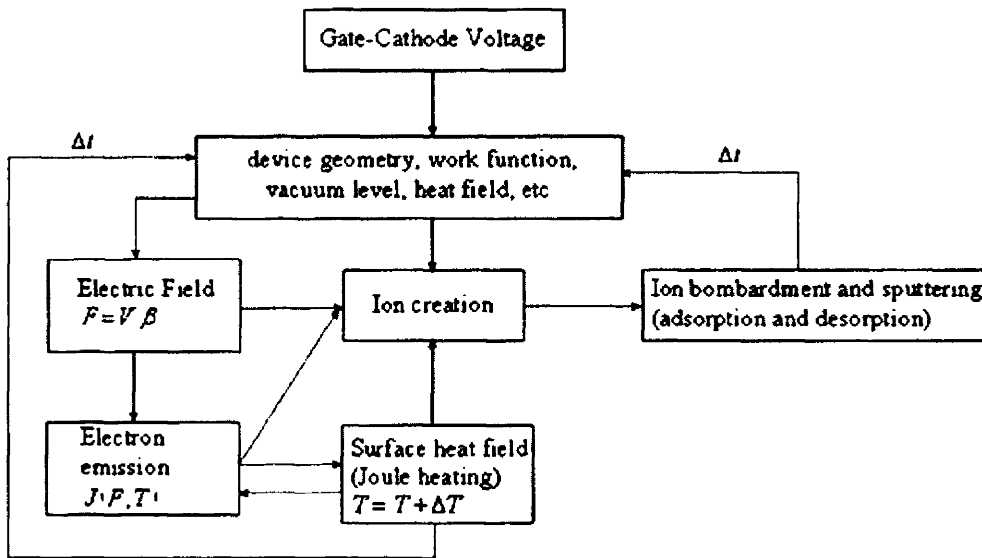

Figure 2.8. Showing the schematic overview of parameters within the system. All parameter changes are fed back into the system after Δt, which is thought to be of the order of nanoseconds due to the short electron transit time of field emitted electrons relative to solid state devices.

The schematic model presented above does not show plasma–surface interaction in the cathode area which leads to vacuum sparks, or the process of thermal failure, both of which effectively destroy the tip by causing areas of very low impedance between electrodes through plasma, which allows for electrical shorts in the system. Here, on the assumption of parasitic-protrusions on the cathode tip, large electric fields across such surfaces massively increases the emitted current density, causing joule heating of these tip protrusions, which further increasing the current density through thermal-field emission and sputtering. This injection of material, consisting of cathode tip material and predominantly nitrogen close to the tip surface, expands into the vacuum where it is ionised by bombardment from energised electrons from the thermal-field emitter. The ions within this plasma are attracted towards the most negative area of the device (the cathode tip) which place pressure on the molten cathode tip apex, resulting in craters with possible sharp edges (unwanted protrusions). These crater edges act as further sites for thermal-field emission, adding to this positive feedback cycle until the melting point of silicon is reached and the cathode tip becomes effectively blunt or electrically shorts-out the cathode-substrate or cathode-gate connections.

In addition to tip changes by the above effects, Busta [6] has suggested that the work function on the surface of the device will be affected by adsorbents in a non-uniform manner, further changing the field emission characteristics of the device. This supports the idea that field emission is a stochastic process. Starting with known parameters and device operation, but sliding into thermal-failure by a positive feedback effect of thermal-field emission, and plasma caused by small changes to tip submicrogeometry structure, i.e. blunting and the chemical composition of the electrodes.

Cathode tip changes may be seen practically in figure 2.9(top), where the cathode current is monitored for a device over twelve hours. As seen, the cathode current is seen as stable over the time measured, with a mean value of 1 μA and a standard deviation of 30 nA, indicating that derivation from the mean over the twelve hour period is small. Although the measured current is stable, a first order fit (shown in red in figure 2.9) indicates that the cathode current continually decreases and will reach device failure, i.e. when the estimated cathode current crosses the x-axis, in approximately 147 hours or 6 days. This is further illustrated in figure 2.9(bottom), where projected cathode current is seen over a 24 hour period. As seen, the rate of loss is constant at 8.7 nA/hr meaning after 24 hours 200 nA is lost from the initial value. Although this apparent rate of loss may be thought of as high relative to the mean of the cathode current (approximately 1 μA), it is stressed that this is a first order estimate and factors such as vacuum level, temperature, cathode tip structure, and stochastic processes play a large role in cathode stability.

The random spikes seen throughout the measurement, may be caused primarily by noises in measurement collection though may be thought of as instability within the system, i.e. stochastic processes of cathode tip change are occurring, making cathode current fluctuations due to Ion bombardment of the cathode tip, the function of which is highly dependant upon pressure dependence as indicated in figure 2.7. This idea is strongly supported by Miyamoto [28 p.439] and Lysenko [Lysenko, 40] who have demonstrated current stability on pressure dependence and have shown that low pressures of the order of 10^{-6} mbar lead to stable cathode currents with minimal current fluctuations.

Although the emitted current has been shown to be strongly linked to pressure by Lysenko's group and has shown to be evident in figure 2.7, the instabilities recorded in figure 2.9 for devices presented here at a constant pressure of 10^{-6} mbar are unimportant as the device as a whole functions on fractional changes, i.e. the percentage difference of total current is proportional to the applied magnetic field. However, this assumes that an even current is recoded at both anodes regardless of total current, and that this total current is not skewed to either anode by multiple emission sites on the cathode surface that are not inline with the anode gap.

Although unwanted multiple emission sites are a concern at low vacuum levels, research conducted here shows that the current deviation from the mean over relatively short periods is very small, and that the mean may be considered constant for ease of calculation throughout this text.

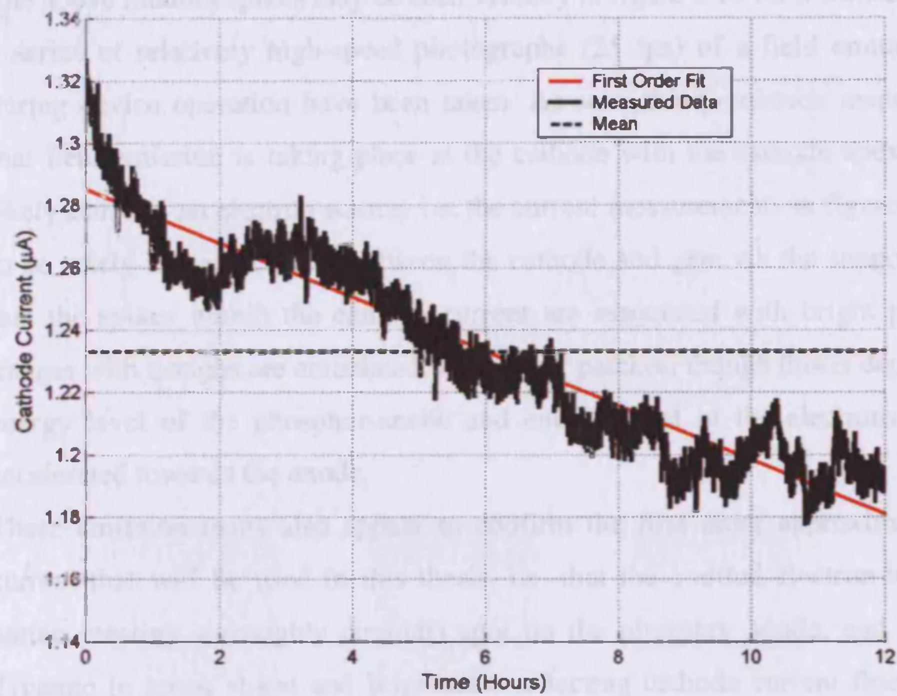

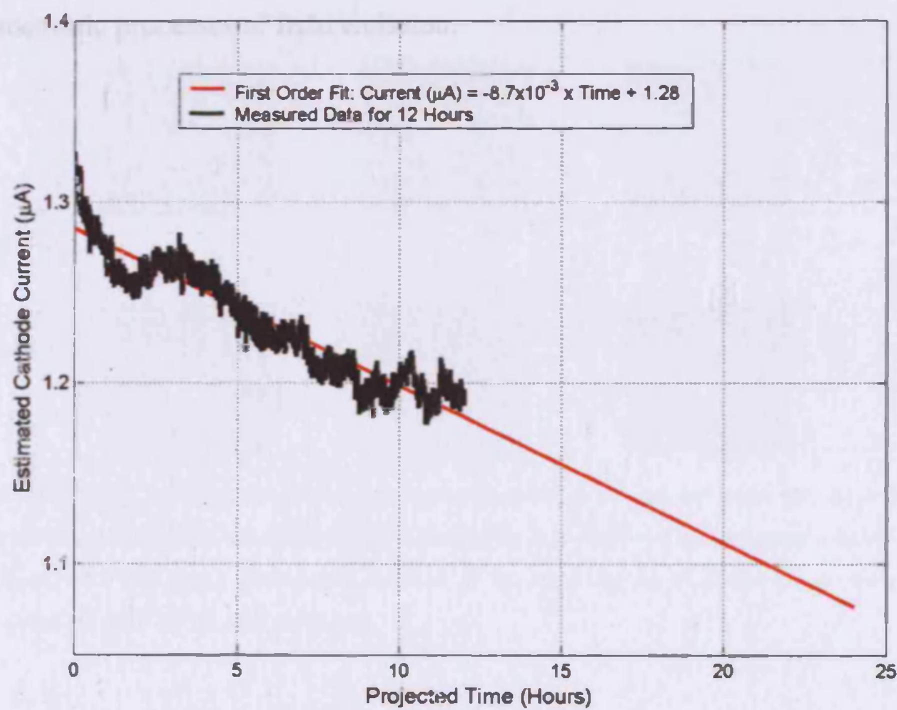

Figure 2.9. Cathode current measured over 12 hours (top) indicating the stochastic process of field emission with a mean current of approximately 1 μA and a standard deviation of 30 nA, with a first order line of best fit. Also shown is the projected estimated emitted current for a further 12 hours (bottom).

The above random spikes may be seen visually in figure 2.10 for a similar cathode, where a series of relatively high-speed photographs (25 fps) of a field emitter cathode apex during device operation have been taken. As seen these emission maps firstly indicate that field emission is taking place at the cathode with the cathode apex being the most likely cause of an electron source, i.e. the current measurements in figure 2.9 are unlikely to be solely leakage current between the cathode and gate via the supporting oxide, and that the spikes within the cathode current are associated with bright patches on these images with troughs are associated with darker patches, though this is dependant upon the energy level of the phosphor-anode and energy level of the electrons that have been accelerated towards the anode.

These emission maps also appear to confirm the first order approximation of emitted current that will be used in this thesis, i.e. that the emitted electron-beam is conic in nature creating a (roughly circular) spot on the phosphor anode, and that this spot is dynamic in terms shape and brightness, reflecting cathode current fluctuations and the stochastic processes of field emission.

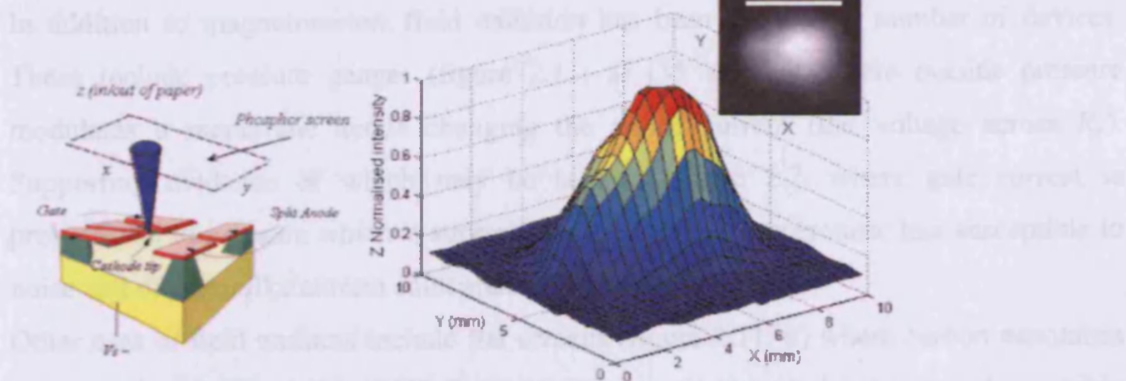

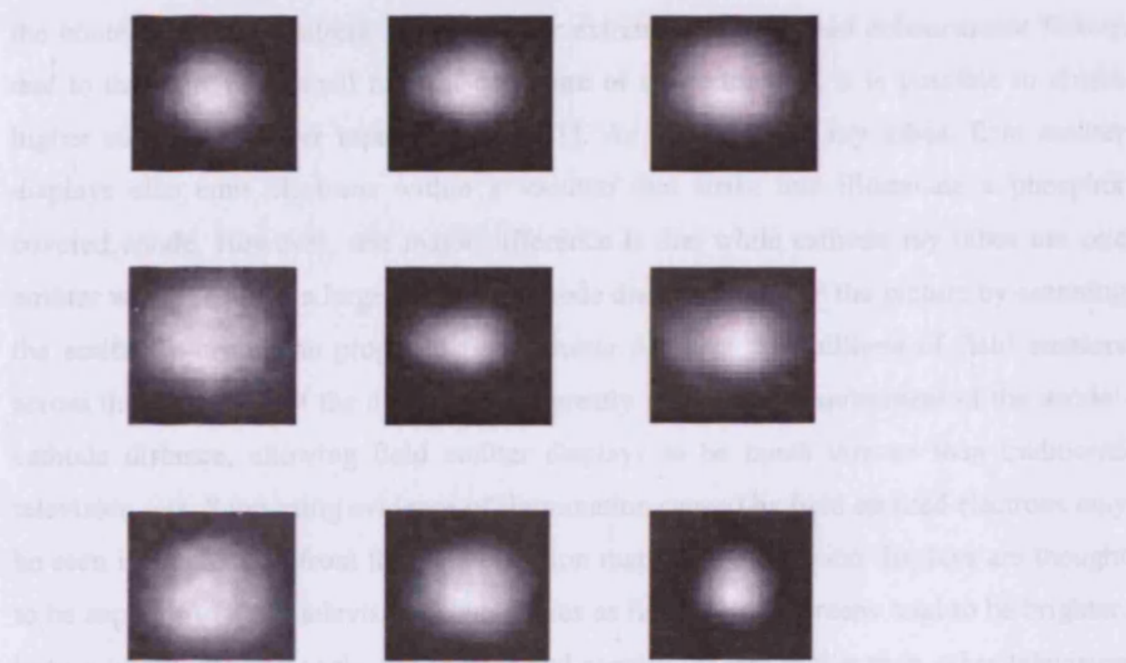

Figure 2.10. Showing the schematic representation of the set up used for recording photographic emmittance (top left), and a normalised intensity plot (top right) indicating typical e-beam composition. A series of high-speed photographs taken at 25 fps recording the emitted electron beam on the phosphor screen are seen on the bottom images.

2.3. Applications of field emission

In addition to magnetometers field emission has been used for a number of devices. These include pressure gauges (figure 2.11, a) [35 and 36] where outside pressure modulates a membrane anode changing the anode current (the voltage across R_c). Supporting evidence of which may be seen in figure 2.7, where gate current is proportional to pressure which is strongly independent of temperature, less susceptible to noise and offset unlike current solid state pressure sensors [35].

Other uses of field emitters include flat screens (figure 2.11, b) where carbon nanotubes are used as cathode tips [41 - 43]. Because of the properties of carbon nanotubes used in the context of field emitters, i.e. they offer extremely higher field enhancement factors due to the extremely small radii of curvature of their structure, it is possible to obtain higher currents at lower input voltages [41]. As with cathode ray tubes, field emitter displays also emit electrons within a vacuum that strike and illuminate a phosphor covered anode. However, one major difference is that while cathode ray tubes use one emitter which requires a large anode to cathode distance to create the picture by scanning the emitted e-beam, the proposed field emitter displays use millions of field emitters across the back pane of the display which greatly reduces the requirement of the anode–cathode distance, allowing field emitter displays to be much thinner than traditional television sets. Supporting evidence of illumination caused by field emitted electrons may be seen in figure 2.10 from the field emission maps. Field emission displays are thought to be superior to other television technologies as field emitter screens tend to be brighter, have a wider viewing angle, are thinner and require far less power than other television technologies [6].

More exotic uses of field emitters are within Field Emission Electric Propulsion (FEEP) engines used in spacecraft propulsion (figure 2.11, c). FEEP engines have been used by ESA and NASA as a method of propulsion which is suitable for missions requiring thrusts in the sub-milliNewton level [44]. These engines work by applying a strong electric field of the order of $1x10^{12}$ V/cm to pull liquid propellant, typically caesium, selected for its low ionization potential and relatively low melting point, off a tungsten needle by the potential difference applied between V_a and V_e in figure 2.11, c. After the liquid propellant has been extracted the (liquid) metal approaches a condition of local instability and due to the combined effects of electrostatic forces and surface tension, the emitted liquid metal spontaneously ionizes and a thrust-producing ion jet is extracted by the electric field. The emitting plasma (C_{s+}) requires neutriliasation to stop the plasma returning to the rocket, and the net effect is results in low thrust. Relative to other traditional fuel rockets, FEEP engines posses low accelerations by current spacecraft propulsion method by they are considered far more efficient, contain no moving parts, pressurized gases are not required and the propellant reservoir is self contained.

(a) Gauges for pressure measurement

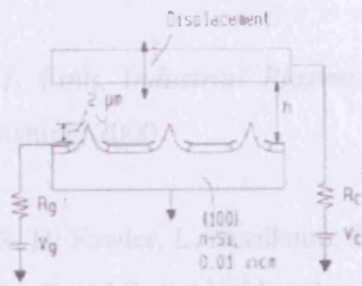

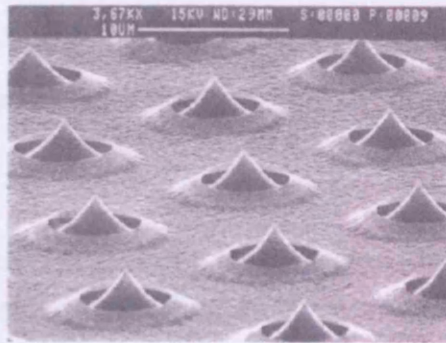

(b) Carbon nanotubes utilised in flat screen televisions

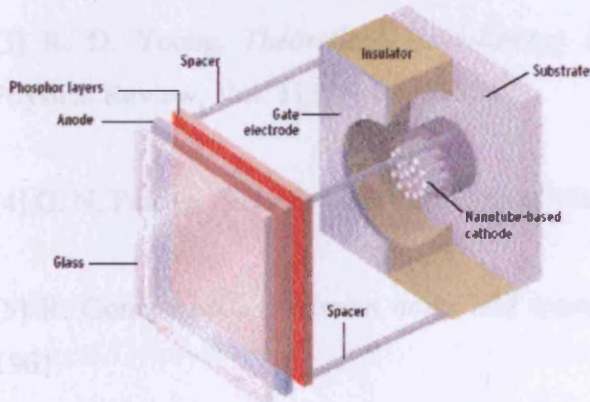

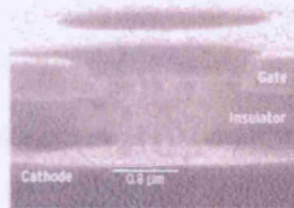

(c) Field Emission Electric Propulsion engines used in spacecraft propulsion

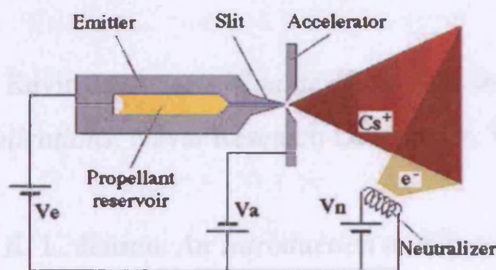

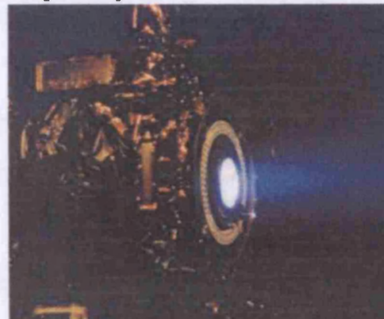

Figure 2.11. Showing numerous uses for field emission including, (a) Pressure gauges [40], (b) Ultra thin television sets [43], and (c) Field Emission Electric Propulsion engines [44].

2.4. References

[1] J. Roth, *Industrial Plasma Engineering*, Volumes 1 and 2, Institute of physics publishing, 2000.

[2] R. H. Fowler, L. Nordheim, *Electron Emission in Intense Electric Fields*, Proceedings for the Royal Society of London, Vol. 119, pp. 173–181, 1928.

[3] R. D. Young, *Theoretical Total-Energy Distribution of Field-Emitted Electrons*, Physical Review, Vol. 113, No. 1, 1958.

[4] G. N. Fursey, *Field Emission in Vacuum Microelectronics 1st Ed.*, Springer, Jan 2005.

[5] R. Gomer, *Field Emission and Field Ionization*, Oxford University Press, London, 1961.

[6] H. Busta, *Review of Vacuum microelectronics*, Amoco Research Centre, 1992.

[7] Kevin L. Jensen, *Course Notes: An Introduction to Electron Emission Physics And Applications*, Naval Research Laboratory, Washington, 2005.

[8] K. L. Jensen, *An Introduction to Electron Emission Physics and Applications, lecture notes: Beam Physics Course*, Inst. Res. El. & Appl. Phys, University of Maryland, April 2005

[9] Compiled by G. W. C. Kaye and T. H. Laby, *Tables of Physical and Chemical Constants and Some Mathematical Functions (Kaye & Laby) 16th Ed.*, Longman Sc & Tech, 1995.

[10] A.G.J. Van Oostrum, *Validity of the Fowler–Nordheim model for field electron emission, Philips Res. Rep. Supply.* 11 pp. 1–102, 1966.

[11] G.N. Fursey, D.V. Glazanov, *Deviation from the Fowler–Nordheim theory and peculiarities of field electron emission from small-scale objects (review)*, J. Vac. Sci. Technol. B 16 (2) pp. 910–915, 1998.

[12] G. N. Fursey, L. M. Baskin, D. V. Glazanov, A. O. Yevgen'ev, A. V. Kotcheryzhenkov, and S. A. Polezhaev, *Specific features of field emission from submicron cathode surface areas at high current densities*, J. Vac. Sci. Technol. B 16.1, 1998.

[13] G.N. Fursey, *Field emission in vacuum micro-electronics*, Applied Surface Science 215, pp. 113–134, 2003.

[14] Seong-Chan Bae, and Sie-Young Choi, *Improvement of the field emission characteristics of an oxidized porous polysilicon using annealed Pt/Ti surface emitter electrode,* Microelectronics Journal 37 pp. 167–173, 2006.

[15] S.E. Pullen, M. Huang, S.E. Huq, E.C. Boswell, P.D. Prewett, G.D.W. Smith And P.R. Wilshaw, Enhanced Field Emission from Polysilicon Emitters using Porous Silicon, 9th International Vacuum Microelectronics Conference, St. Petersburg 1996.

[16] W Lang, P Steiner and H Sandmaier, *Applications of porous silicon microstructuring*, J. Micromech. Microeng. 5 pp. 175-176, 1995.

[17] S. H. Jo, D. Banerjee, and Z. F. Ren, *Field emission of zinc oxide nanowires grown on carbon cloth,* Applied Physics Letters, Vol. 85, No. 8, 2000.

[18] J. Robertson, *Mechanisms of electron field emission from diamond, diamond-like carbon, and nanostructured carbon*, J. Vac. Sci. Technol. B, Vol. 17, No. 2, Mar/Apr 1999.

[19] J. Zhang, J. Tang, G. Yang, Q. Qiu, Lu-Chang Qin, O. Zhou, *Efficient Fabrication of Carbon Nanotube Point Electron Sources by Dielectrophoresis*, Advanced Materials Vol. 16, 2004.

[20] Pulickel M. Ajayan1 and Otto Zhou, *Applications of Carbon Nanotubes*, Topics Appl. Phys. 80, pp. 391–425, 2001.

[21] Yuan Cheng, Otto Zhou, *Electron field emission from carbon nanotubes*, C. R. Physique 4 pp. 1021–1033, 2003.

[22] M. Chhowalla, C. Ducati, N. L. Rupesinghe, K. B. K. Teo, and G. A. J. Amaratunga, *Field emission from short and stubby vertically aligned carbon nanotubes*, Applied Physics Letters, Vol. 79, No. 13, 2001.

[23] Jean-Marc Bonard, Thomas Stockli, Andre Chaötelain, and Jean-Paul Salvetat, *Field emission properties of multiwalled carbon nanotubes*, Ultramicroscopy 73 pp. 7-15, 1998.

[24] M.T. Kuo, P.W. May , and M.N.R. Ashfold, *Field emission site density studies of amorphous carbon films*, Diamond and Related Materials Vol. 11, pp. 1422–1428, 2002.

[25] K. B. K. Teo, M. Chhowalla, G. A. J. Amaratunga, and W. I. Milne, *Field emission from dense, sparse, and patterned arrays of carbon nanofibers*, Applied Physics Letters, Vol. 80, No. 11, 2002.

[26] P. R. Hinton, *Statistics Explained*, Routledge Publishing, 2004.

[27] W. Karain, L. Knight, D. Allred and A. Reyes-Mena, *Emitted current instability from silicon field emission emitters due to sputtering by residual gas ions*, JVST A -- Journal Vacuum Surfaces and Films, 1994.

[28] N. Miyamoto, H. Adachi, H. Nakane, and K. Yamane, *Emission stability of a field emitter array observed by an emission microscope*, (JVST B) Microelectronics and Nanometre Structures, 2003.

[29] I. J. Chung, I. B. Kang, and A. Hariz, *A simulation of the structural stability of field emission micro-tips against discharge*, Smart Material Structures, Vol. 6, pp. 628-632, 1997.

[30] T. S. Fisher, D. G. Walker, and Robert A. Weller. *Analysis and Simulation of Anode Heating Due to Electron Field Emission*. IEEE Transactions on components and packaging technologies, Vol. 26, No, 2, June 2003.

[31] H. Anton. *Calculus 5th Ed*, John Wiley and Sons publishing, 1995.

[32] David Arnold, *Curvature in Matlab*, Course in Multivariable Calculus (Math 50C), University of Redwoods, 2007.

[33] P. Hofmann, *Lecture Notes on Surface Science*, Arhus University, 05/10/2005.

[34] D. M. Garner, *Case for Support: Control of Electron Motion in Vacuum Microelectronic Devices: High Sensitivity Magnetic sensors and Other Applications*, correspondence between the companies involved in this CASE project, 2003

[35] H. H. Busta, J. E. Pogemiller and J. Zimmerman, *The field emitter triode as a displacement/pressure sensor*, Journal Micromechanics, 1993, pp. 49-56.

[36] P. J. French, *Field-emission Pressure Sensors*, WCSIM scholarships, 2006.

[37] K. L. Jensen, *An Introduction to Electron Emission Physics and Applications, lecture notes: Beam Physics Course*, Inst. Res. El. & Appl. Phys, University of Maryland, 2005

[38] I. Brodie, *Bombardment of Field-Emission Cathodes by Positive Ions Formed on the Inter-electrode Region*, Int. J. Electronics, 38(4), 1975.

[39] Nobuo Miyamoto, Hiroshi Adachi, Hideaki Nakane, and Khoichi Yamane, *Emission stability of a field emitter array observed by an emission microscope*, J. Vac. Sci. Technol. B 21.1., 2003.

[40] D. Lysenko and G. Muller, *Pressure dependence and current stability of field emission from carbon nanotubes on porous alumina*, Vacuum Nanoelectronics Conference, IVNC, pp.192-193, 2004.

[41] H. Lee and R. Huang, *A theoretical study on field emission array for microsensors*, IEEE Trans. Electron Devices Vol., 39 pp. 313-24, 1992.

[42] G. Amaratunga, *Watching the Nanotube*, IEEE Spectrum, 2003.

[43] Ed Sheibler and Theodore S. Fahlen. *Candescent's vision for field emission flat panel displays.* In Proceedings of the 14th International Vacuum Microelectronics Conference, pages 175–176, 2001.

[44] Private correspondence with J. V. Noord, http://www.grc.nasa.gov/WWW/ion/, NASA.

Chapter 3

Experimental setup and Magnetometer Evolution

The experimental apparatus is defined, followed by the evolution of the field emission magnetometer, with changes made to the original design being documented and discussed.

3.3. Experimental setup

The intention of the setup is to firstly cancel the Earth's magnetic field, allowing for an unbiased testing environment of the vacuum magnetic sensor, and secondly to test the sensors under controlled conditions of known magnetic fields in each of the Cartesian coordinates, and this is demonstrated in the sections that follow. The vacuum level of the system is kept constant at 1×10^{-6} mBar and temperature is considered room temperature (300 K) unless stated otherwise throughout these experiments.

The experimental infrastructure is shown in figure 3.1, where in order to test the vacuum magnetic sensor a closed-loop triaxial Helmholtz coil system [1, p. 285] was devised. As well as the schematic of the triaxial Helmholtz coil system in figure 3.1(a), the device orientation may also be seen in the z axis, perpendicular to the xy-plane, figure 3.1(b) also shows the experiment in the Laboratory.

A series of a General Purpose Interface Bus (GPIB) cards and cables are used in a closed-loop system of magnetic field measurement. The programming language, LabVIEW [2, 3] is used to control a series of Keithley instruments (Keithley models 236 and 6430 used) that control the triaxial Helmholtz coil system that produces magnetic fields. The reference [4] and Device Under Test (*DUT*) sensors are held in close proximity within these magnetic fields, the reaction of which is fed back into the system by a set of Kiethleys allowing for measurements against any magnetic field to be applied and

recorded. The cables between the Kiethleys meters and vacuum system are kept as short as possible and are shielded to minimise noise within the system.

The fields generated by the triaxial Helmholtz coil system are governed by equation (3.1), where magnetic field for each pair of coils is responsible for the magnetic field through x, y and z coordinates of the vacuum test chamber, i.e. it is assumed that the superposition of the three separate fields, B_x, B_y and B_z are given by equation (3.1) for each Helmholtz pair of coils. It is well documented that by placing the coils apart the same distance, *d*, as the radius of the coils, *r*, that magnetic field calculations for the centre of the coil are linear and homogenous within the centre of the coils [1, p. 285], as seen in figure 3.1(d).

Placing known parameters into equation (3.1) allows the governing equation to be simplified to be proportional to the current flowing through the coil pairs, the component magnetic field parts consist of (*B* in Tesla):

$$B = \begin{pmatrix} B_X \\ B_Y \\ B_Z \end{pmatrix} = \begin{pmatrix} \lambda \\ \lambda \\ \lambda \end{pmatrix} \begin{pmatrix} I_X \\ I_Y \\ I_Z \end{pmatrix} \quad \text{Tesla} \qquad \text{Eq. 3.1}$$

Where:

$$\lambda = \frac{0.72 \mu N}{r} \cong 2.5x10^{-4} \quad \text{T/A}$$

With constants, $\mu = 4\pi x 10^{-7}$ Tm/A (permeability of free space), $N = 70$ (number of turns per coil), $r = 0.254$ metres (radius of each coil). Therefore using this system, for $B_z \approx 1$ mT, I must equal 4 Amps, and cancellation of the Earth's magnetic field requires approximately 200 mA in the x and y pairs of coils, i.e. λ x 200 mA = 50 μT.

(a) Schematic overview of measurement system

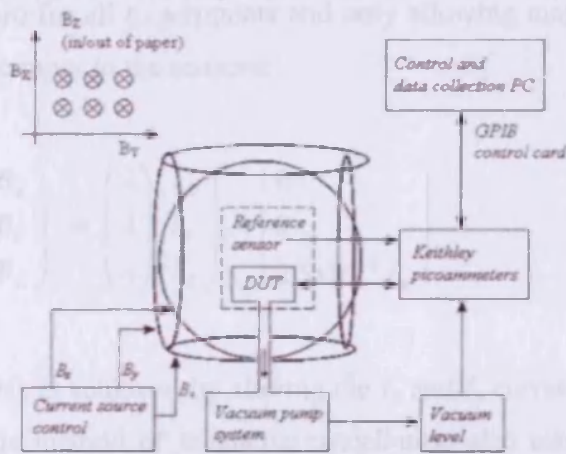

(b) Reference sensor and DUT within the system

Reference sensor

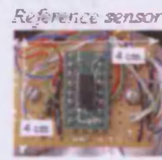

DUT:

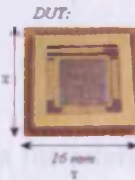

(c) Triaxial Helmholtz coil system

(d) Calculated magnetic field across a pair of Helmholtz coils

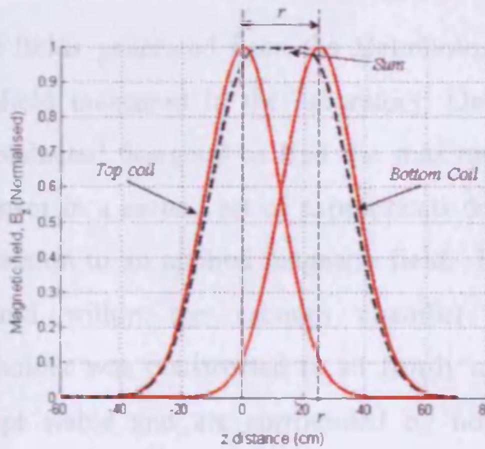

Figure 3.1. (a) A schematic view of the setup for the triaxial Helmholtz coil system used to apply magnetic fields, (b) The reference sensor and orientation of reference sensor within the system, (c) A photograph from the laboratory showing the completed Helmholtz coil system, and (d) A graph showing the z-distance and corresponding magnetic field for a single pair of Helmholtz coils.

Equation (3.1) is further simplified by setting the magnetic field within the xy-plane to zero for all experiments and only allowing magnetic fields to pass through the z-axis as the input to the sensors:

$$\begin{pmatrix} B_X \\ B_Y \\ B_Z \end{pmatrix} = \begin{pmatrix} \lambda \\ \lambda \\ \lambda \end{pmatrix} \begin{pmatrix} I_X \\ I_Y \\ I_Z \end{pmatrix} = \begin{pmatrix} 0 \\ 0 \\ 2.5x10^{-4}\, I_Z \end{pmatrix}$$

This is achieved by altering the I_x and I_y currents so that the reference sensor reads zero, this method of magnetic cancellation also takes account of any abnormalities in local magnetic fields.

Using the setup described the magnetic fields generated from the Helmholtz coils are adjusted until they cancel the Earth's field measured in the laboratory. Once this is achieved a series of experiments are conducted designed to find the maximum anode current, and then B_Z is applied to the sensor in a second set of experiments designed to test for the vacuum magnetic sensors reaction to an applied magnetic field. Figure 3.2 shows a close up of the *DUT* held within the vacuum chamber. Here, a Polytetrafluoroethylene (PTFE) device holder was constructed to sit firmly around the DUT so that the devices could be kept stable and are surrounded by non-gaseous materials under high vacuum [8]. The PTFE holder was then attached to a testing-PCB which is wired to an electrical feed through allowing for access to the device. This entire structure was then placed within a sealed vacuum chamber, itself then placed within the above triaxial Helmholtz coil system.

(a) Device and PTFE holder

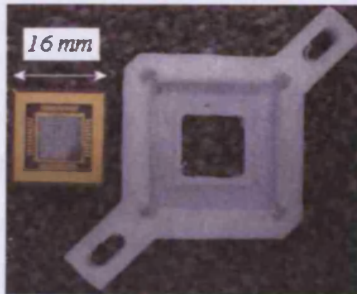

(b) Device and testing-PCB

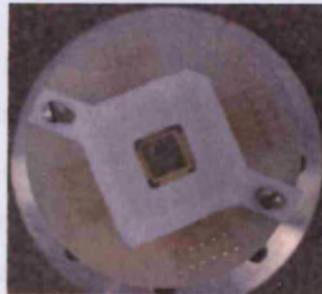

(c) Wiring inside Vacuum chambe

(d) Completed setup

Figure 3.2. Stages of the DUT within the vacuum chamber, showing:

(a) Device and PTFE holder.

(b) PTFE holder and PCB.

(c) Wiring inside the test chamber.

(d) Completed test chamber as seen from the outside showing all components.

3.2. Fabrication overview

The Layout Edit package [5] was used in the layout design and manufacture for the devices presented here and manufactured at the INNOS fabrication facility at MiPlaza in Eindhoven [6]. The fabrication schematic of the lateral field emission magnetometer is shown in figures 3.3 – 3.6, accounting for the manufacture of the second generation only (differences between the first and second generations are discussed in the next section). The starting material was 150 mm diameter Silicon On Insulator (SOI) wafers consisting of a 300 nm thick heavily doped active top layer, 2 μm of buried oxide, and 625 μm thick handle substrate. On arrival of the SOI wafers, the top and substrate layers are recorded as having a resistance of 1 Ohm.cm, both of which are n-type (phosphorous) doped. Processing began with an additional phosphorous doping of the top silicon layer to reduce the device sheet resistivity to 10 Ohms/square or $3x10^{-4}$ Ohm.cm, and this 3,000 order of magnitude decrease in top layer resistivity makes it highly conductive to the same degree as some pure metals and alloys such as copper, aluminium and nichrome [7, 8], allowing for the metallic Fowler Nordheim model to be used [9 - 13]. The low resistivity of the top layer corresponds to total phosphorous concentration of 1% of all atoms within the top layer being phosphorous with the reaming atoms being silicon [8 p. 200].

It is assumed that the distribution of doping is uniform throughout the active layer, so that the electron supply is consistent throughout the top layer. The probability of electron emission is chiefly governed by protrusion sizes, not protrusion location within the active layer as indicated in figure 3.3 where the predominant emission site is that of the tip apex. It is also assumed that of the work function of silicon is constant at 4.52 eV regardless of doping level. A compilation of work functions for materials with similar conductivities such as copper and aluminium has been complied by Kaye and Laby, indicating small variance between metallic materials [Kaye and Laby, 35].

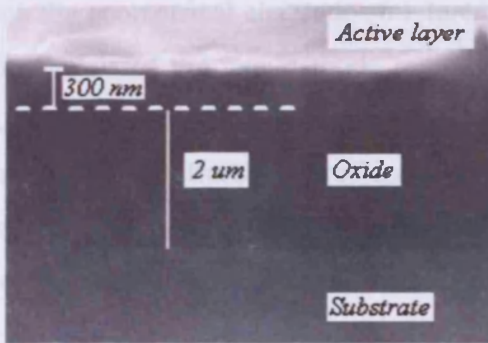

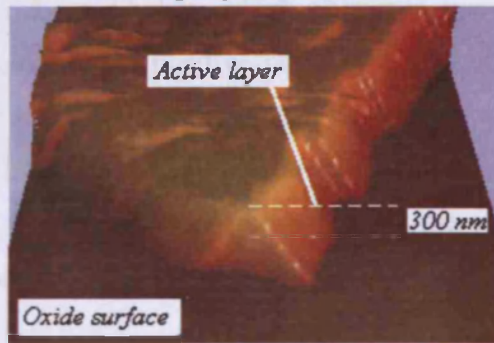

Figure 3.3. Showing (a) An electron micrograph of the side profile, and (b) The AFM profile of an example tip.

Having deposited the silicon nitride (positive mask), in which the electrode spacings are optimised by simulation, LOCal Oxidation of Silicon (LOCOS) was used to completely oxidise the top silicon-oxide layer in the areas around the electrode spacings. Due to the nature of LOCOS growth, this forms a very sharp tip at the end of the silicon gate electrode [6 and 1 pp. 3-5], as shown in the cross-section schematic in figures 3.4(b):

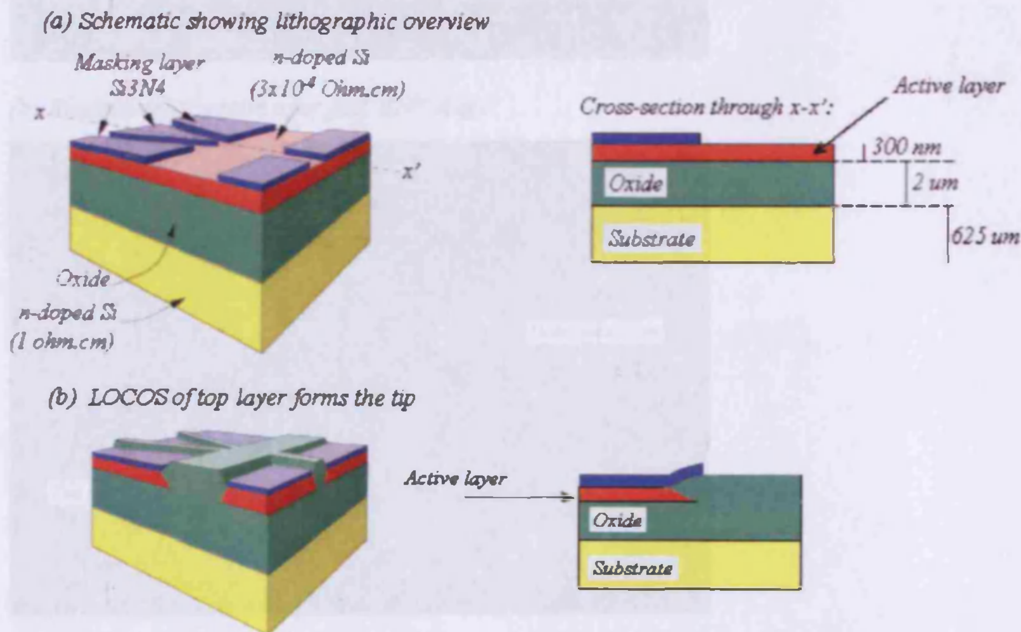

Figure 3.4. Showing (a) Schematic mask layer overview, and (b) The LOCal Oxidation of Silicon stage.

High resolution stepper lithography and fluorine based dry etching was then performed to etch the geometrical electrode structures as indicated below, where a electron micrograph shows part of the gate-cathode region (including the positive masking layer) in figure 3.5(a). The remaining Si_3N_4 masking layer and SiO_2 are stripped in hot phosphoric acid followed by buffered hydrofluoric acid (BHF) leaving the isotropic undercut of the geometry of approximately 2 μm, though with some oxide remaining on the substrate floor as shown in the electron micrograph below in figure 3.5(b):

(a) Electron micrograph after dry etching

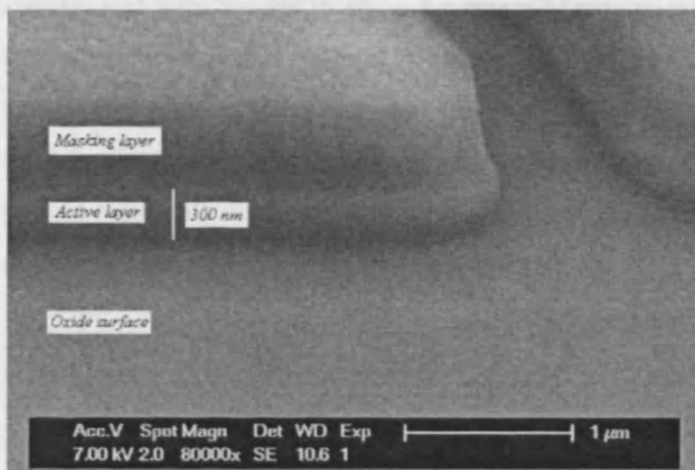

(b) Electron micrograph after first BHF stage

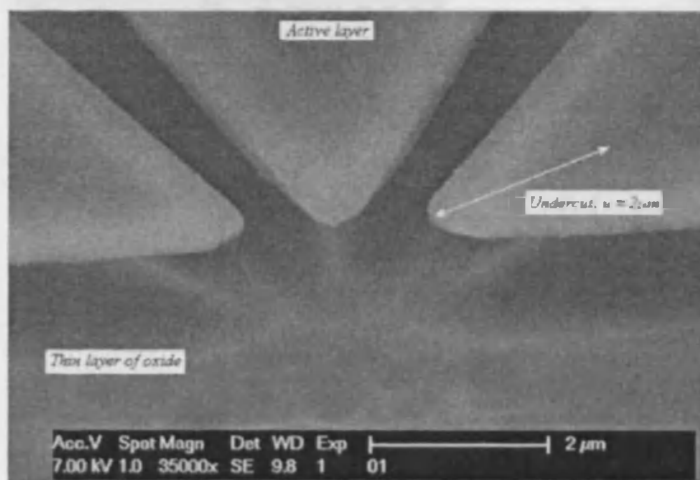

Figure 3.5. Showing (a) The schematic LOCOS stage, and (b) A supporting electron micrograph post BHF stage.

The metal contact pads were formed by magnetron sputter deposition of a 350nm thick layer of Chromium-Gold (Cr-Au), patterning the pad configuration by I-line stepper lithography and then wet etching the metal to leave the isolated pads. The final wafer processing step consisted of a long etch in BHF to remove the remaining SiO_2 surrounding the device electrodes and substrate floor, leaving the completed lateral vacuum magnetic field sensor with an isotropic tip undercut of 2 μm (the same as the oxide thickness).

Finally individual devices were selected and sawn from the wafer, mounted in chip carriers and wire bonded to allow for device testing as indicated in figure 3.6. Because of the nature of processing lateral structures such as those devices presented here, i.e. the same fabrication process step and therefore the same photolithographic mask layer is used for the top layer, the main advantage of lateral designs is that the cathode tip and the split in the anode are automatically aligned, and issues with misalignment-induced offset that occur with vertical structures are avoided.

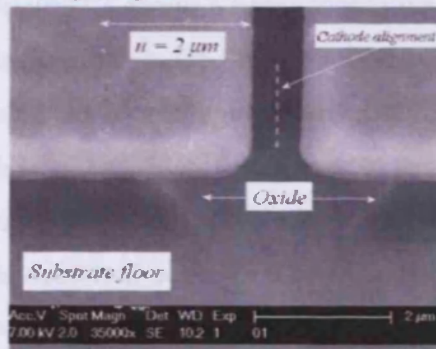

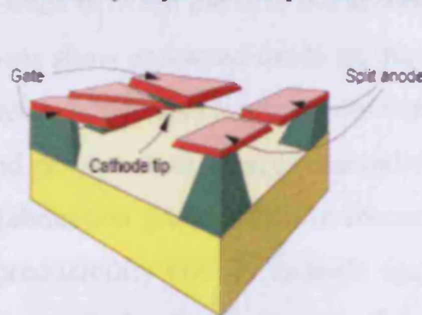

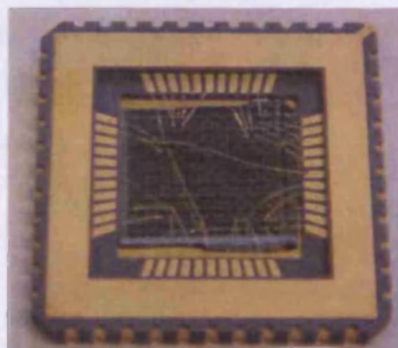

Figure 3.6. Showing electron micrographs, schematic and photograph of the anode section (top left), schematic of completed device (top right), bond pad (bottom left), and completed package (bottom right).

3.3. Failure analysis and device improvement

The technique described above is a variation of the first batch of devices, where initially the oxide and top layer was grown on a bulk substrate and no dry etch was employed. This was found to lead to a number of device issues documented below. Within this context, the first generation of devices were constructed from a thermally grown oxide at INNOS on a substrate, while the second generation of devices were SOI wafers. Although the oxide thickness is similar in both generations, i.e. 2 μm thick, the differences in quality are far greater for the second generation due to SOI preparation, leading to less current leakage, lower capacitance, and higher breakdown voltage threshold [36]. On further inspection between the two generations, it has been noted the device quality is of far greater in the centre of the wafer than the edge. This was true of both generations, though the overall quality in the second generation was greater than that of the first for reasons discussed below.

Figure 3.7 shows a basic qualitative difference between the first and second generation of devices. Here, the first generation of devices show unwanted oxide on the substrate floor, far more edge-roughness around all electrodes which also leads to unwanted debris across the device. This is in contrast to the second generation of devices that indicates overall far more controlled fabrication. The above fabrication process for the second generation of devices is thought to allow for good reproducibility both in cathode tip sharpness, and controlling the short cathode-gate interelectrode distances (of the order of one micrometer), although experiments by the author have shown that unwanted protrusions on the cathode tip surface do lead to tip damage and that these protrusions are largely difficult to control during fabrication. Cathode tip damage and contamination are further discussed in chapter 3.3.1. *Fabrication issues.*

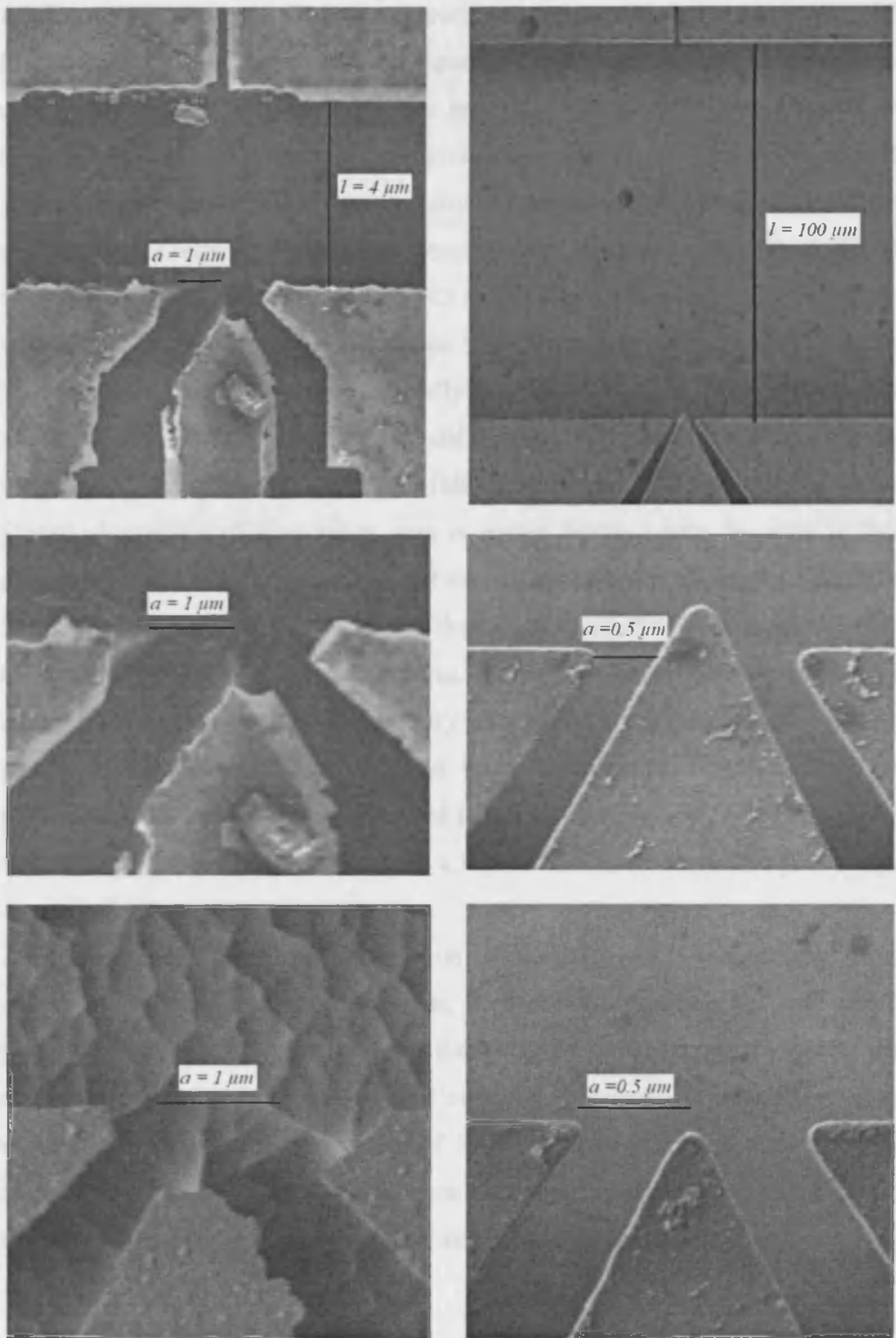

Figure 3.7. Comparison of the first and second generation of devices (left and right respectively).

Adding to the above qualitative comparison is a quantitative measurement of emitted cathode current over time. As with figure 2.9, the cathode current is recorded over a twelve hour period for the new device and superimposed on figure 3.8(top), where the mean emitted current from both generations of devices are of the order of 1 uA, though a slightly higher mean for emitted current for the first generation of devices than the second. This is reflected in the corresponding mean emission area radii of ~10 nm for the first generation of devices [P. French, 15 and 16], and 100 nm for the second generation, with higher current densities associated with lower emission areas. It is believed that higher current densities across atomically sharp emitting sites such as those indicated in above in figure 3.7(left side), and especially from devices whose radius of curvature is of the order of 10 nm, have led to emitter failure by thermal breakdown [17 p. 882].

Statistical analysis of time series data is shown below where the data is Gaussian in nature, with the highest probability of emission being the mean. As seen from figure 3.8(bottom), the standard deviation for the second generation of devices is approximately half that of the first generation of devices, and because both data sets have been collected under very similar conditions, i.e. very similar vacuum level, input voltages, device geometry and operation conditions at room temperature, implying that the second generation of devices is more controlled in terms of fabrication where a higher deviation of measured current is associated with a higher number of unwanted protrusions around the cathode.

Although this difference in distribution is recorded and illustrates the difference in operation between the two generations, because devices presented here function as a percentage difference of anode current the distributions of cathode current have no effect on device operation for relatively low standard deviations. However, for much higher standard deviations the probability of higher current densities results, i.e. electrical currents of the order of 1 mA across relatively small cathode tip sizes are possible under these circumstances and can cause thermal breakdown [17 p. 882, 18].

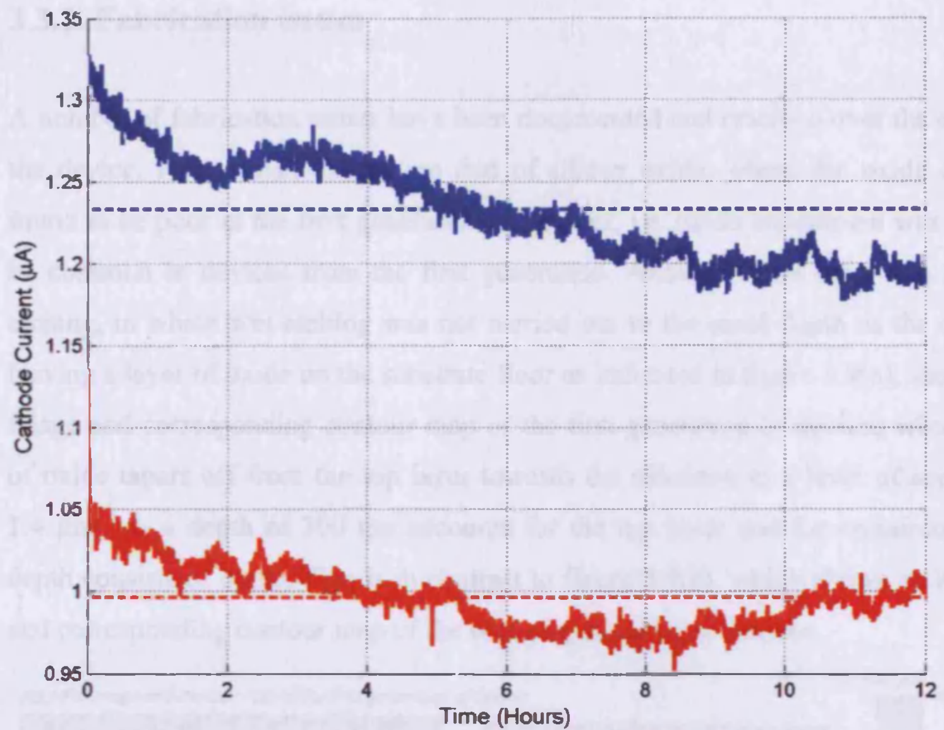

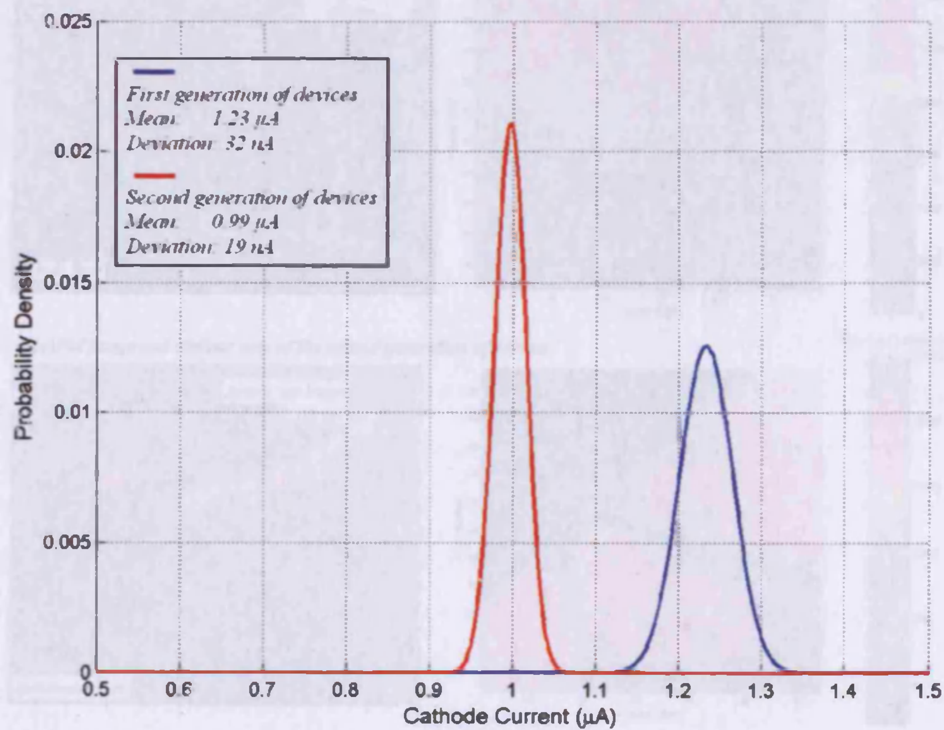

Figure 3.8. Comparison of the first and second generation of devices in terms of cathode current over a twelve hour period (top and bottom respectively).

3.3.1. Fabrication issues

A number of fabrication issues have been documented and resolved over the evolution of the device. Predominant issues are that of silicon oxide, where the oxide quality was found to be poor in the first generation of devices, i.e. oxide breakdown was believed to be common in devices from the first generation. Another oxide issue was that of wet etching, in which wet etching was not carried out to the same depth as the oxide level, leaving a layer of oxide on the substrate floor as indicated in figure 3.9(a), showing AFM image and corresponding contour map of the first generation of devices where the level of oxide tapers off from the top layer towards the substrate to a level of approximately 1.4 µm, i.e. a depth of 300 nm accounts for the top layer and the remaining (1.1 µm) depth consists of oxide. This is in contrast to figure 3.9(b), which shows an AFM image and corresponding contour map of the second generation of devices,

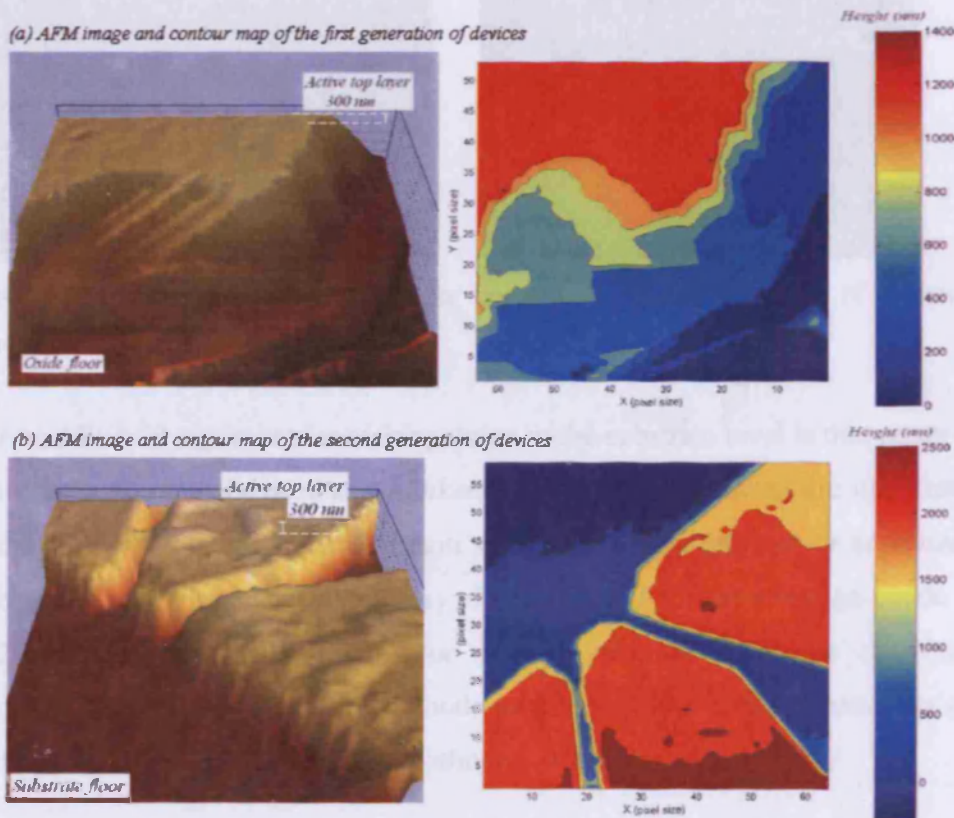

Figure 3.9. AFM and corresponding contour plots for (a) A sample from the first generation of devices and (b) A sample from the second generation of devices. Both of which indicate the degree of verticality of the side edge.

As seen, the drop between the top layer and substrate floor is much sharper in the second generation of devices as the supporting oxide is not detected by AFM in the second generation samples. It is believed that poor oxide is responsible for leakage current, which may prevent field emission if the oxide offers little resistance to charge flowing between the substrate and gate electrodes.

One argument for etching down to the substrate is that of a thin oxide layer appearing on top of the substrate surface as shown in figure 3.10. When used as a steering electrode, the substrate may be required to draw all electrons into itself or electrons may simply strike this layer. When this occurs the thin layer of oxide may retain charge, making the device act as a capacitor, leading to unstable electron trajectories.

Figure 3.10. Comparison of cathodes for the first and second generation of devices (left and right respectively).

An additional argument for etching down to the substrate level is that positive voltages on the substrate may be used as a *blinker*, where emitted electrons are intentionally drawn to the substrate for any desired reason such as device alignment or adjustment while still being in operation. The device may also be used as a field emission triode amplifier [19, 20, 21], where an input capacitor may provide AC signals to the biased substrate, draining the e-beam from the cathode-gate region (the cathode being the current source and gate being the output) to the cathode-substrate region.

Other issues that affect device operation are that of contamination of clean surfaces which can severely affect field emission characteristics. The most common source of contamination is dust particles from preparation as shown in figure 3.11(a), which offer lower resistance paths creating resistor-like characteristics. Another common fabrication issues with the first generation of devices are that of stitching shown in figure 3.11(b), which often comes apparent as an open-circuit during testing. Manufacturing issues such as that shown in figure 3.11(c) have been common with the first generation of devices. These include a range of issues within the device including defects in the wafer, mask layer issues, contamination, unintentional emission sites and fused anodes, where the separation of the anode has failed due to processing issues. Correspondence with INNOS [6], the manufacturer of the devices revealed that the minimum anode split separation is of the order of 0.5 μm otherwise bridging of electrodes results ruining devices operation. Most of these issues may be resolved by simple changes in fabrication and handling which are reflected in the much higher quality of the second generation of devices.

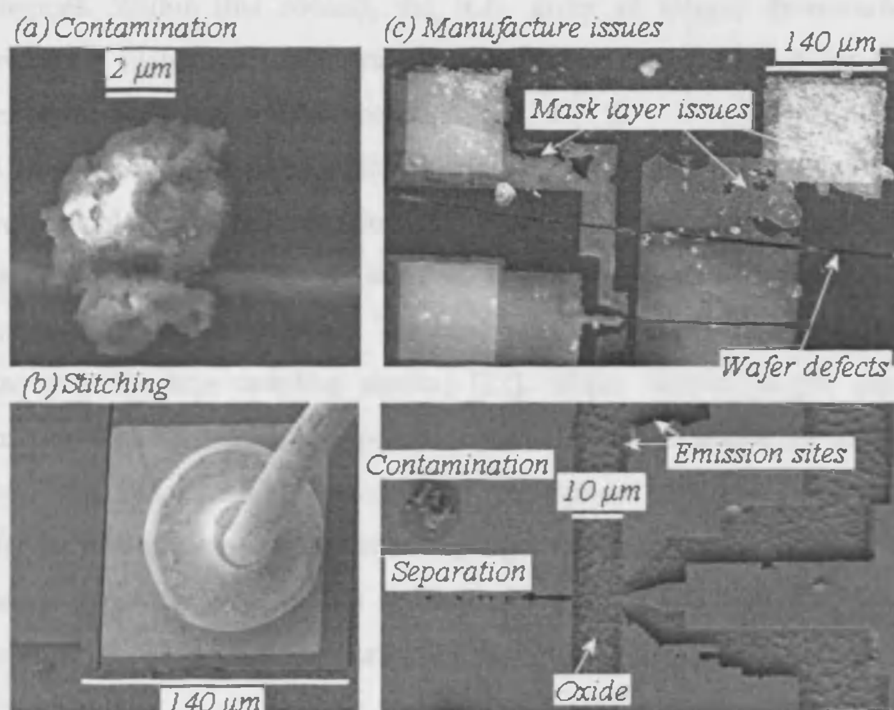

Figure 3.11. Showing (a) Contamination, (b) Stitching, and (c) Manufacture issues found in the first generation of devices (examples of contamination, separation failure, presence of oxide and unwanted emission sites are shown).

3.3.2. Cathode tip structure and stability

From the previous chapters it is clear that cathode current and structure are vital to the success of the device, with the cathode being the sole electron source and the orientation of the cathode apex giving rise to the sensitivity of the device.

In order to quantitatively analyse cathode tip structure and further illustrate differences between the two generations of devices, an algorithm for cathode tip perimeter roughness is carried out. This is achieved by measuring the Hausdorff Dimension (*HD*) [22 - 25] of the cathode tip curve which gives the degree of roughness as a fractal dimension. The fractal dimension is a positive (non)-integer that describes the complexity or irregularity of the cathode perimeter, and is due to the geometry of the perimeter being non-Euclidean. Specifically, the *H.D.* gives a numerical estimate of the cathode perimeter roughness in which the degree of roughness is directly proportional to parasitic emission sites. Electron micrograph evidence implies higher perimeter roughness for the first generation of devices and lower perimeter roughness for the second generation of devices. Within this context, the *H.D.* gives an integer measurement for Euclidean surfaces, such as 1 for a straight line, 2 for a square, and 3 for a cube, making the expected *H.D.* values bound between, $1 < HD < 2$.

Using the cathode tip samples shown in figure 3.10, areas thought most likely to be responsible for field emission and device failure are arbitrary selected from both generations of devices, i.e. areas of approximately equal sizes are selected from the cathode tip of both samples. The algorithm used to calculate the Hausdorff Dimension involves the box counting method [22], where sample images from figure 3.10 are uploaded to Matlab[6]. Image processing within Matlab allows for the perimeter outline to be found and a grid of N squares is superimposed over the resultant image as shown in figure 3.12(bottom). A box counting algorithm was then devised to count the occupied squares that the edge passes through giving, $N(s)$. This is continued for an increasing number of squares (up to an arbitrary, $N = 20$) as shown in figure 3.13:

[6] Code given in *Appendix A.2. Matlab code.*

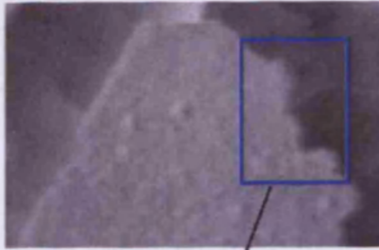

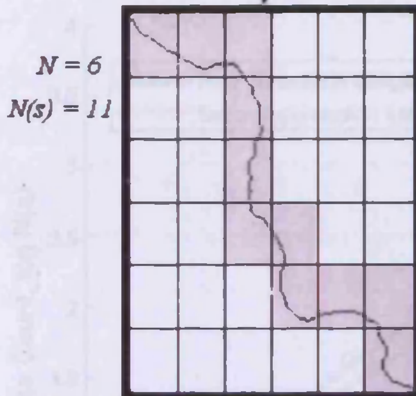

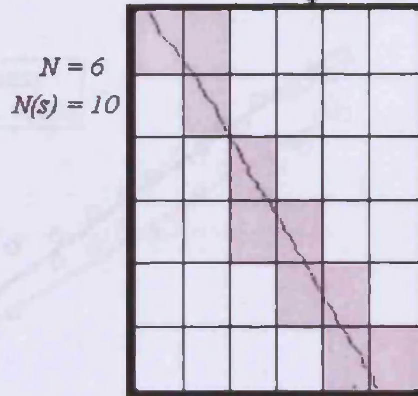

Figure 3.12. Showing the selected images (top) for the first and second generation of devices (blue and red lines respectively), and box counting method used to calculate occupied boxes (bottom).

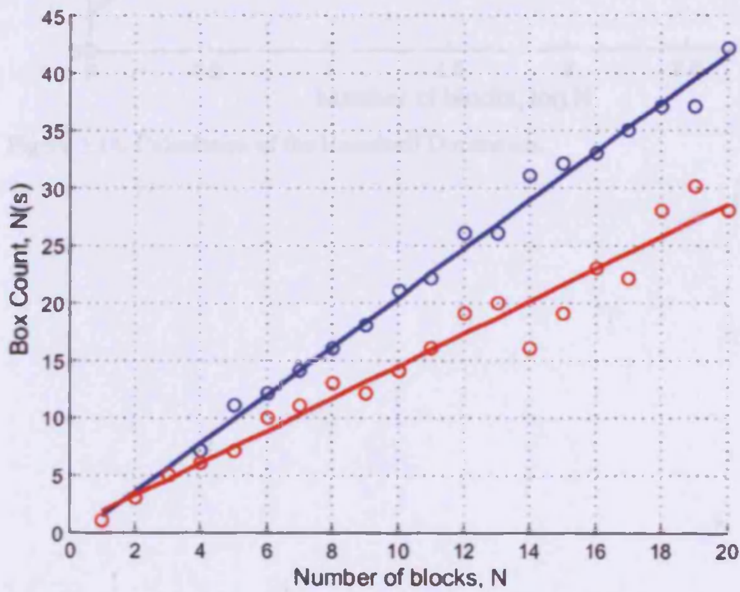

Figure 3.13. Showing the resultant graph of occupied boxes, $N(s)$, against box count N (for one side of the box shown above).

The fractal dimension is given by the gradient of the logarithm of the number of squares, *log N*, over the number of squares occupied by the edge, *log N(s)*, as given by equation (3.2) and shown in figure 3.14:

$$HD = \lim_{N \to \infty} \frac{\log N}{\log N(s)} \qquad \text{Eq. 3.2}$$

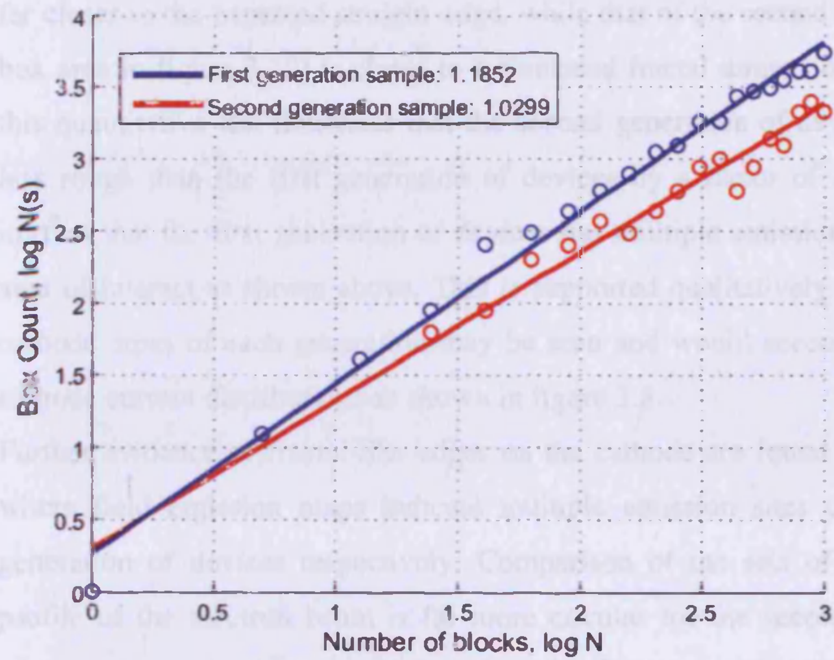

Figure 3.14. Calculation of the Hausdorff Dimension.

Applying this algorithm to the two individual images shown above gives fractal dimensions for the first (HD_1) and second (HD_2) generation of devices of:

$HD_1 = 1.1852$

$HD_2 = 1.0299$

Indicating that the edge of the second generation sample (red box area in figure 3.12) is far closer to the expected straight-edge, while that of the second generation sample (blue box area in figure 3.12) is closer to a truncated fractal dimension on this scale. Overall, this quantitative test illustrates that the second generation of devices may be considered less rough than the first generation of devices by a factor of approximately 0.8. This implies that the first generation of devices has multiple emission sites around the boxed area of interest as shown above. This is supported qualitatively by figure 3.7 where the cathode areas of each generation may be seen and would account for the differences in cathode current distributions as shown in figure 3.8.

Further evidence of fractal-like edges on the cathode are found in figure 3.15(a and b), where field emission maps indicate multiple emission sites on the first and second generation of devices respectively. Comparison of the sets of images shows that the profile of the electron beam is far more circular for the second generation of devices where one emitter area dominates, than the first generation where numerous emitting sites are present and non-uniform emission can be seen.

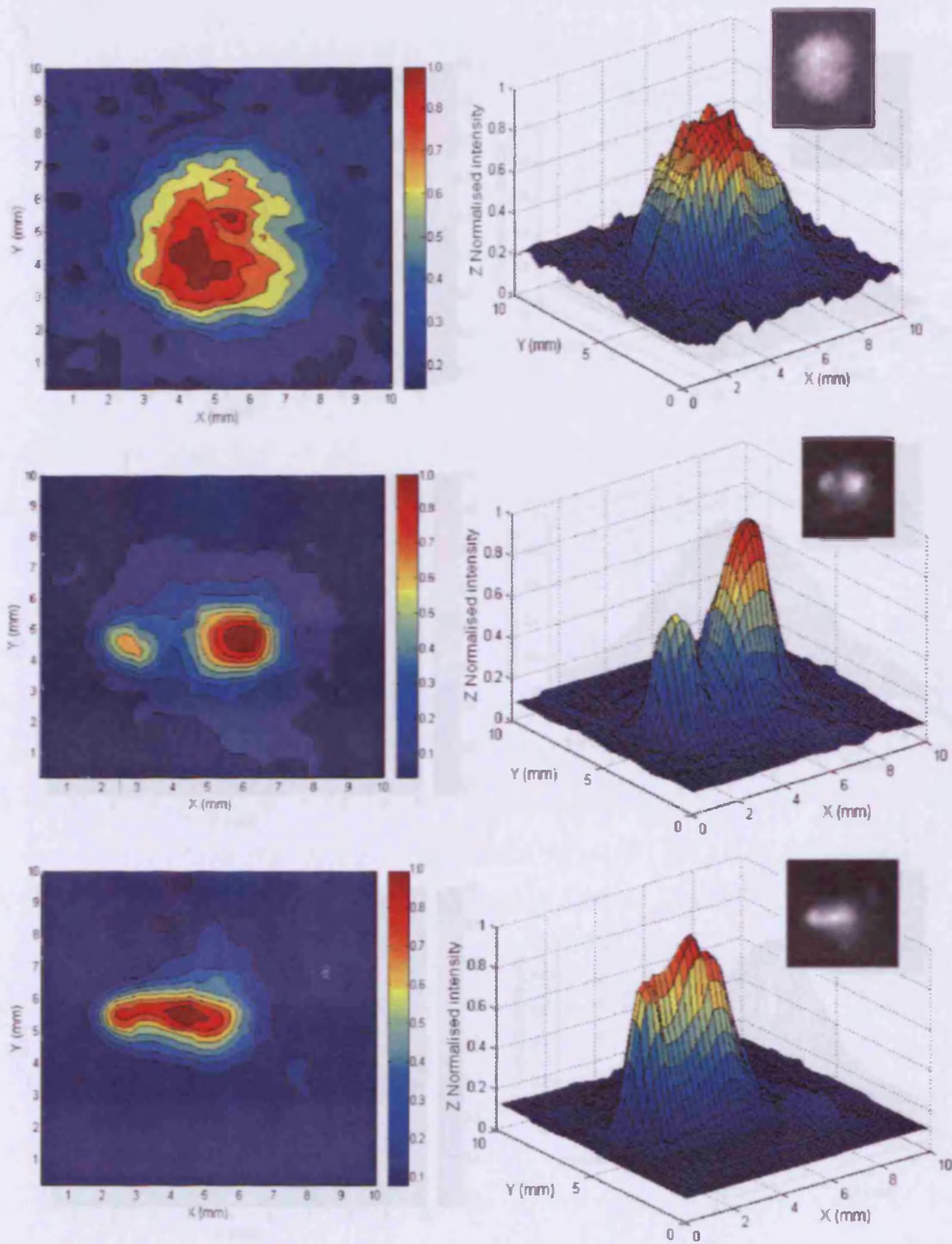

Figure 3.15(a). Normalised field emission maps indicating the stochastic nature of field emission for the first generation of devices.

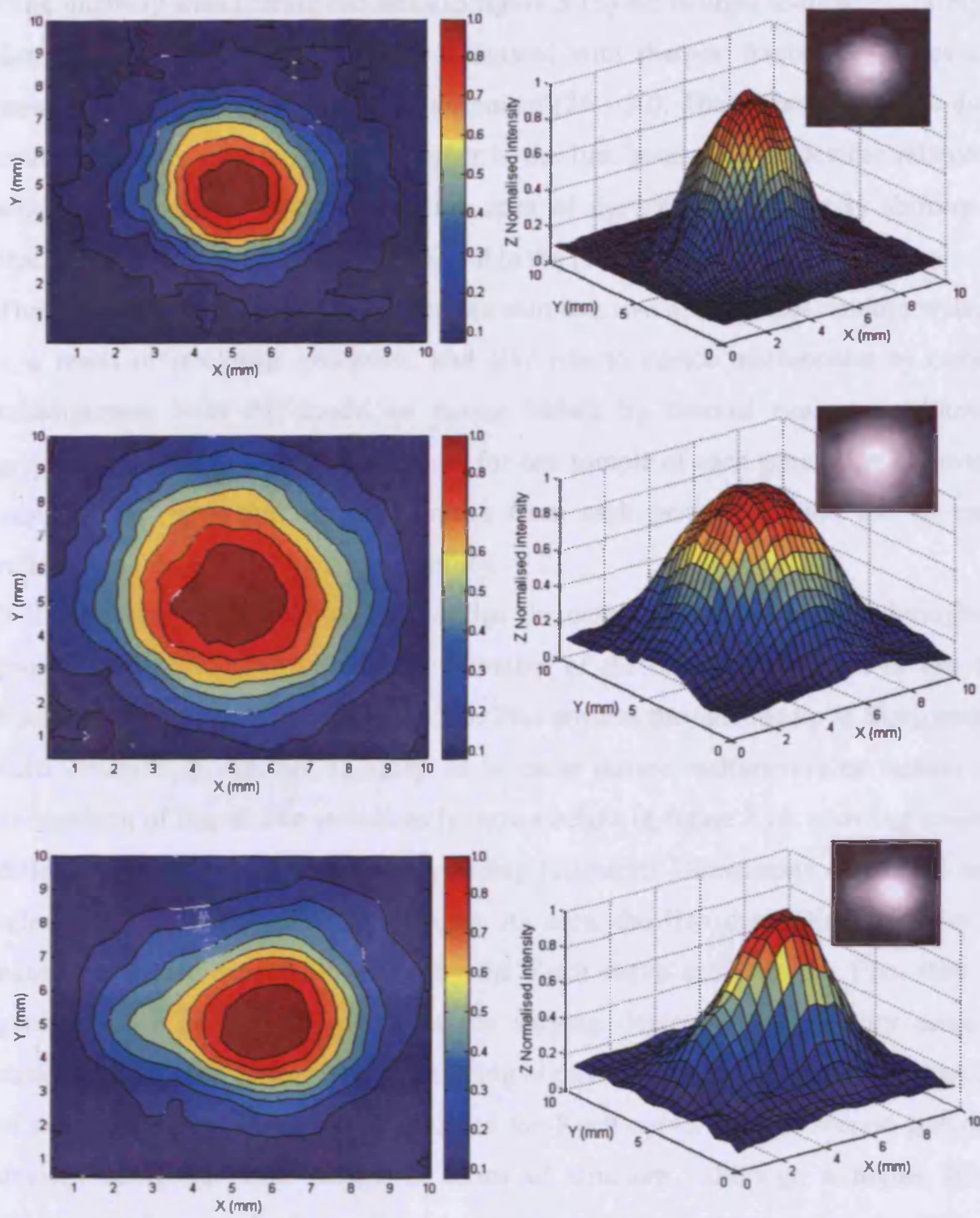

Figure 3.15(b). Normalised field emission maps indicating the stochastic nature of field emission for the second generation of devices.

The emission maps shown also indicate the variance of peak intensity in the xy-plane. Peak intensity sites (darker red areas in figure 3.15) are thought to directly correspond to dominant emitting sites, which are associated with sharper, fractal like edges as these areas offer greater electric field enhancement [26 - 30]. The variance of these dominant emitting sites is seen to be much higher in the first generation of devices relative to the second, and may be thought of as the apex of the cathode effectively shifting due to stochastic processes discussed above, and in the previous chapter.

These shifts in peak intensity location are akin to a two dimensional random walk, which is a result of stochastic processes, and give rise to device malfunction by cathode tip misalignment with the anode, or device failure by thermal runaway. Although the graphics generated from figure 3.15 are for one sample of each generation of devices, the samples used represent typical samples from each generation, and are an empirical reflection of device structure and stability.

It is for these reasons outlined above that the cathode structure chosen throughout this project deliberately has a radius of curvature of the order of hundreds of nm with no fractal-like edges as shown in figure 2.5. This ensures the cathode tip is sharp enough for field emission though not so sharp as to cause device malfunction or failure. A final comparison of fractal-like structures is shown below in figure 3.16, showing a number of different structures and their corresponding Hausdorff Dimensions calculated from the selected black boxes within the images. As seen, the Hausdorff Dimension for carbon nanotubes is the highest, followed by the Koch curve and then the first, then second generation of devices. This reflects the varying degrees of complexity across these structures, with the carbon nanotubes being highly complex in nature, the first generation of devices sharing similar fractal traits to the Koch curve, and the second generation of devices being the most simple in terms of structure. Although a higher Hausdorff Dimension for a cathode structure is associated with higher current densities due to greater field enhancement [29], this leads to instability within the structure and non-linearity in electron emission direction and magnitude, leading to cathode tip misalignment and a higher probability of thermal runaway [29, and 32 - 34].

A major assumption here is that true fractals; mathematical objects as shown in figure 3.16(b) are scale invariant and self-similar, when in fact the cathode tip fractals presented are loosely self-similar and thus (loosely) scale invariant, i.e. the fractals presented here are truncated. Because we have assumed that the truncated fractals here are scale-invariant and self-similar, Hausdorff Dimensional measurements are taken on areas thought to be most fractal-like - areas that thought to give rise to non-linear current densities, which are chosen by inspection of the electron micrographs and consequently must be used only as a first order guide in quantitative cathode tip analysis:

(a) Carbon nanotube field emitter
Hausdorff Dimension: 1.4834

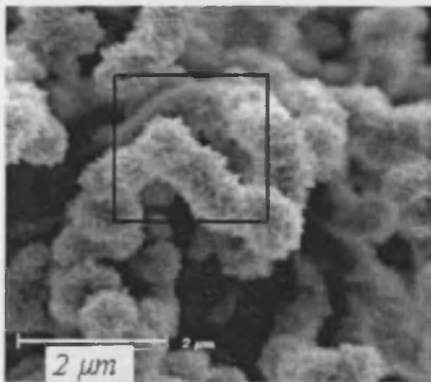

(b) Koch curve
Hausdorff Dimension: 1.2619

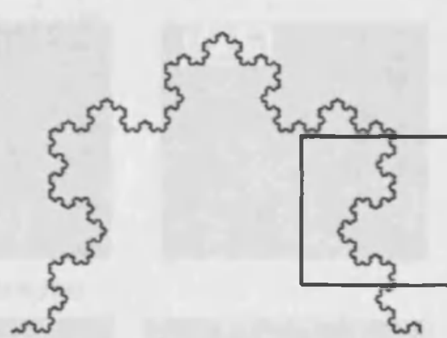

(c) First generation sample
Hausdorff Dimension: 1.1841

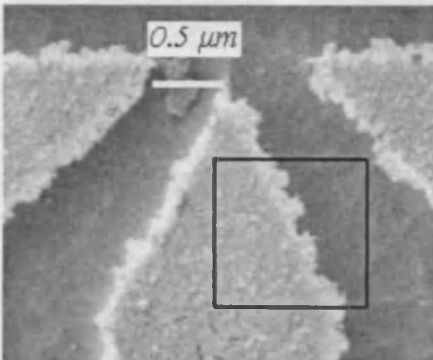

(d) Second generation sample
Hausdorff Dimension: 1.0627

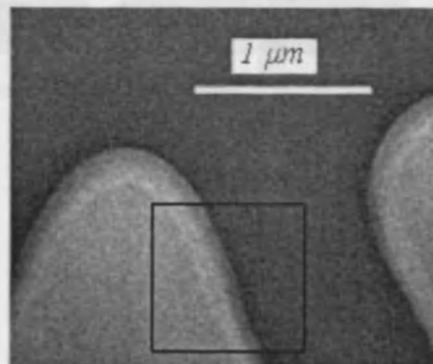

Figure 3.16. Showing a number of structures with corresponding Hausdorff Dimension, with, (a) Carbon nanotube field emitter, from [31], (b) Koch curve structure, from [22], and samples from the first and second generation of devices.

Figure 3.17 shows a selection of cathode tip samples reflecting the degrees of fractal structures in cathode tip shapes. These are predominantly triangular in shape around the apex for the first generation as seen in figure 3.17(a) and elliptical for the second generation as indicated in figure 3.17(b).

(a) First generation cathode tip samples

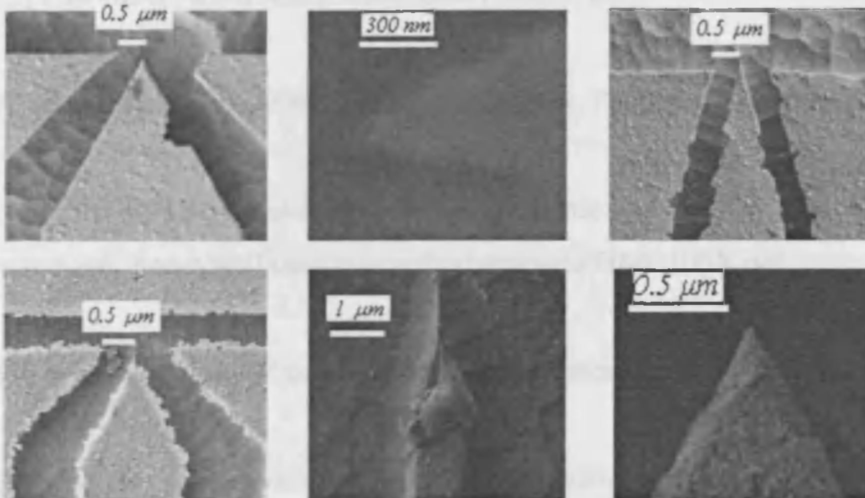

(b) Second generation cathode tip samples

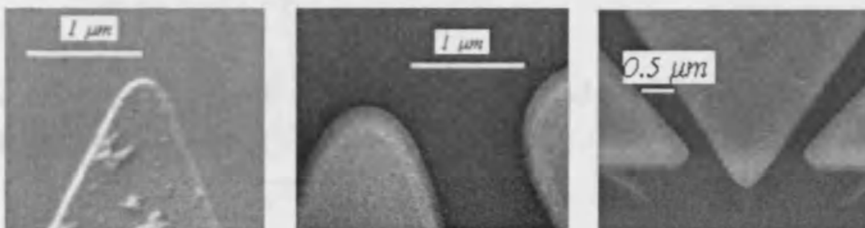

Figure 3.17. Showing a selection of cathode tips for the first generation (a) and second generation (b) of devices.

3.4. References

[1] H. D. Young and R. A. Freedman, *University Physics*, Addison-Wesley publishers, 2000.

[2] LabVIEW, www.nationalinstruments.com, 2005.

[3] B, Mihura, *LabVIEW for Data Acquisition*, Prentice Hall, 2001.

[4] HMC1053 3-axis magnetoresistive magnetic sensor by Honeywell, www.ssec.honeywell.com/magnetic/datasheets/HMC105X.pdf

[5] J. Thies, *LayoutEditor*, www.layout.sourceforge.net, 2006.

[6] Private communication with Dr. Graham Ensell, head of INNOS fabrication, University of Southampton.

[7] Richard C. Jaeger, *Introduction to Microelectronic Fabrication 2nd Edition*, Prentice Hall Publishing, 2001.

[8] N. Braithwaite, *Electronic Materials*, Open University Press, 1990.

[9] R. Gomer, *Field Emission and Field Ionization*, Oxford University Press, London, 1961.

[10] H. Busta, *Review of Vacuum microelectronics*, Amoco Research Centre, 1992

[11] Kevin L. Jensen, Course Notes: An Introduction to Electron Emission Physics And Applications, Naval Research Laboratory, Washington, 2005.

[12] K. L. Jensen, E. G. Zaidman, M. A. Kodis, B. Goplen and D. N. Smithe, *Analytical and seminumerical models for gated field emitter arrays*, J. Vac. Sci. Technol. B, Vol. 14, No. 3, 1996.

[13] Private communication with Dr. Kevin L. Jensen, Naval Research Laboratory, Washington.

[14] R. E. Neidert, P. M. Phillips, S. T. Smith, and C. A. Spindt, *Field Emission Triodes*, IEEE Transactions on Electron Devices, Vol. 38, No. 3, 1991.

[15] G. Hui, D. M. Garner, P.J. French, *Design of a CMOS-Compatible Field-Emission Magnetic Sensor with Adjustable Sensitivity*, Technical Digest of the 16th International Vacuum Microelectronics Conference, 71-72, 2003.

[16] P. J. French, *Poster Presentation on Field-emission Magnetic Sensors*, IEEE Sensors Conference, Vienna, 2004.

[17] F. Charbonnier, *Arcing and voltage breakdown in vacuum microelectronics microwave devices using field emitter arrays: Causes, possible solutions, and recent progress*, J. Vac. Sci. Technol. B 16.2., 1998.

[18] W. P. Dyke, *The field emission initiated vacuum arc experiments*, Physical Review, Vol. 91, 1993.

[19] R. E. Neidert, P. M. Phillips, S. T. Smith, and C. A. Spindt, *Field Emission Triodes*, IEEE Transactions on Electron Devices, Vol. 38, No. 3, 1991.

[20] Chih-Wen Lu and Chung Len Lee, *A Physical Simulation Model for Field Emission Triode*, IEEE Transactions on Electron Devices, Vol. 45, No. 10, 1998.

[21] A. Wisitsora, W. P. Kang, J. L. Davidson, D. V. Kerns, and T. Fisher, *Diamond Field Emission Triode with low gate Turn-on Voltage and High Gain*, IEEE Sensors, 2001.

[22] Hausdorff Dimension, http://mathworld.wolfram.com/HausdorffDimension.html.

[23] M. M. Dodson and S. Kristensen, *Hausdorff Dimension and Diophantine Approximation*, Proceedings of Symposia in Pure Mathematics, American Mathematical Society, 2003.

[24] O. Knill, *Dynamical systems lecture notes Math118*, dept. of mathematics, Harvard University (spring semester), 2005.

[25] V. Constantoudis and G. P. Patsis, *Line edge roughness and critical dimension variation: Fractal characterization and comparison using model functions*, J. Vac. Sci. Technol. B 22.4., 2004.

[26] V.A. Solntsev, *The electric field gain in the cathode with fractal multistep surface*, Technical Digest of IVMC, 1997.

[27] S. H. Jo, J. Y. Huang, S. Chen, G. Y. Xiong, D. Z. Wang, and Z. F. Ren, *Field emission of carbon nanotubes grown on carbon cloth*, J. Vac. Sci. Technol. B 23(6), 2005.

[28] A. F. Bobkov, E. V. Davidov, S. V. Zaitsev, A. V. Karpov, M. and A. Kozodaev, *Some aspects of the use of carbon materials in field electron emission cathodes*, J. Vac. Sci. Technol. B 19(1), 2001.

[29] P. R. Wilshaw and E. C. Boswell, *Field emission from pyramidal cathode covered in porous silicon*, J. Vac. Sci. Technol. B 12(2), Mar. 1994.

[30] N. I. Tatarenko, V. A. Solntsev and A. N. Rodionov, *Novel nanoscale field emission structures: Fabrication technology, experimental, and calculated characteristics*, J. Vac. Sci. Technol. B 17(2), Mar 1999.

[31] R. Kurt, J.M. Bonard, and A. Karimi, *Structure and field emission properties of decorated C/N nanotubes tuned by diameter variations*, Thin Solid Films 398–399, pp. 193–198, 2001.

[32] N. Miyamoto, H. Adachi, H. Nakane, and K. Yamane, *Emission stability of a field emitter array observed by an emission microscope*, J. Vac. Sci. Technol. B 21.1, 2002.

[33] R. Z. Bakhtizin, S. Ghots and P. V. Glazer, *Statistical model of semiconductor field emitter with atomically clean surface*, J. Micromech, pp. 45-48, 1993.

[34] M. Kildemo, S. Calatroni, and M. Taborelli, *Breakdown and field emission conditioning of Cu, Mo, and W*, Physical Review Special Topics – Accelerators and beams, Vol. 7, 2004.

[35] Compiled by G. W. C. Kaye and T. H. Laby, *Tables of Physical and Chemical Constants and Some Mathematical Functions (Kaye & Laby) 16th Ed.*, Longman Sc & Tech, 1995.

[36] V. Sonnenberg and J. A. Martino, *SOI technology characterization using SOI-MOS capacitor*, Solid-State Electronics, Vol. 49, pp. 109–116, 2005.

Chapter 4

Simulations

4.1. Overview of Device Optimisation

A model has been developed that incorporates field emission and initial electron positions, along with electron optics under electrostatic and electromagnetic fields. Emphasis on electron trajectory modelling is given between the interactions of crossed electric and magnetic fields within the magnetometer, with an analytic approach being employed to maximise sensitivity and range, with supporting numerical results.

Firstly, an analytical model has been developed to estimate the current density, sensitivity and range of devices under different device parameters of electrode distances, voltages and applied magnetic fields. The analytical model presented is considered accurate enough to be used as the basis of comparison with supporting evidence from the electron optic simulation programme, SimIon [1]. Discrepancies between the numerical and analytical models have been noted and are partly due to the differences in approximation of electric field calculation, partly due to the fact that fringing fields are considered in the numerical model though not within the analytic model, and partly due to the fact that no field emission simulation package exists. The final stage is one of device optimisation which aims to maximize current density and minimise emitted electron-beam (e-beam) width, both of which will be shown to play critical roles in the magnetometer's range and sensitivity.

4.2. Supporting Numerical Simulations

Like common electrostatic packages, SimIon [1] uses the finite element method to solve the Laplace equation to calculate the electric field, and then employs the (fourth order) Runge-Kutta method to trace electron paths within the device, the subject of which is well documented [1 pp. E-6 to E-14].

4.2.1. Laplace equation for crossed electric and magnetic fields

The model considered is the simplified two dimensional device introduced in chapter one and shown in figure 4.1, which has been employed for a number of reasons. The primary reason is that the area of primary interest is within the xy-plane, where electron trajectories within the z direction (into or out of the device) are associated with either very high magnetic fields or large voltages on the substrate. Either of these may result in unpredictable behaviour as indicated by empirical research in the previous chapter and by the author [2].

A number of assumptions have been introduced into this model, the first being; only relatively low magnetic fields are considered which confine radius of curvature of the e-beam to the xy-plane. Another assumption is that pseudo-field emission is used; where electrons are placed around the cathode in accordance with current densities found by Fowler Nordheim theory. This is necessary because SimIon cannot account for the doping level of the silicon of the electrodes - only absolute conductivity is assumed for electrodes. Also, SimIon is unable to account for material permittivities within the device so that silicon oxide layer is not modelled, only a vacuum gap is present to distinguish between the substrate and top-level as indicated in figure 4.4. Though this is thought not to alter the device operation as the silicon oxide layer is used a supporting structure within the device. Overall, the analytic model used has no substrate due to complexity of introducing a substrate, and the numerical model presented does account for the substrate. Because the substrate is used to optimise the device under quiescent magnetic fields, it has been found that there is little difference between the analytic and numerical models when a magnetic field is applied.

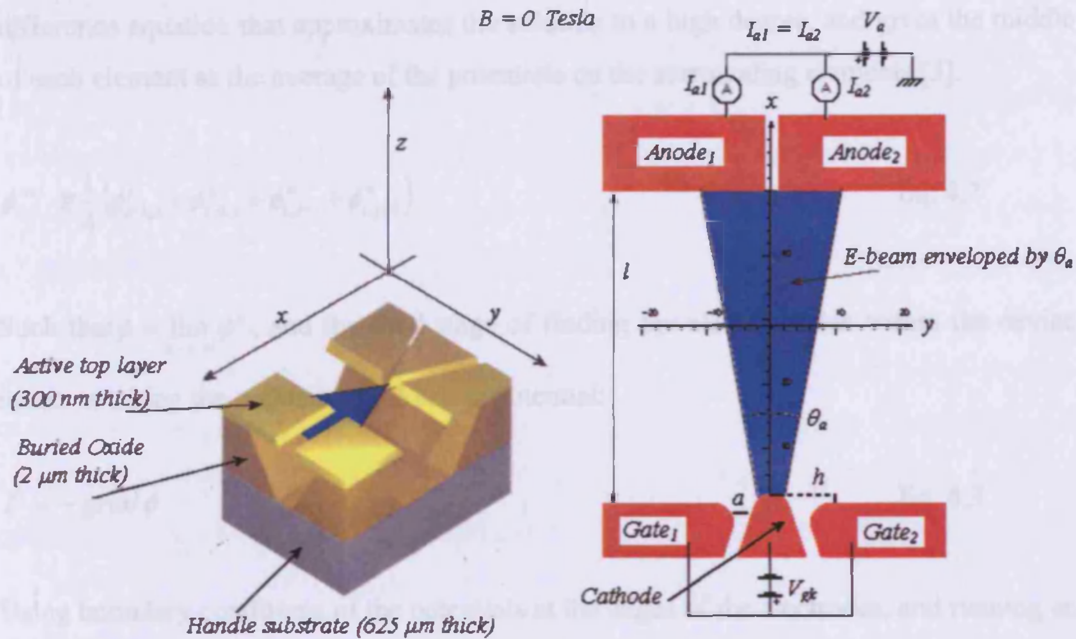

Figure 4.1. Showing a schematic of the device (left) and the two-dimensional top layer model (right). Under the quiescent magnetic fields (shown), the emitted e-beam is incident on both electrodes in equal measure.

The first stage of the simulation deals with finding the electric field for a given geometrical design, i.e. for the device structure shown above (right side). In order to find the potentials and electric fields within the device, the distribution of charge must be found from the boundaries of the regions defined by the sensor. This is accomplished by solving the Laplace equation (Eq. 4.1) that satisfies a set of boundary conditions given by the device geometry and electrode voltages.

$$\frac{d^2\phi}{dx^2} + \frac{d^2\phi}{dy^2} = 0 \qquad \text{Eq. 4.1}$$

The Laplace equation may be solved numerically by the discretization of the xy-plane of the sensor into a fine mesh, where it is possible to address the potential at the center of each element as indicated in figure 4.2(a). The solution to this specific problem, i.e. the problem defined by the geometry, is then found by the Jacobi scheme (Eq. 4.2) which is a

difference equation that approximates the solution to a high degree, and gives the middle of each element as the average of the potentials on the surrounding elements [3].

$$\phi_{i,j}^{n+1} \cong \frac{1}{4}\left(\phi_{i+1,j}^{n} + \phi_{i-1,j}^{n} + \phi_{i,j+1}^{n} + \phi_{i,j+1}^{n}\right) \quad \text{Eq. 4.2}$$

Such that $\phi = \lim_{n \to \infty} \phi^{n}$, and the final stage of finding the electric fields within the device involves taking the gradient of the scalar potential:

$$F = -\,grad\,\phi \quad \text{Eq. 4.3}$$

Using boundary conditions of the potentials at the edges of the electrodes, and running an iterative process (represented by n) for each element until the solution converges, results in the desired solution as shown in figure 4.2(b):

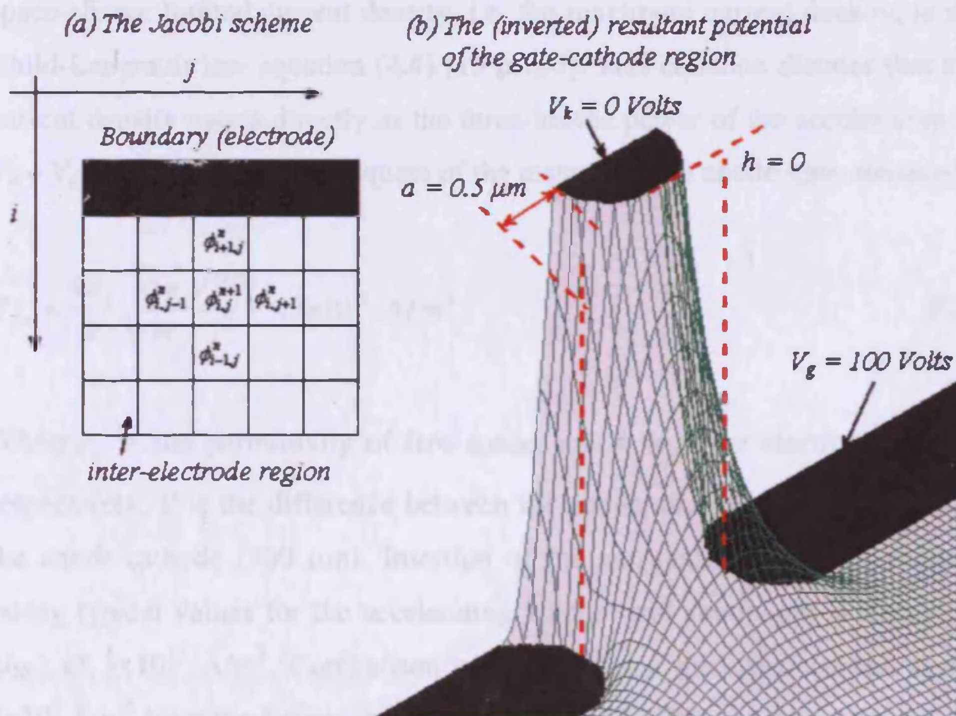

Figure 4.2. Showing (a) The Jacobi scheme involving the discretization of the xy-plane, and (b) the (inverted for clarity) potential of the gate-cathode region developed in SimIon.

Because the applied magnetic field covers the entire magnetometer, i.e. is perpendicular to the device, and is constant, there is no need for a similar scheme for application of the magnetic field. Instead only the value of the field, B_z, is applied to the device in analytic and simulated calculations. Magnetic fields in the other directions are assumed zero for calculations and are kept constantly at zero for empirical measurements, i.e. only $(0, 0, B_z)$ is applied by the triaxial Helmholtz coil system introduced in the previous chapter to an xy-plane containing electric fields of $(F_x, F_y, 0)$.

Assumptions introduced in the model include one-way coupling, where once an electron tunnels from the cathode no change in barrier voltage is produced by escaping electrons, and within in this context, when electrons leave the cathode surface they are directly replaced by an electron from the cathode lattice [4]. In addition, space-charge is an inherent property of all vacuum system to some degree. Because of the low current densities inherent with devices presented here, emitted electrons are affected by the underlying electric field though they do not, in turn, affect it, i.e. there is no feedback effect on the Laplace equation, and hence space-charge is not considered an issue. The space-charge limited current density, i.e. the maximum current density, is shown by the Child-Langmuir law equation (4.4) [15 p.100]. This equation dictates that the maximum current density varies directly as the three-halves power of the accelerating voltage, $V = V_a - V_g$, and inversely as the square of the distance l (the anode-gate distance).

$$J_{\lim} = \frac{4\varepsilon_o}{9}\sqrt{\frac{2e}{m}}\frac{V^{(3/2)}}{l^2} \approx 3\text{x}10^{13}\ A/m^2 \qquad \text{Eq. 4.4}$$

Where ε_o is the permittivity of free space, e and m is the electron's charge and mass respectively, V is the difference between the anode and gate (250 – 100 Volts), and l is the anode-cathode (500 μm). Insertion of the constants (defined in chapter two), and taking typical values for the accelerating voltage and anode-gate distance, gives a limit (J_{lim}) of $3\text{x}10^{13}$ A/m^2. Comparison of this with the measured current density limit of $4\text{x}10^7$ A/m^2 from the figures given in chapter two (p. 38), show that the measured density is well below the limit allowed by the Child-Langmuir law.

4.2.2. Electron distribution and ray tracing

Having obtained the electric field distribution across the device, the second stage involved in the numerical simulation is that of initial electron position and then calculating the electron trajectories within the device. Because SimIon is unable to simulate field emission, electrons are placed around the cathode tip in accordance with the angular current density. This is determined by measuring the electric field across the tip within SimIon for a specific geometry and electrode voltages as indicated above in figure 4.2, then placing the angular electric field, i.e. $F(\theta)$ measured across the cathode apex, into equation (2.2) resulting in the corresponding angular current density (the constants are defined in chapter two):

$$J(\theta)=\frac{aF(\theta)^2}{\phi}\exp\left(\frac{-b\phi^{\frac{3}{2}}}{F(\theta)}\right) \qquad \text{(Eq. 2.2)}$$

An example of angular electric field and corresponding angular current density is shown in figure 4.3 for an arbitrary set of device variables, i.e. interelectrode distances, l = 50 µm, a = 0.5 µm and h = 0, with electrode voltages of V_{gk} = 100 V and V_a = 200. Electron position is then found by placing electrons up to the anode angle, θ_a, or angular spread given by:

$$\theta_a = 2\left(\frac{\int_0^{\pi/2}\theta^2 J(\theta)\,d\theta}{\int_0^{\pi/2}J(\theta)\;\;d\theta}\right)^{-\frac{1}{2}} \qquad \text{Eq. 4.5}$$

Where the distribution width at the anode, i.e. the electron beam enveloped by the angular spread (figure 4.1, right-side), is given as equation 4.6:

$$y_w = \tan(\theta_a)\,l \qquad \text{Eq. 4.6}$$

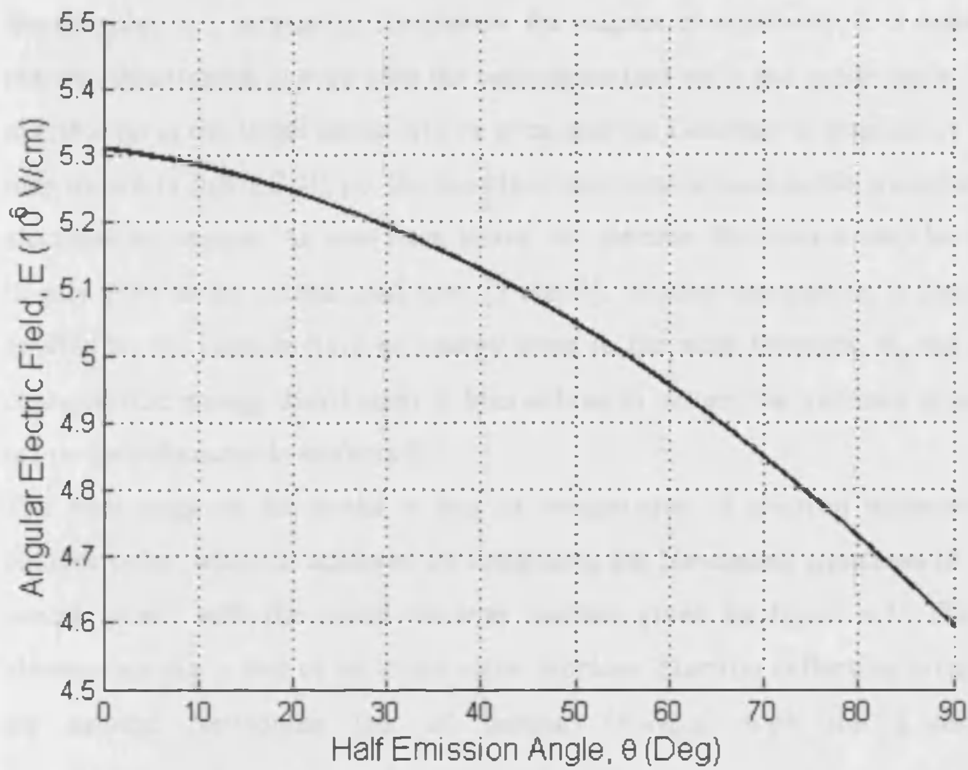

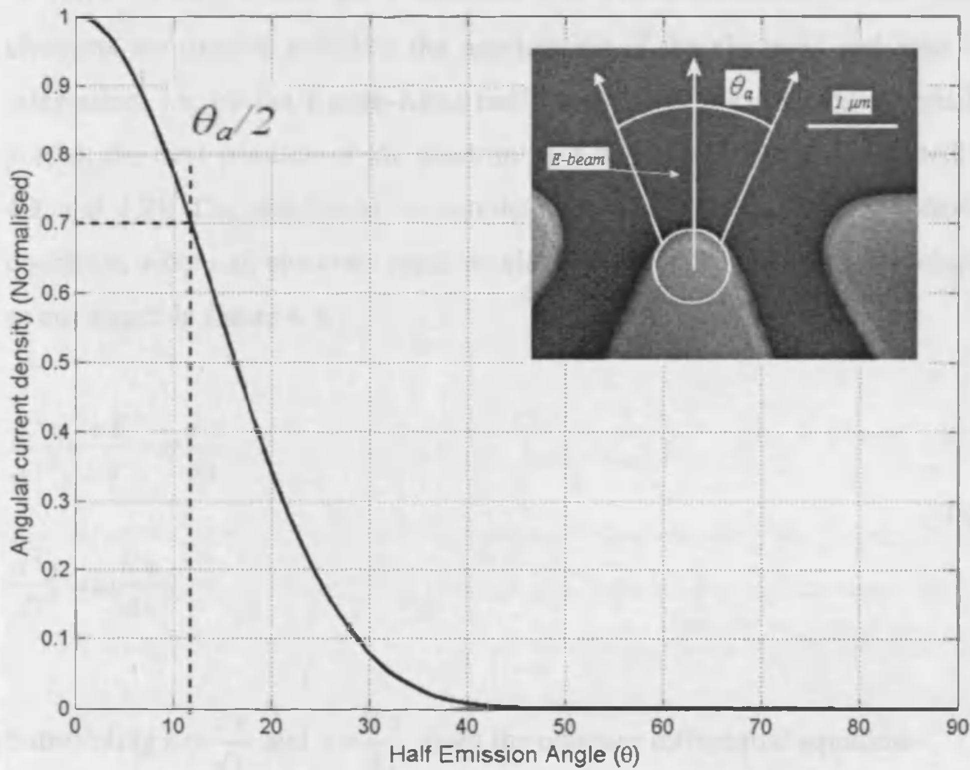

Figure 4.3. Angular electric field (top) and corresponding angular current density (bottom).

Because this is a supporting simulation, for reasons of simplicity, it is assumed that the electron distribution is even over the cathode surface up to the anode angle. The electron distribution at the target anode will be even and not Gaussian as implied by the emission map shown in figure 2.10, i.e. the density of electrons around anode areas being struck by electrons is constant. As seen from above, the electron distribution may be thought of as largely even in the central peak area [5 and 6]. Another assumption is that all electrons emitted by the cathode have an energy equal to the work function, Φ, and although the characteristic energy distribution is Maxwellian in nature, the variance of energy spread is low for cold cathode emitters [6].

The final stage in the model is that of computation of electron trajectories from the cathode point, which is achieved by integrating the Newtonian equations of motion. This process starts with the initial electron position given by figure 4.3: The problem in electron tracing is that of an initial value problem. Electron deflection involves equating the second Newtonian law of motion $(F = ma)$ with the Lorentz equation $(F = e(E + v \times B)$ which gives equation 4.6. The electrostatic forces imposed on the electrons are used to calculate the acceleration of the electrons and used by numerical integration, i.e. by the Runge-Kutta method which is documented in detail [7 - 10], to predict the next position of the electron by a time-step method (described by equations 4.8 and 4.9). The simulation is complete when all electrons reach a device boundary condition, where all electrons reach an electrode or go beyond the inter-electrode regions as envisaged in figure 4.4.

$$\frac{d^2x}{dt^2} = \frac{eE}{m} - \omega\frac{dy}{dt}$$

$$\frac{d^2y}{dt^2} = \omega\frac{dx}{dt}$$

Eq. 4.7

Substituting $w = \frac{dx}{dt}$ and $z = \frac{dy}{dt}$ gives the ordinary differential equations:

$$\frac{dw}{dt}=\frac{eE}{m}-\omega z=F(t,w,z)$$ Eq. 4.8

$$\frac{dz}{dt}=\omega\, w=G(t,w,z)$$

Which are suitable for the fourth-order Runge Kutta scheme:

$$w_{n+1}=w_n+\frac{h}{6}(k_1+2k_2+2k_3+k_4)$$

Eq. 4.9

$$z_{n+1}=z_n+\frac{h}{6}(I_1+2I_2+2I_3+I_4)$$

Where:

$$k_1=hF(t_n,w_n,z_n)$$
$$k_2=hF(t_n+h/2,\ w_n+k_1/2,\ z_n+I_1/2)$$
$$k_3=hF(t_n+h/2,\ w_n+k_2/2,\ z_n+I_2/2)$$
$$k_4=hF(t_n+h,\ w_n+k_3,\ z_n+I_3)$$

$$I_1=hG(t_n,w_n,z_n)$$
$$I_2=hG(t_n+h/2,\ w_n+k_1/2,\ z_n+I_1/2)$$
$$I_3=hG(t_n+h/2,\ w_n+k_2/2,\ z_n+I_2/2)$$
$$I_4=hG(t_n+h,\ w_n+k_3,\ z_n+I_3)$$

$$t_{n+1}=t_n+h$$

The value, w_{n+1}, is determined by the present value (w_n) plus the product of the size of the interval step (a suitable h, which SimIon auto selects) and an estimated slope given by k_n or I_n. The initial conditions are given by w_0 and z_0, so the first application of the scheme gives w_1 and z_1, and so on iteratively until the electrons reach a boundary condition.

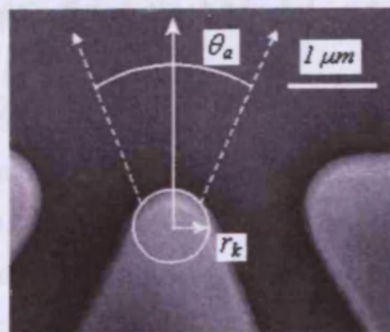

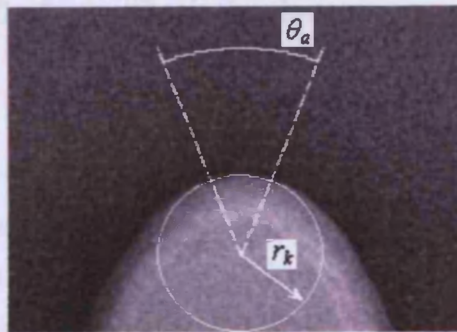

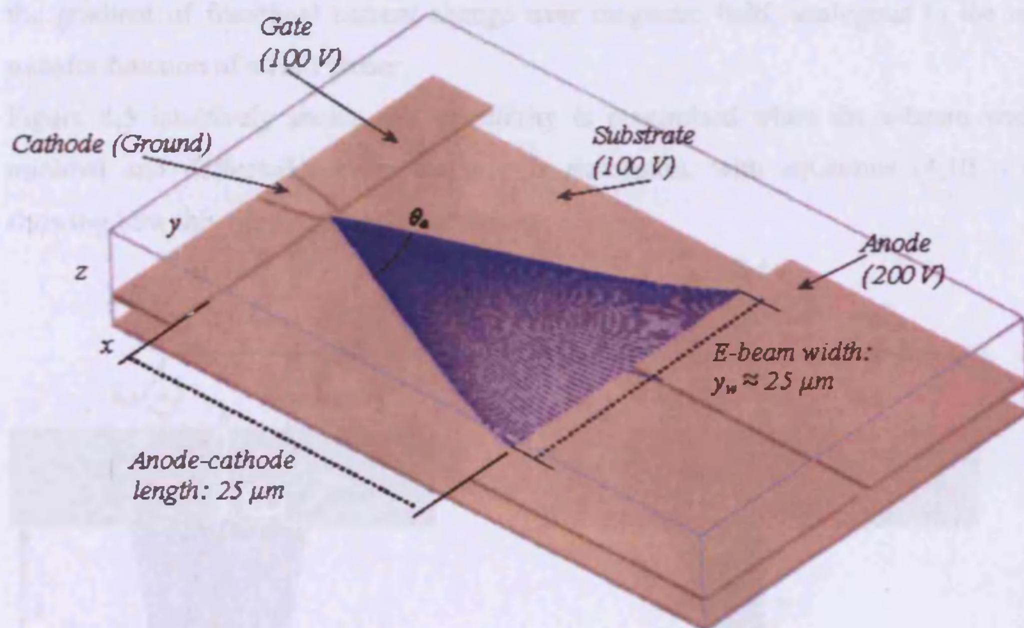

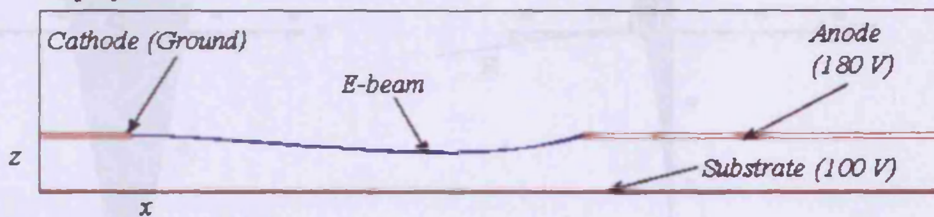

Figure 4.4. Showing the proposed electron distribution (top), and the electron trajectories (blue lines) derived by the Runge-Kutta scheme (middle and bottom).

4.3. Analytical Model and Preliminary Optimisation

Sensitivity is predominantly defined by two factors, the e-beam width under quiescent magnetic fields (y_w) and the y-distance of the deflected e-beam under a magnetic field (Δy), with factors such as the device geometry and applied magnetic field further defining these. Specifically, sensitivity is defined as the fractional change in the measured anode currents (directly related to y_w and Δy) over the applied magnetic field, i.e. sensitivity is the gradient of fractional current change over magnetic field, analogous to the output transfer function of a Hall sensor.

Figure 4.5 intuitively shows that sensitivity is maximised when the e-beam width is minimal and deflected e-beam distance is maximum, with equations (4.10 – 4.12) showing how this figure relates to sensitivity:

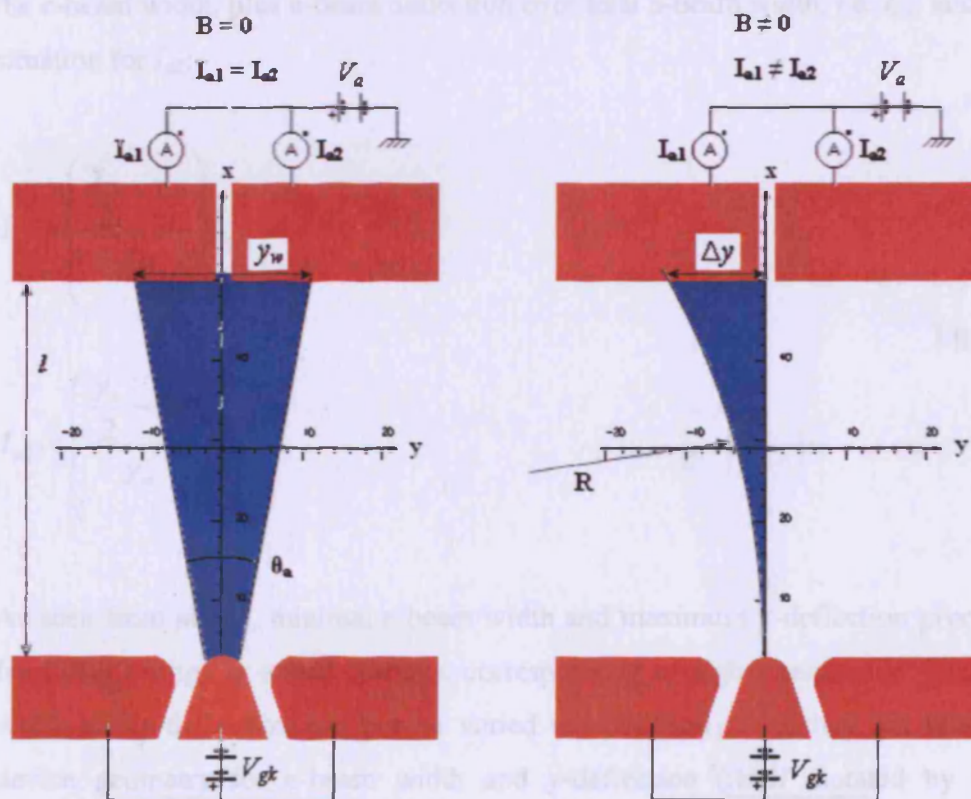

Figure 4.5. Factors influencing the sensitivity of the device, with e-beam width (y_w) under quiescent magnetic conditions (left) and e-beam deflection (Δy) under a magnetic field of B_Z applied within the xy-plane (right).

$$S = \frac{\frac{(I_{a1} - I_{a2})}{(I_{a1} + I_{a2})}}{B_Z} = \frac{d(\Delta Ia/Ia)}{dB} \quad \%/T \qquad \text{Eq. 4.10}$$

With total (anode) current as the sum of individual anode currents, and the change in anode current as the difference between the two:

$$I_a = I_{a1} + I_{a2}$$

$$\Delta I_a = I_{a1} - I_{a2} \qquad \text{Eq. 4.11}$$

By inspection of figure 4.5 individual anode currents are defined as the fraction of half the e-beam width, plus e-beam deflection over total e-beam width, i.e. I_{a1}, and the reverse situation for I_{a2}:

$$I_{a1} = \left(\frac{\frac{y_w}{2} + \Delta y}{y_w} \right) I_a$$

$$I_{a2} = \left(\frac{\frac{y_w}{2} - \Delta y}{y_w} \right) I_a \qquad \text{Eq. 4.12}$$

As seen from above, minimal e-beam width and maximum y-deflection give the highest fractional change in anode currents, corresponding to higher sensitivity. Clearly e-beam width and y-deflection can not be varied independently, but they are related through device geometry for e-beam width and y-deflection (itself dictated by the applied magnetic field). It is these two factors: Electron beam width *(y_w)* and, deflected e-beam distance *(Δy)* that are described in detail in the next section.

4.3.1. Electron beam width under quiescent magnetic fields

The method of calculating the e-beam width requires three steps: (1) Calculation of the angular electric field across the cathode surface, $F(\theta)$. (2) Angular current density, $J(\theta)$. (3) Angular beam spread, θ_a as shown in figure 4.5 (left-side).

The analytical model used is shown in figure 4.6 where the model developed by Jensen [11 p. 1944, 12 and 13] is employed to calculate the angular electric field across the cathode surface. This uses a ring of charge acting as the gate, centered on a central cathode sphere, both of which are in parallel to the anode plane. Although Jensen's Saturn model gives approximate quantitative estimates of the angular beam spread as it is more suited to a three dimensional model, qualitative dependencies may still be inferred.

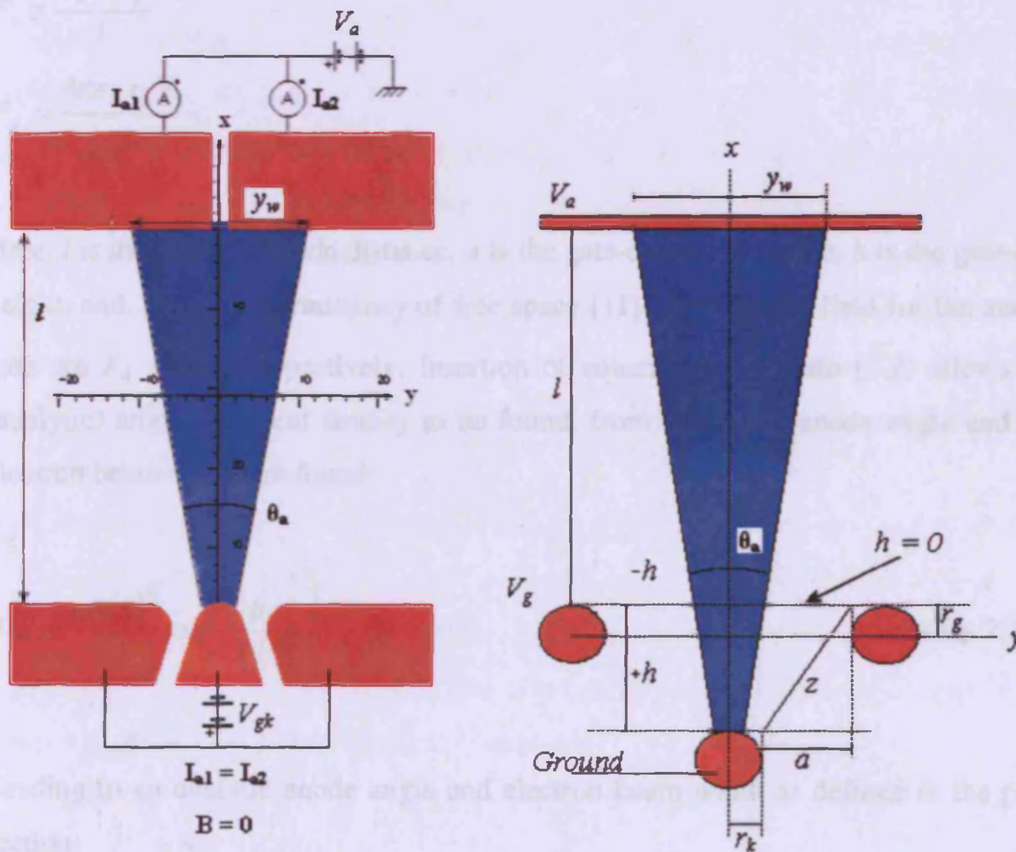

Figure 4.6. The schematic representation of the model (left) and the analytical model developed by Jensen (right).

As with all electrostatic problems of this type, Jensen's model is a boundary value problem with azimuthal (x-axis) symmetry, the solution of which is found by the image of charges method leading to a summation of Legendre polynomials [11 and 7]. Equating Jensen's analytic solution to the variables given above and expanding to the second order Legendre polynomial gives the angular electric field across the cathode as equation (4.12):

$$F(\theta)= 3F_a \cos\theta + F_g \left\{1+3\frac{r_k h}{z^2}\cos\theta+\frac{5}{4}\left(\frac{r_k}{z}\right)^2\left(3\left(\frac{h}{z}\right)^2-1\right)\left(3(\cos\theta)^2-1\right)\right\} \quad \text{Eq. 4.13}$$

Where:

$z^2 = a^2 + h^2$

$F_a \cong \frac{V_a - V_g}{l}$

$F_g = \frac{4\pi\varepsilon_o r_g V_g}{z r_k}$

Here, l is the anode-cathode distance, a is the gate-cathode aperture, h is the gate-cathode height, and ε_o is the permittivity of free space [11]. The electric field for the anode and gate are F_a and F_g respectively. Insertion of equation (4.12) into (2.2) allows for the (analytic) angular current density to be found, from which the anode angle and desired electron beam width are found:

$$J(\theta)=\frac{aF(\theta)^2}{\phi}\exp\left(\frac{-b\phi^{\frac{3}{2}}}{F(\theta)}\right) \quad \text{(Eq. 2.2)}$$

Leading to an analytic anode angle and electron beam width as defined in the previous section:

$$\theta_a = 2\left(\frac{\int_0^{\pi/2} \theta^2 \, J(\theta)\, d\theta}{\int_0^{\pi/2} J(\theta) \quad d\theta}\right)^{-\frac{1}{2}} \qquad \text{(Eq. 4.5)}$$

$$y_w = \tan(\theta_a)\, l \qquad \text{(Eq. 4.6)}$$

From the above definition of the critical emission angle, clearly a smaller anode angle equates to a smaller electron beam width at the anode. Because the nature of the cathode current density and e-beam width are non-linear with respect to the three geometric variables of the device, i.e. $J = f(a, h, l)$ and $y_w = f(a, h, l)$, a first order optimization process is required and illustrated in figure 4.7. This aims to minimise the e-beam width by altering the gate-cathode aperture and height variables for fixed constraints. Design constraints introduced at this stage include: A minimum aperture value of half a micron up to one micron; considered the safest minimum values that the device processing stage can achieve without bridging between the gate and cathode electrodes [14] which would still ensure emission, and the gate-cathode geometry smaller relative to the anode-cathode length; to further ensure field emission from the cathode and not other electrodes. Other constraints are a gate voltage of one hundred volts to ensure emission, and an anode voltage equal to twice the gate voltage, i.e. V_g = 100 Volts and $V_a = 2V_g$, to ensure all electrons are drawn to the anode.

As seen from figure 4.7, total e-beam width is largely unaffected over the given aperture and height ranges, i.e. within 0.5 μm < a < 1 μm, and, -2 μm < h < 2 μm, though the total e-beam width may be considered minimised for minimal aperture with the cathode placed 1 μm below the gate. It is thought that this configuration ensures field emission while minimising the electron beam width at the anode.

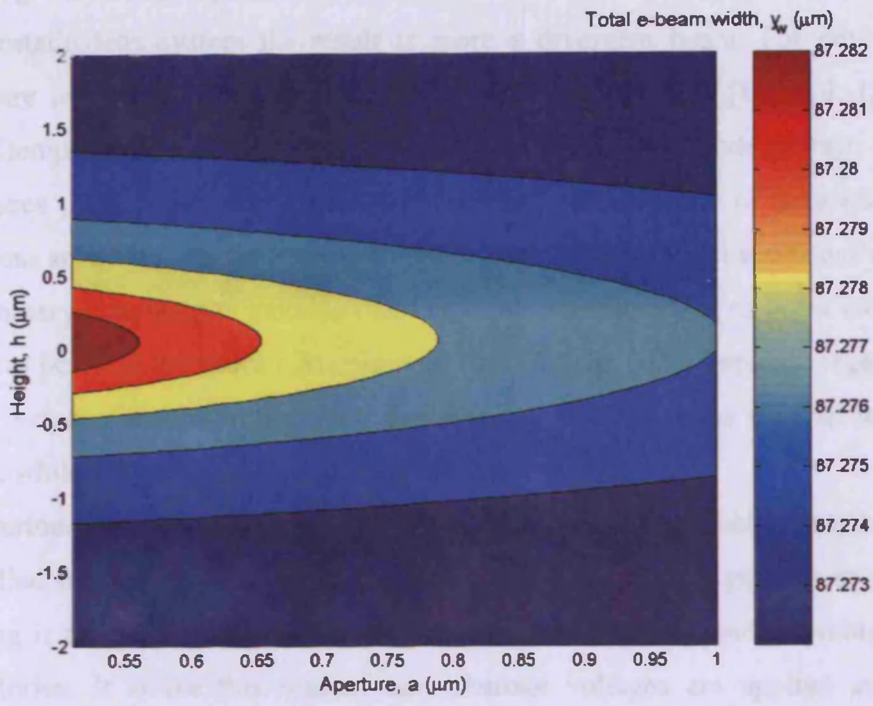

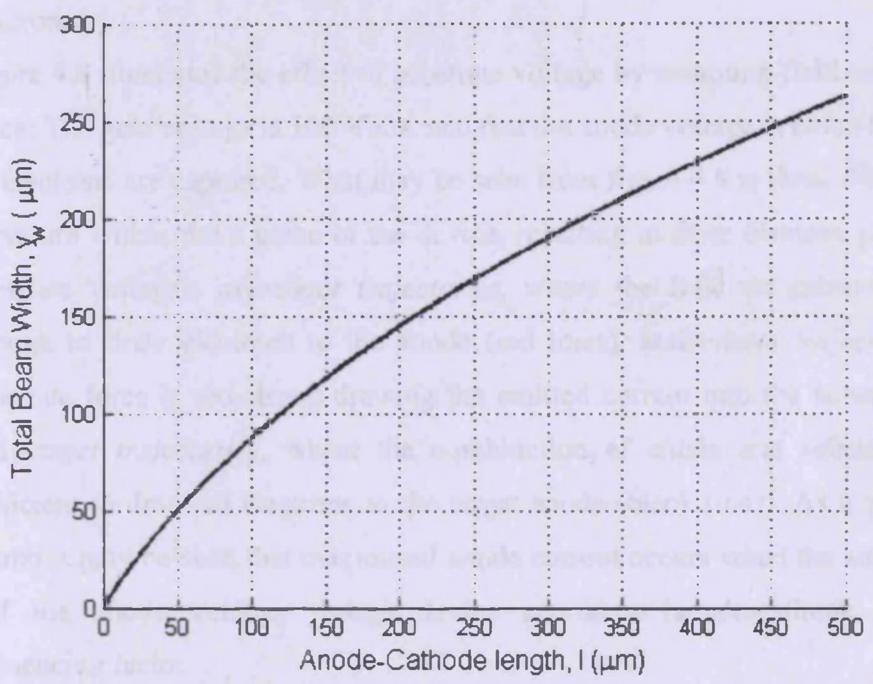

Figure 4.7. Total electron beam width for fixed constraints as a function of gate aperture and height (above), and total electron beam width as a function of anode-cathode length (below).

Although a sharp, collimated e-beam is desired, the reality is that without any electrostatic lens system the result is more a divergent beam. For devices of similar structure without the aide of lenses, researchers such as Roth [15, Vol. 1, pp. 176-184] and Klemperer [3 p. 275] have shown that increasing the anode voltage proportionally decreases the e-beam width, though the overall affect is one of reduced sensitivity as electrons spend far less time in the detection region between the anode and cathode.

Preliminary conclusions indicate that the anode voltage needs to be as close to the gate value as possible to ensure maximised electron expose under applied magnetic fields, i.e. lower velocity results in a greater degree of curvature for the e-beam under magnetic fields, while still drawing all electrons to the anode.

One serious criticism of the analytic model presented is that electron trajectories are only modelled in two dimensions. It was empirically found that ignoring the substrate, i.e. leaving it floating during experiments, resulted in charging and unpredictable electron trajectories. It is for this reason that substrate voltages are applied under quiescent magnetic fields such that the anode current is maximised to capture all of the emitted electrons.

Figure 4.8 illustrates the effect of substrate voltage by assuming field emission has taken place: The gate voltage is 100 Volts, and that the anode voltage is twice the gate to ensure all electrons are captured. What may be seen from figure 4.8 is three different degrees of curvature within the z plane of the device, resulting in three electron paths for different substrate voltages: *overshoot trajectories*, where the field on substrate is not strong enough to draw electrons to the anode (red lines), *undershoot trajectories*, where the substrate force is too strong drawing the emitted current into the substrate (blue lines), and *target trajectories*, where the combination of anode and substrate voltages are sufficient to draw all electrons to the target anode (black lines). As a first order rule of thumb it may be seen that maximised anode current occurs when the substrate voltage is half the anode voltage, though device geometry (anode-cathode spacings) is an influencing factor.

These simulations imply that all electrodes for any device require voltage tuning in order to maximise anode current. This is investigated in the next chapter, where empirical results show the result of anode current as a function of electrode voltages for different anode-cathode spacings. The following simulations assume that the anode current has been maximised.

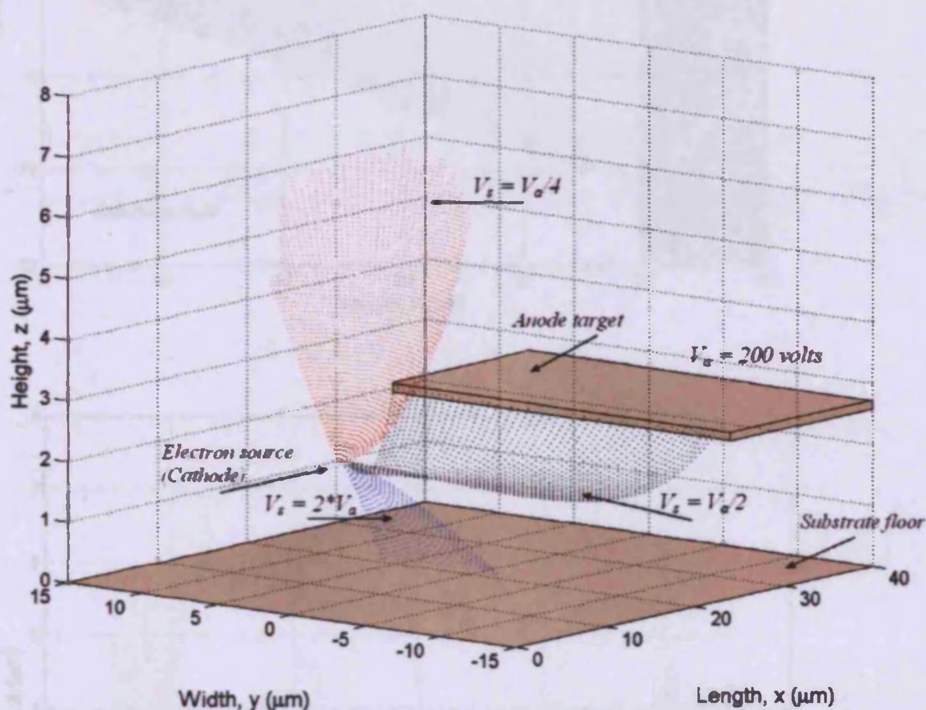

Figure 4.8(a). Showing a three dimensional view of electron beam trajectories for different substrate voltages, indicating that the emitted e-beam may be controlled within the z-dimension.

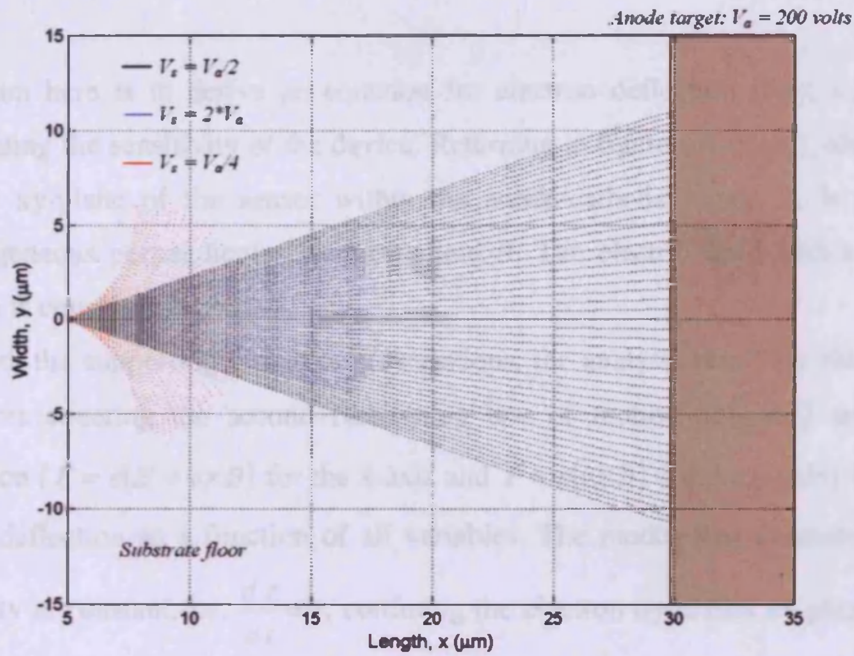

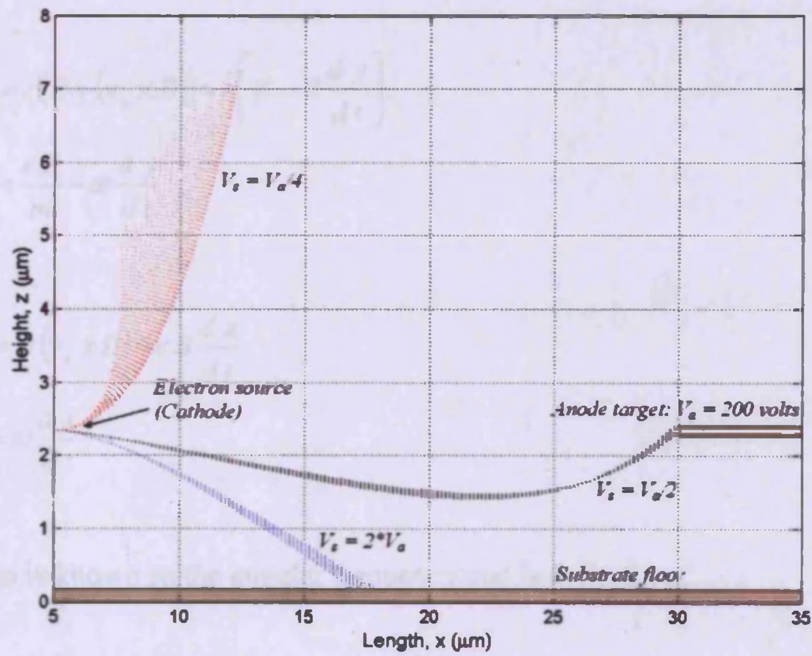

Figure 4.8(b and c). Showing top and side profiles of the above result. Clearly showing overshoot (red lines), undershoot (blue lines), and target (black lines) trajectories.

4.3.2. Analytical calculation of the Lorentz Force Equation

The aim here is to derive an equation for electron deflection (Δy), a prerequisite for estimating the sensitivity of the device. Returning to figure 4.5 (right), electron trajectory in the xy-plane of the sensor within the anode-cathode region E, is shown under a homogeneous perpendicular magnetic field B. The electric field within the anode-gate region is considered constant.

As with the supporting numerical calculations, the analytic result for electron deflection involves equating the second Newtonian law of motion $(F = ma)$ with the Lorentz equation ($F = e(E + v \times B)$ for the x-axis and $F = e(v \times B)$ for the y-axis), then solving for the y-deflection as a function of all variables. The model also assumes that the z-axis velocity is constant, i.e. $\frac{dz}{dt} = 0$, confining the electron dynamics xy-plane. Equating the Newtonian law of motion with the Lorentz force gives:

$$m\frac{d^2x}{dt^2} = e(E + (v_y \times B)) = e\left(E - B\frac{dy}{dt}\right)$$
$$\frac{d^2x}{dt^2} = \frac{eE}{m} - \omega\frac{dy}{dt} \qquad \text{Eq. 4.14}$$

$$m\frac{d^2y}{dt^2} = e(v_x xB) = eB\frac{dx}{dt}$$
$$\frac{d^2y}{dt^2} = \omega\frac{dx}{dt} \qquad \text{Eq. 4.15}$$

Where ω is known as the angular frequency and is defined as:

$$\omega = \frac{eB}{m}$$

Equation (4.14) may be integrated directly assuming the initial velocity of each electron for both components is zero at time zero, i.e. $\left.\frac{dx}{dt}\right|_{t=0} = \left.\frac{dy}{dt}\right|_{t=0} = 0$, and that the electron starts at (0,0,0), i.e. the cathode tip:

$$\frac{dy}{dt} = \omega x \qquad \text{Eq. 4.16}$$

Placing equation (4.16) into (4.15):

$$\frac{d^2x}{dt^2} = \frac{eE}{m} - \omega^2 x$$

$$\frac{eE}{m} = \frac{d^2x}{dt^2} + \omega^2 x \qquad \text{Eq. 4.17}$$

Which is the equation of a simple harmonic oscillator subject to a constant force, the general solution of which is given as [15, Vol. 1 p. 181]:

$$x(t) = \frac{eE}{m\omega^2} + A\cos(\omega t) + B\sin(\omega t) \qquad \text{Eq. 4.18}$$

The specific solution for the harmonic oscillator presented here is found applying the initial conditions to the above, i.e. $\left.\frac{dx}{dt}\right|_{t=0} = \left.\frac{dy}{dt}\right|_{t=0} = 0$ making $x|_{t=0} = y|_{t=0} = 0$:

$$0 = \left.\frac{eE}{m\omega^2} + A\cos(0) + B\sin(0)\right|_{t=0}$$

$$\Rightarrow A = \frac{-eE}{m\omega^2}$$

$$\Rightarrow B = 0$$

Insertion of these constants (A and B) into equation (4.14) gives the specific solution:

$$x(t) = \frac{eE}{m\omega^2}(1-\cos(\omega t)) \qquad \text{Eq. 4.19}$$

Placing (4.19) into (4.16) and integrating with respect to time:

$$\frac{dy}{dt} = \omega x = \omega\left(\frac{eE}{m\omega^2}(1-\cos(\omega t))\right)$$
$$y(t) = \frac{eE}{m\omega^2}(\omega t - \sin(\omega t)) \qquad \text{Eq. 4.20}$$

Equations (4.19) and (2.40) are in parametric form and require a time-step to plot the trajectories as discussed in the numerical chapter. Further simplification of the above is achieved by decoupling the equations, i.e. eliminating t, to give $y(x)$. Further simplification may be found by substituting in the anode-cathode length (l) for x to give the total deflection as a function of anode-gate electric field (E), anode-cathode (l), and applied magnetic field (B) as shown in equation (2.20). Figure 4.9 shows total e-beam deflection for a series of magnetic fields, with confirmation of deflection in figure 4.9(bottom) showing numerical values from SimIon which appear to confirm similar deflection value by analytic means for 300 mT.

$$\Delta y = -\frac{m\pi}{BeE} + \frac{\sqrt{2}B\sqrt{eE^3 m}\, l^{\frac{3}{2}}}{3E^2 m} \qquad \text{Eq. 4.21}$$

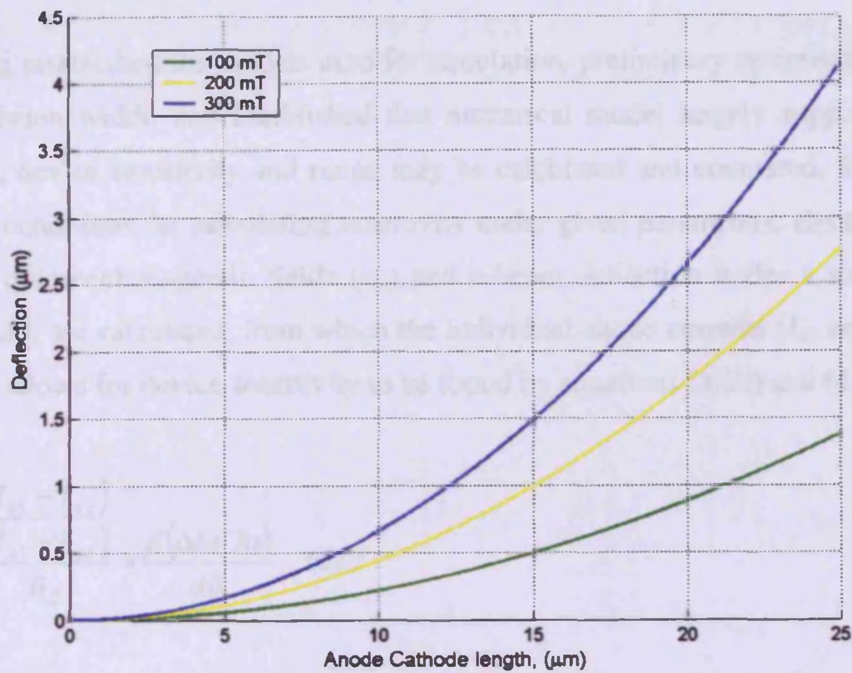

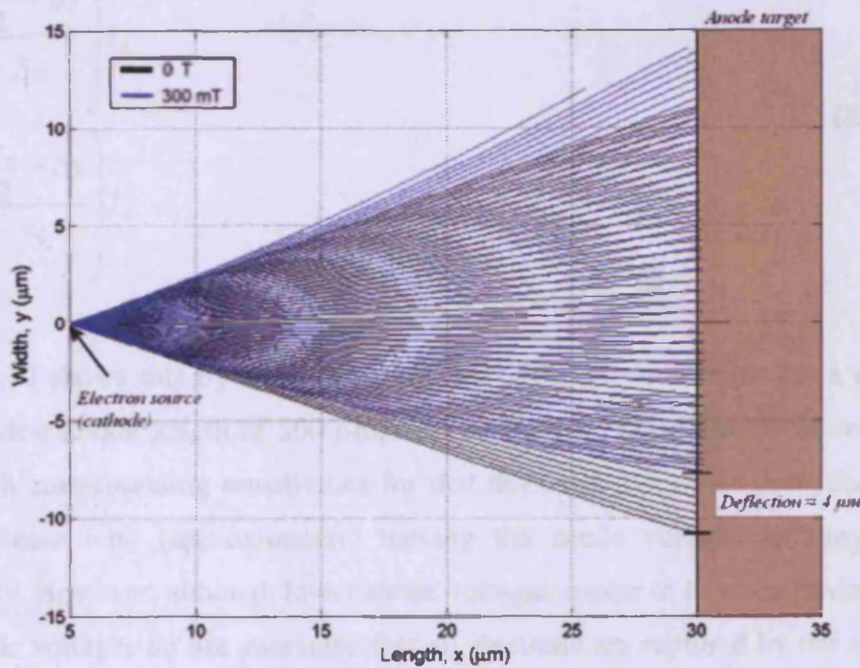

Figure 4.9. Showing total deflection for different magnetic fields from the analytic model (top), and one numerical result confirming deflection magnitude for 300 mT (bottom). Both sets of data derived from identical constraints, i.e. $l = 25\ \mu m$, $Vg = 100$ *volts* and $Va = 200$ *Volts*.

4.4. Sensitivity and Range

Having established the models used for simulation, preliminary optimisation to minimise the e-beam width, and established that numerical model largely supports the analytic model, device sensitivity and range may be calculated and compared. Starting with the initial conditions for calculating sensitivity under given parameters; electron beam width under quiescent magnetic fields (y_w) and e-beam deflection under a specific magnetic field (Δy) are calculated, from which the individual anode currents (I_{a1} and I_{a2}) are found which allows for device sensitivity to be found by equations (4.10) and (4.12):

$$S = \frac{\dfrac{(I_{a1} - I_{a2})}{(I_{a1} + I_{a2})}}{B_Z} = \frac{d(\Delta Ia/Ia)}{dB} \quad \%/T \qquad \text{(Eq. 4.10)}$$

$$I_{a1} = \left(\frac{\dfrac{y_w}{2} + \Delta y}{y_w} \right) I_a$$

$$I_{a2} = \left(\frac{\dfrac{y_w}{2} - \Delta y}{y_w} \right) I_a \qquad \text{(Eq. 4.12)}$$

Figure 4.10 shows this by calculating the individual anode currents for a single device with anode-cathode length of 500 μm, i.e. $l = 500\ \mu m$, for a number of anode voltages (top) with corresponding sensitivities for that device (bottom). As seen, the response is largely linear with (approximately) halving the anode voltage doubling the device sensitivity. However, although lower anode voltages appear to increase device sensitivity, low anode voltages do not guarantee that all electrons are captured by the anode. Figure 4.11(top) further supports this result by showing device sensitivity over anode-cathode length for a number of anode voltages. For low anode voltages there appears to be a doubling in sensitivity.

Figure 4.11(bottom) also shows the upper detectable range for the devices, which indicate an inverse relationship with sensitivity over anode-cathode distance, although for devices less than 250 μm in length the detectable range is well above what can be produced in the laboratory.

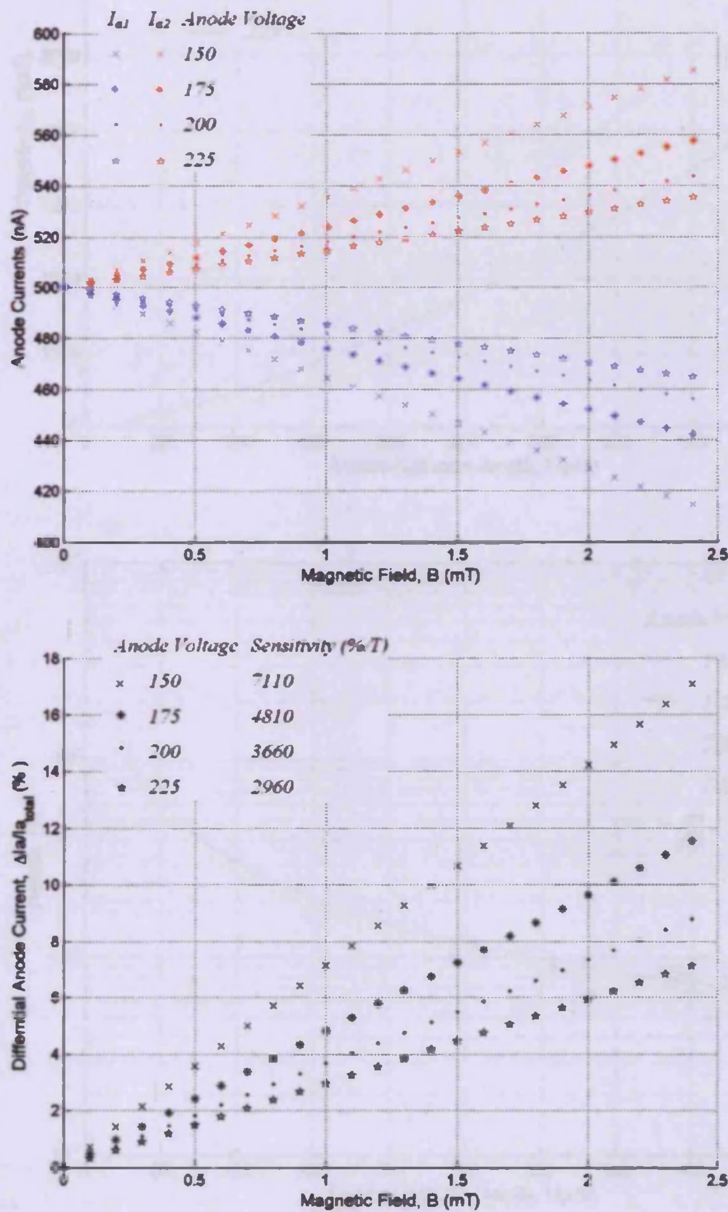

Figure 4.10. Anode current over magnetic fields for typical anode voltages (top), and the corresponding differential anode current which gives sensitivity (bottom) for a device with anode-cathode length of 500 μm.

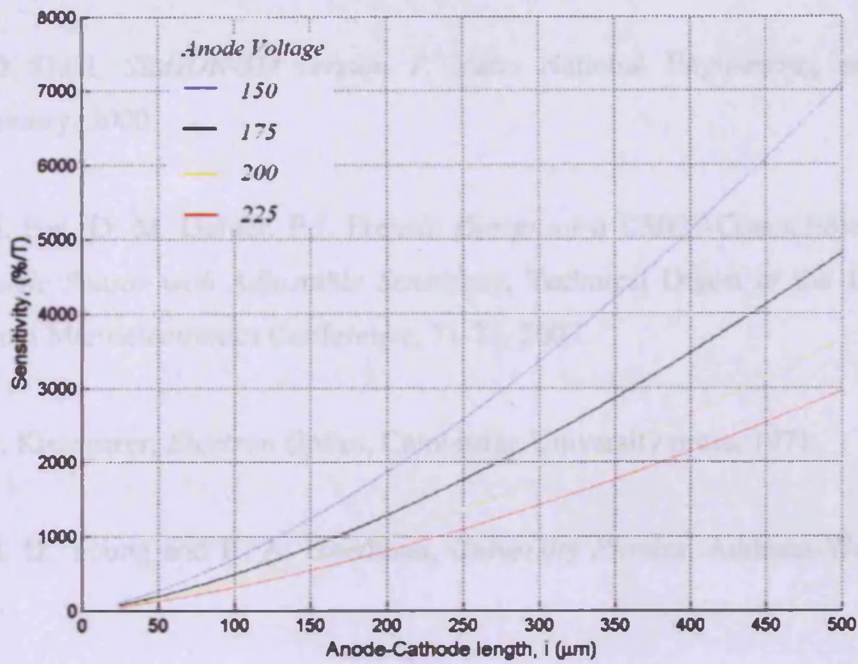

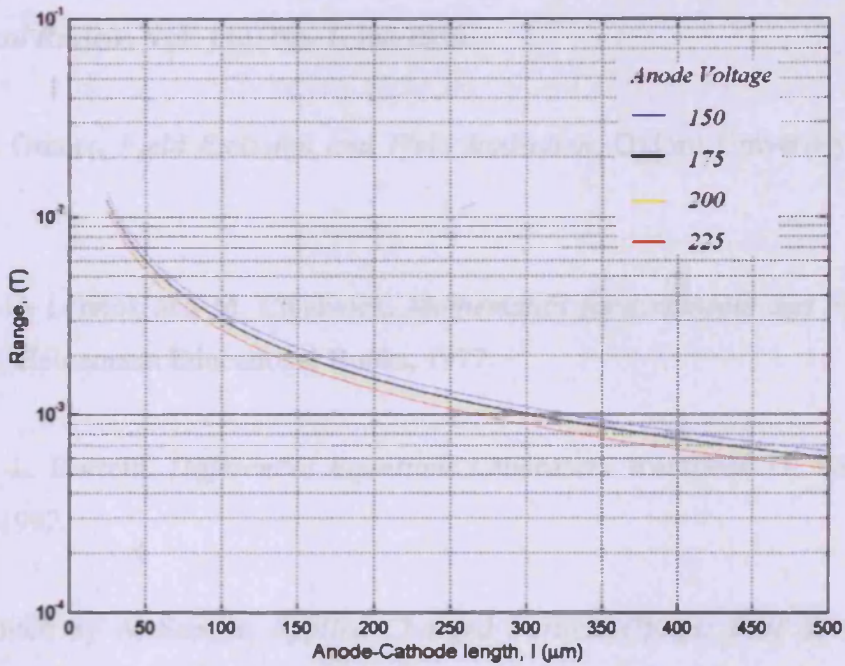

Figure 4.11. Illustrating the inverse relationship between sensitivity (top) and range (bottom) for a number of anode voltages.

4.5. References

[1] D. Dahl, *SIMION-3D version 7*, Idaho National Engineering and Environment Laboratory, 2000.

[2] G. Hui, D. M. Garner, P.J. French, *Design of a CMOS-Compatible Field-Emission Magnetic Sensor with Adjustable Sensitivity*, Technical Digest of the 16th International Vacuum Microelectronics Conference, 71-72, 2003.

[3] O. Klemperer, *Electron Optics*, Cambridge University press, 1971.

[4] H. D. Young and R. A. Freedman, *University Physics*, Addison-Wesley publishers, 2000.

[5] R. D. Young, *Theoretical Total-Energy Distribution of Field-Emitted Electrons, Physical Review*, Vol. 113, No. 1, Jan 1958.

[6] R. Gomer, *Field Emission and Field Ionization*, Oxford University Press, London, 1961.

[7] S. C. Lennox and M. Chadwick, *Mathematics for Engineers and Applied Scientists 2nd Ed*, Heinemann Educational Books, 1977.

[8] R. L. Borrelli, *Differential Equations Laboratory Workbook 1st Ed*, John Wiley & Sons, 1992.

[9] Edited by A. Septier, *Applied Charged Particle Optics: Part A*, Academic Press, 1980.

[10] Edited by A. Septier, *Applied Charged Particle Optics: Part B*, Academic Press, 1980.

[11] K. L. Jensen, *Analytical and seminumerical models for gated field emitter arrays (I. Theory)*, J. Vac. Sci. Technol. B 14(3), 1996.

[12] K. L. Jensen, *An Introduction to Electron Emission Physics and Applications, lecture notes: Beam Physics Course*, Inst. Res. El. & Appl. Phys, University of Maryland, 2005

[13] Private correspondence with K. L. Jensen, University of Maryland, 2007.

[14] Private communication with Dr. Graham Ensell, head of INNOS fabrication, University of Southampton.

[15] J. Roth, *Industrial plasma engineering (Volumes 1 and 2)*, Institute of physics publishing, 2000.

[16] Junji Itoh, Koji Uemura, and Seigo Kanemaru, *Three-dimensional vacuum magnetic sensor with a Si emitter tip*, J. Vac. Sci. Technol. B 16.3, 1998.

Chapter 5

Experimental Results and Discussion

5.1. Demonstrating field emission

The processes of field emission have already been discussed in chapter two, though they are further discussed here using field emission maps for further comparison of the first and second generation of devices.

Figure 5.1(top) shows the rectification characteristic of the device for the received gate current over gate-cathode voltage, with the corresponding Fowler Nordheim plot shown (bottom), revealing gate and cathode tip radii of 50 nm and 100 nm, respectively. The techniques described in chapter two. It was found that these figures reflect typical radii for devices of this type [1], which has been confirmed by electron microscopy.

Figure 5.1(top) also indicates that a gate voltage of ±70 Volts appears to be sufficient to initiate field emission from the gate or cathode tip surface. As described in chapter two, p. 38, this is due to the gate sharpness being equal to, or greater than the cathode sharpness. This is of small concern due to the fact that devices are intended to run under forward bias (red lines only).

A preliminary conclusion from this experiment is that device geometry defined during the fabrication process has allowed for emission current of the order of a micro-amp, given a typical current density of $4x10^3$ A/cm^2 [2]. The current also appears to be stable over the lifetime of the device without thermal failure occurring, although data has been collected only over twelve hours. Because field emission is a stochastic process, devices are subject to variation, with the possibility of thermal failure occurring due to nanoprotrusions that may be created from ion bombardment, or by a slow decrease in emission efficiency by the erosion of the tips (and reducing the field enhancement factor β) by adsorption of ions onto the tip surface as suggested in chapter two.

Miyamoto's [3] research on emitter tip stability shows that in devices used in this configuration of a low anode and substrate voltage relative to a gate-cathode voltage, that emitter lifetime decreases rapidly in accordance with electrons that strike the gate, with cathode-gate electrons having a higher energy than any other destination electrons (cathode-anode or cathode-substrate electrons), and therefore gate-cathode ions (positively charged ions striking the cathode from the gate), have enough energy to destroy the tip. Alternatively, below a critical destruction energy level, these gate-cathode ions become adsorbed on the tip surface. Miyamoto concludes that the lifetime of the tip is dependent upon the geometry of the device, vacuum level, voltages at which it is used, and configuration in which the device is used. An in-depth model of tip erosion is suggested in the next chapter, future work.

Further proof of field emission is shown in figures 5.2 and 5.3 which show the field emission maps, where a large negative voltage has been placed on the substrate, encouraging emitted electrons to strike a phosphor screen which is parallel to the device. These images not only indicate that field emission has taken place, but they also demonstrate the nature of the e-beam profile for the first and second generation of devices (figures 5.2 and 5.3 respectively). Comparison of these images shows the non-Gaussian beam profile for the first generation of devices and more Gaussian beam cross-section for the second generation of devices. This was also demonstrated in chapter three, figure 3.8, in which the measured current deviation for the first generation was found to be twice that of the second generation due to factors discussed in chapter three. The figures also indicate that the peak intensity position (darkest red areas of the images) are akin to a random walk for the first generation sample, where the variance in spot intensity location is high compared to the more stable second generation.

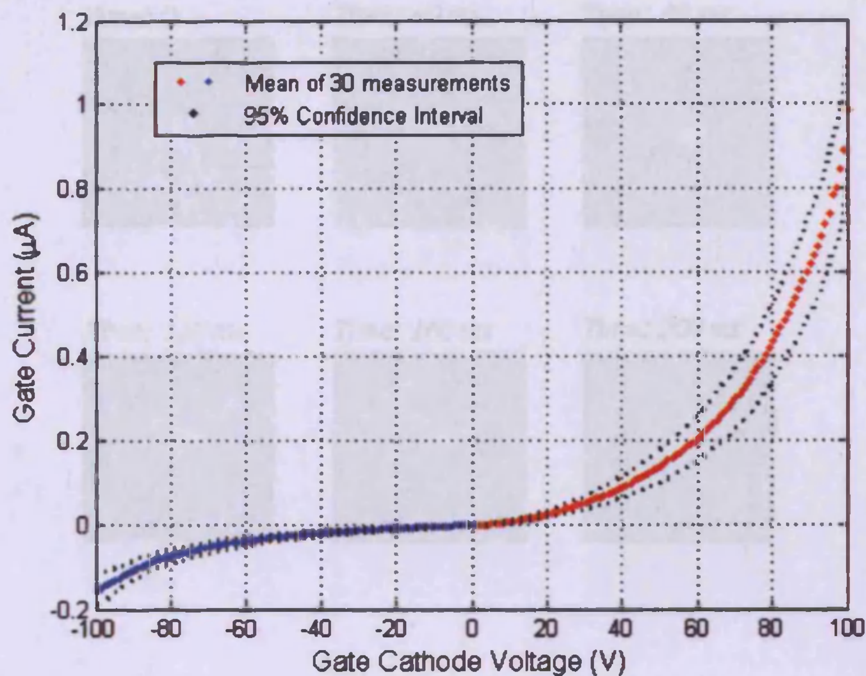

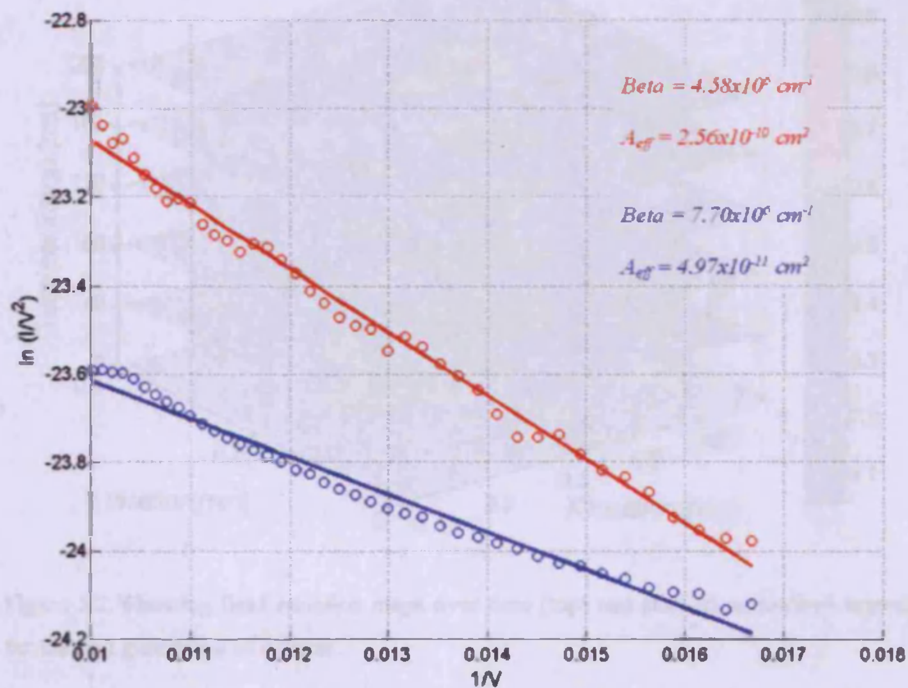

Figure 5.1. Showing rectified characteristic of the device for current against gate-cathode voltage (top), and corresponding Fowler Nordheim plots (bottom).

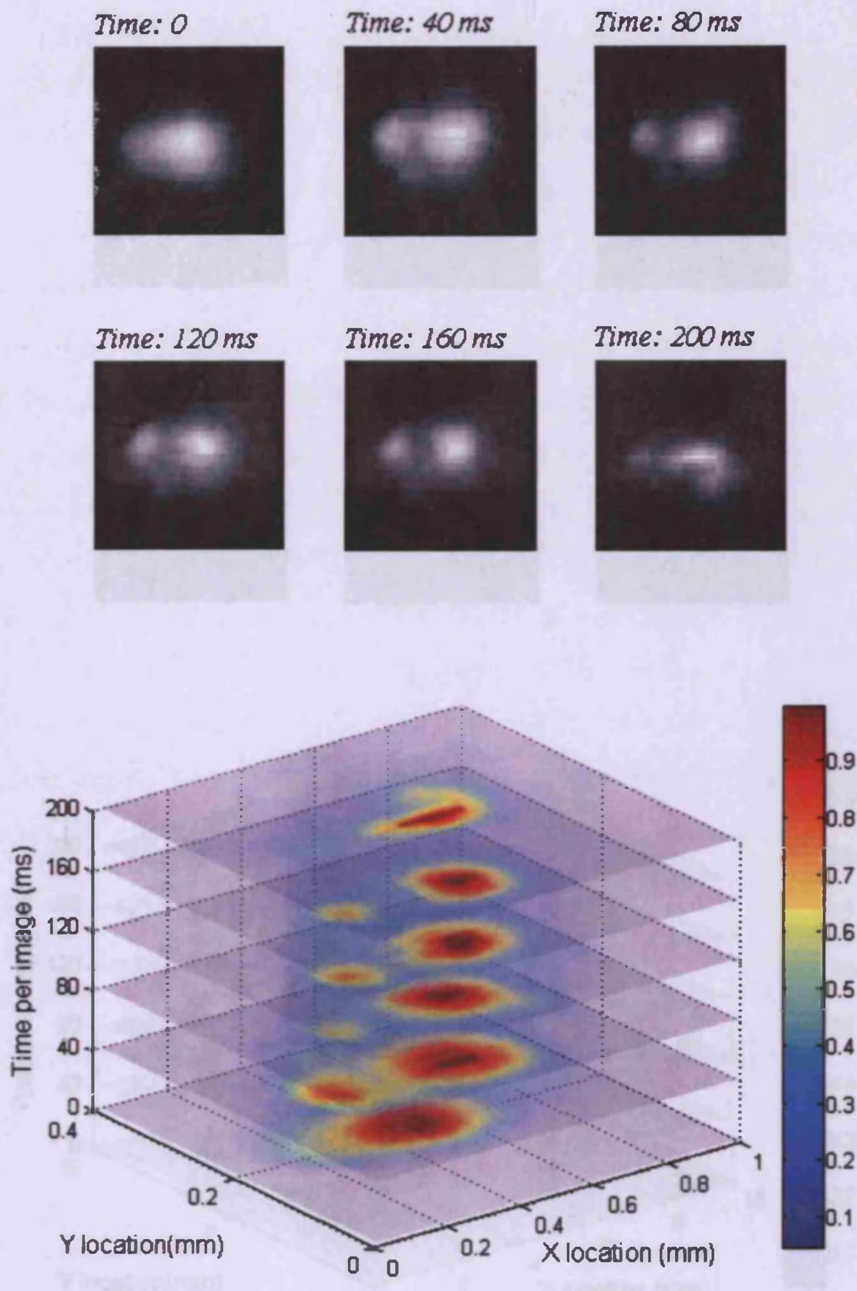

Figure 5.2. Showing field emission maps over time (top) and stacked normalised intensity plots (bottom) for the first generation of devices.

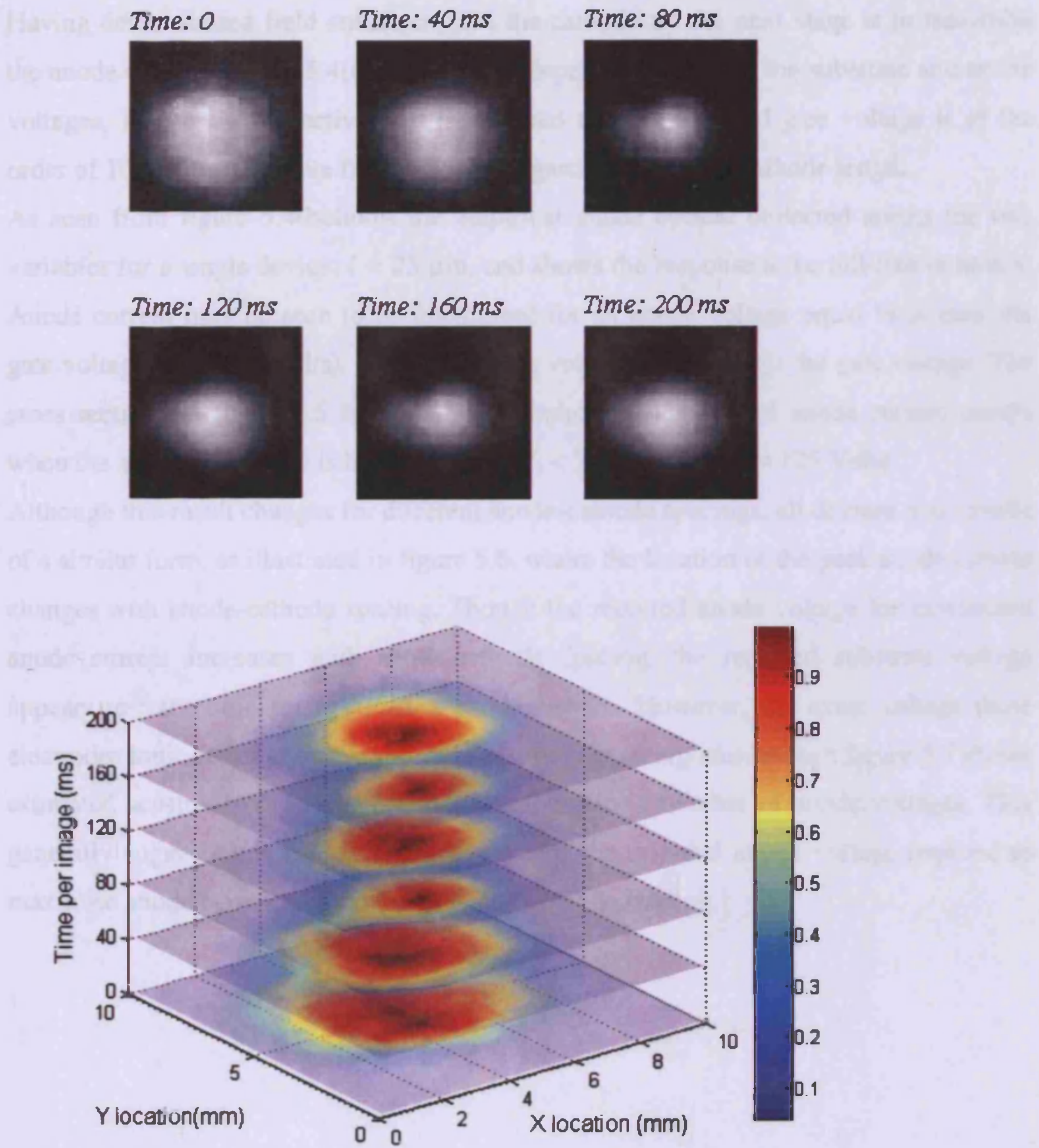

Figure 5.3. Showing field emission maps over time (top) and stacked normalised intensity plots (bottom) for the second generation of devices.

5.2. Maximising anode current under quiescent magnetic fields

Having demonstrated field emission from the cathode tip the next stage is to maximise the anode current. Figure 5.4(top) shows the dependence of I_a on the substrate and anode voltages, V_s and V_a, respectively. It is assumed that the required gate voltage is of the order of 100 Volts to initiate field emission regardless of anode-cathode length.

As seen from figure 5.4(bottom) the empirical anode current collected across the two variables for a single device; $l = 25$ μm, and shows the response to be hill-like in nature. Anode current may be seen to be maximised for an anode voltage equal to at least the gate voltage ($V_g = 100$ volts), with a substrate voltage equal to half the gate voltage. The cross sections in figure 5.5 support this by indicating maximised anode current occurs when the substrate voltage is bound by $30 < V_s < 70$ volts, for $V_a \approx 125$ Volts.

Although this result changes for different anode-cathode spacings, all devices give results of a similar form, as illustrated in figure 5.6, where the location of the peak anode current changes with anode-cathode spacing. Though the required anode voltage for maximised anode current increases with anode-cathode spacing, the required substrate voltage appears to vary little for maximised anode current. However, the exact voltage these electrodes must be set at for maximised sensitivity is ambiguous, though figure 5.7 shows estimated sensitivity over anode-cathode spacing for a number of anode voltages. This generally suggests that sensitivity is highest for the minimal anode voltage required to maximise anode current, regardless of anode-cathode spacing.

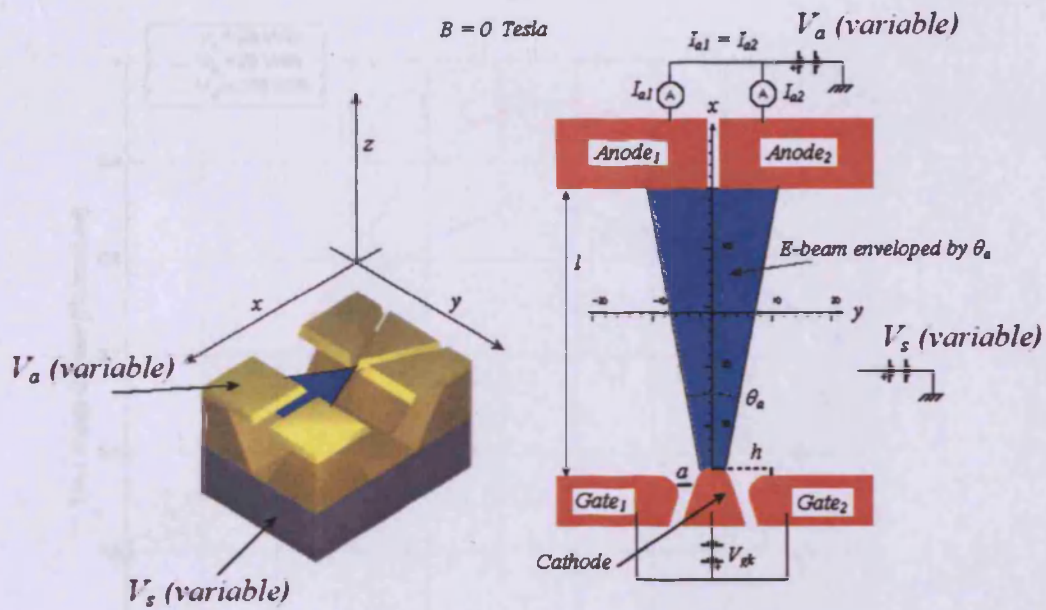

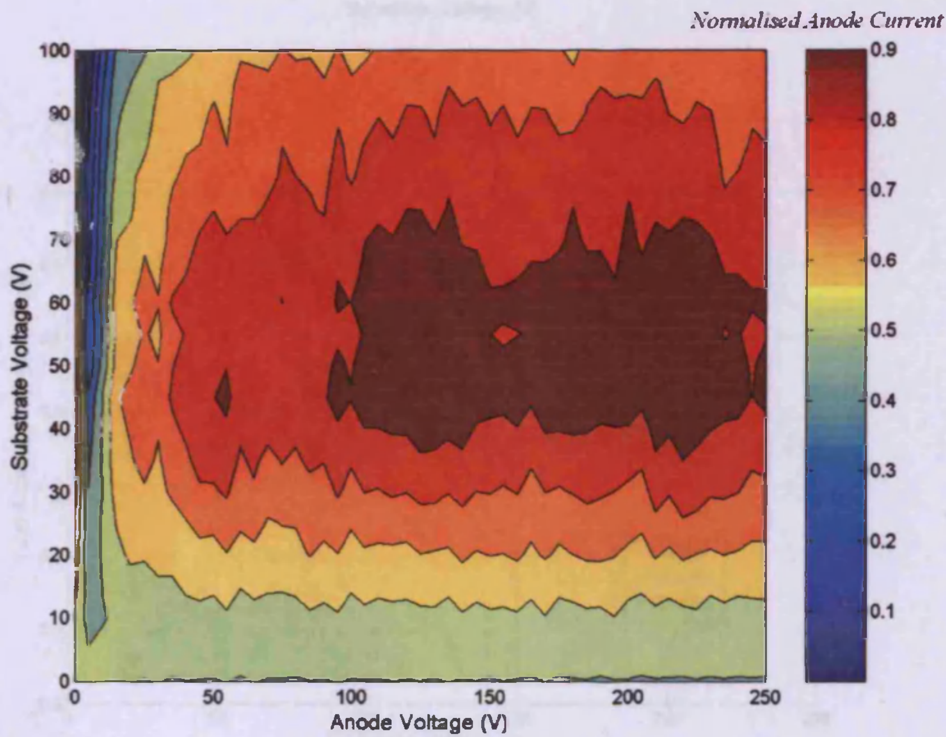

Figure 5.4. A schematic for maximising anode current (top) and empirical (normalised) anode current values across the two variables for a typical device (bottom).

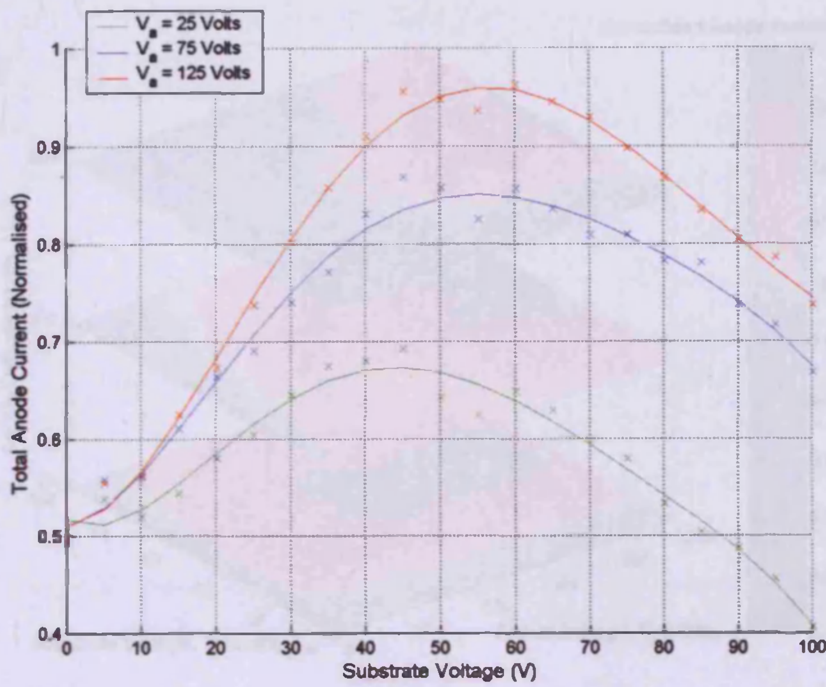

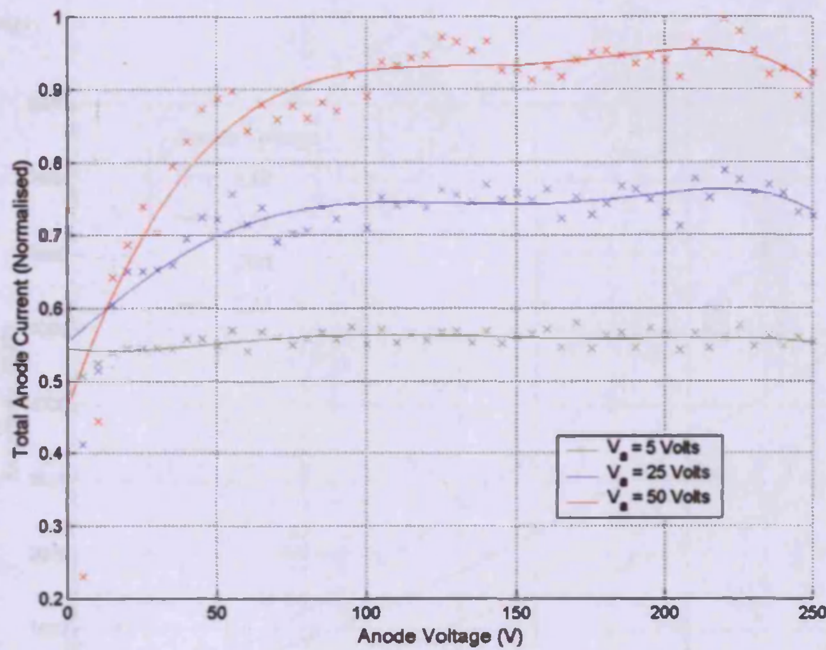

Figure 5.5. Taken from the above figure, showing cross sections of data through one variable keeping the other variable constant.

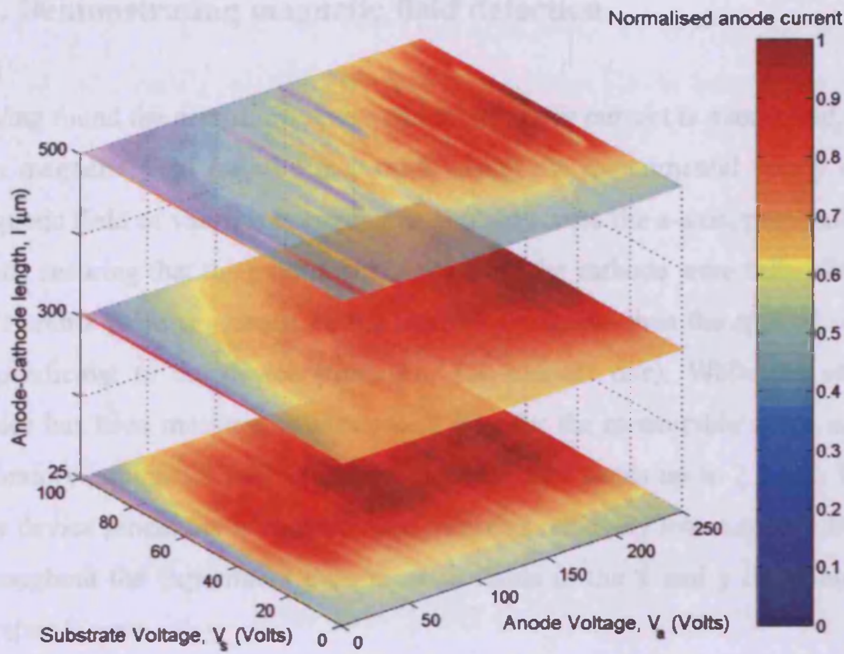

Figure 5.6. Anode current over substrate and anode voltage configurations for a number of anode-cathode spacings

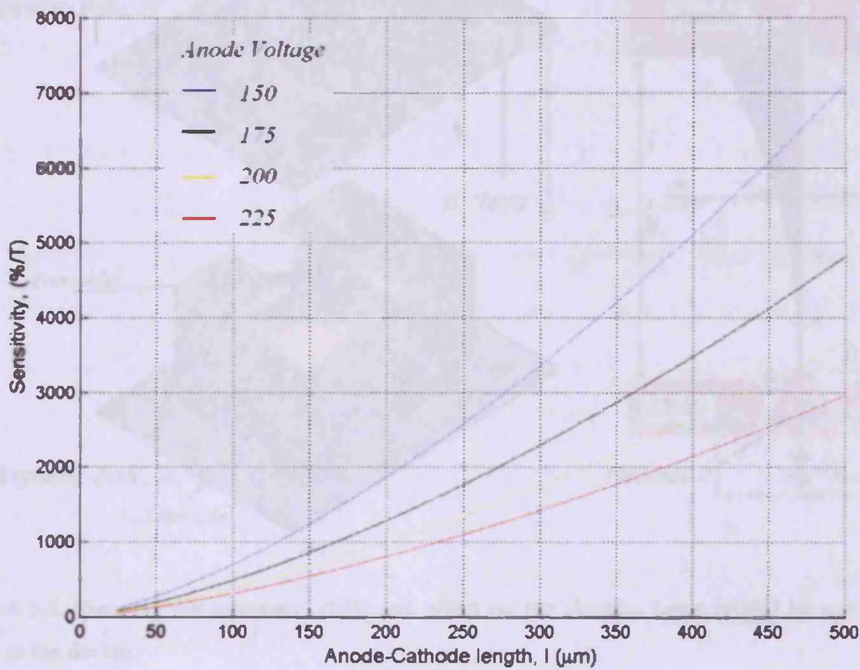

Figure 5.7. Device sensitivity as a function of anode-cathode length for different anode voltages.

5.3. Demonstrating magnetic field detection

Having found the conditions under which the anode current is maximised, device reaction to a magnetic field may be measured. Using the experimental set up of figure 5.8, a magnetic field of varying strength was applied across the z-axis, perpendicular to the xy-plane, ensuring that the emitted electrons from the cathode were fully affected by B_z, i.e. the Lorentz force is greatest on the emitted electrons when the applied magnetic field is perpendicular to the device (from Eq. 1.1, chapter one). While the sensitivity of the device has been measure, unfortunately data for the measurable range is limiting as the laboratory equipment may only generate magnetic fields up to 2.5 mT. Because of this, only device sensitivity is characterised over this relatively low magnetic field range.

Throughout the experiment the magnetic fields in the x and y directions of the sensor were set to zero.

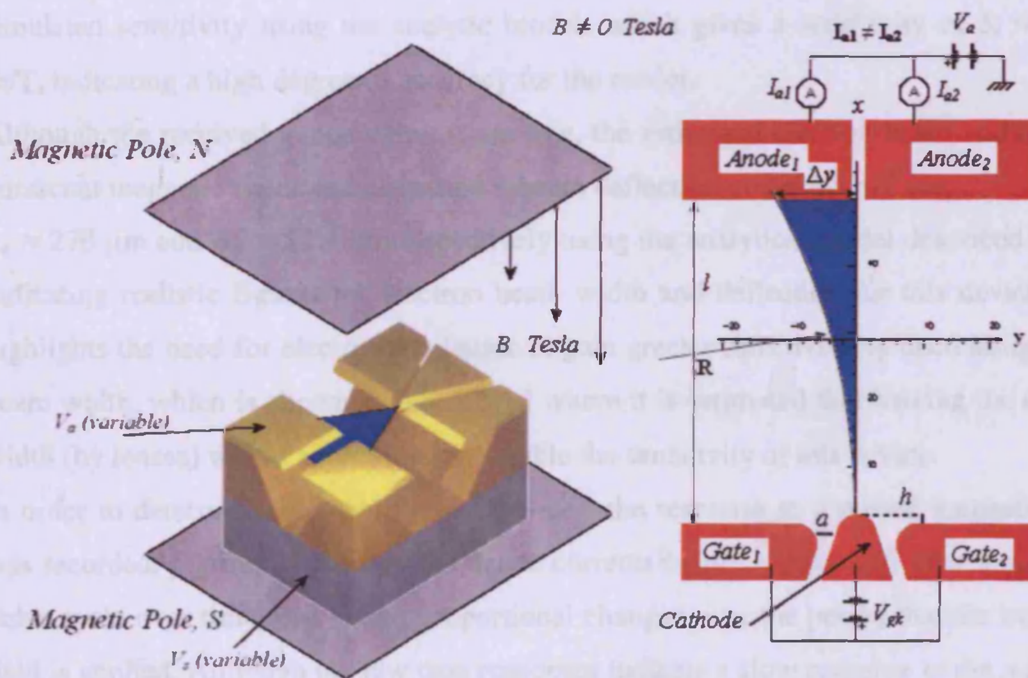

Figure 5.8. Showing the schematic (left) and effect on the electron beam (right) by applying a magnetic field to the device.

The result of this experiment may be seen in figure 5.9(top) where the change in individual anode currents are seen over a magnetic field applied perpendicular to the sensor in the z-direction. The device tested had an anode-cathode distance of 500 μm, and required gate and anode voltages of 100 and 200 Volts respectively, in order to maximise the anode current.

Linear regression shows a proportional change of anode currents on applied magnetic field in figure 5.9(top), where each point measured is the mean of five measurements of the currents received at the split anodes. Electron beam skew is seen under quiescent magnetic fields, which is thought to result from misalignment of the cathode with the anode electrodes, as discussed in chapter three.

The differential anode current over magnetic field may be seen in figure 5.9(bottom), where the gradient over the applied magnetic field range of up to 2.5 mT showed high linearity and a sensitivity of S_e = 3,960 %/T, believed to be the highest sensitivity recorded for a planer magnetometer device [4 and 5]. The result is extremely similar for simulated sensitivity using the analytic model, which gives a sensitivity of S_s = 3,660 %/T, indicating a high degree of accuracy for the model.

Although the received anode currents are low, the estimated electron beam width under quiescent magnetic fields and estimated e-beam deflection under 2.5 mT are,

$y_w \approx 270$ μm and $\Delta y \approx 12.4$ μm respectively using the analytical model described above, indicating realistic figures for electron beam width and deflection for this device. This highlights the need for electrostatic lenses to gain greater sensitivity by decreasing the e-beam width, which is shown in figure 5.10 where it is estimated that halving the e-beam width (by lenses) would approximately double the sensitivity of this device.

In order to determine the stabilities of devices, the response to a pulsed magnetic field was recorded. Figure 5.11 shows the anode currents before, during and after a magnetic pulse cycle over time, and shows proportional changes over the period that the magnetic field is applied. Although the raw data responses indicate a slow response to the magnetic field, this is due to the response time of the Helmholtz coil applying the field and not the actual response of the device.

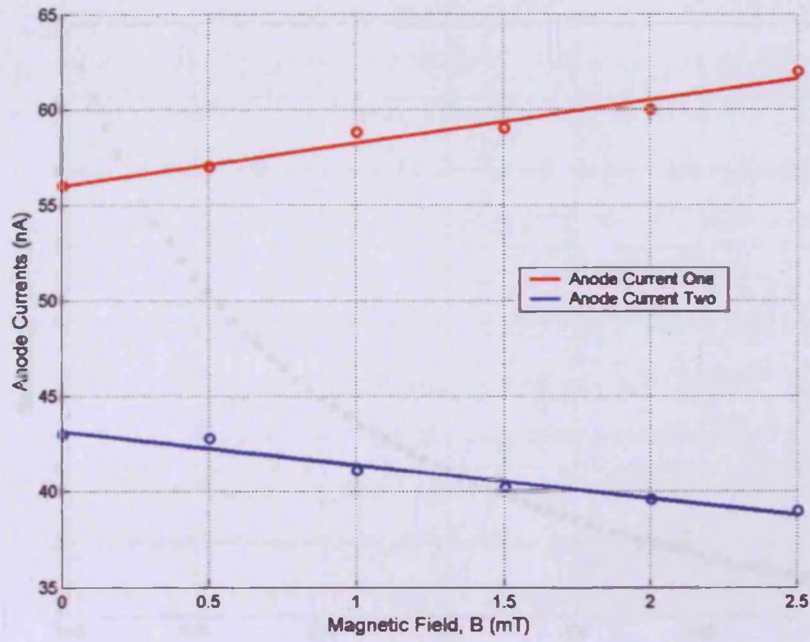

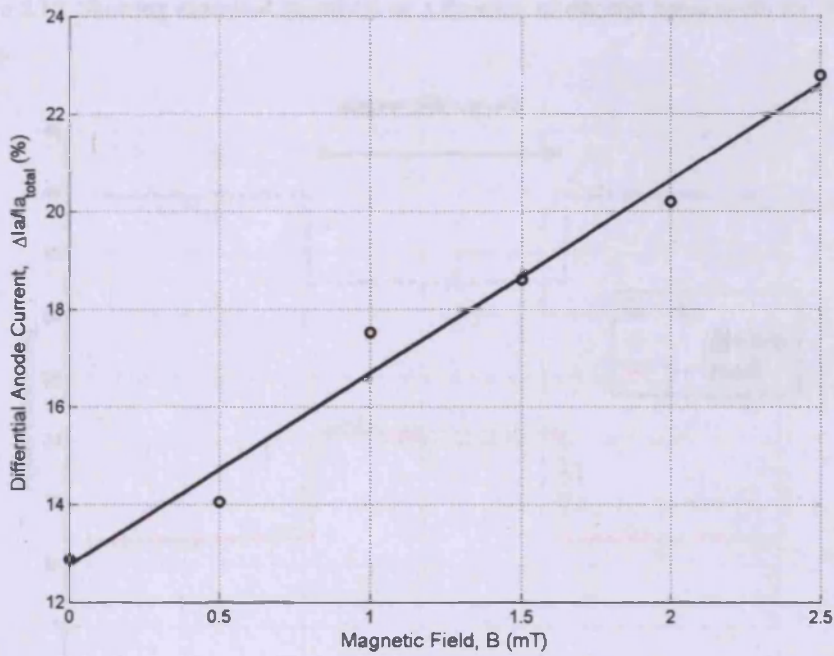

Figure 5.9. Individual anode currents over applied magnetic field (top) and differential anode current as a percentage over applied magnetic field (bottom).

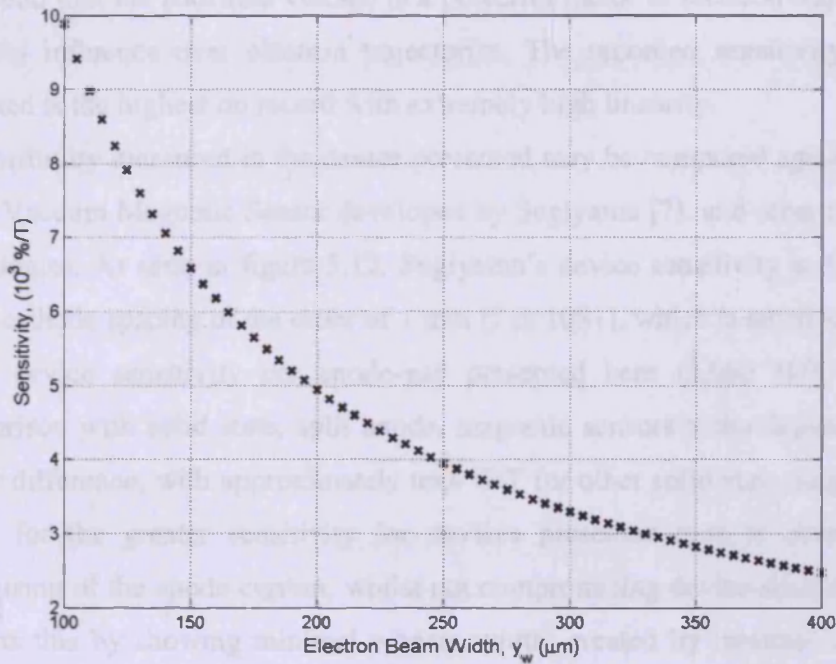

Figure 5.10. Showing estimated sensitivity as a function of electron beam width for the device described above.

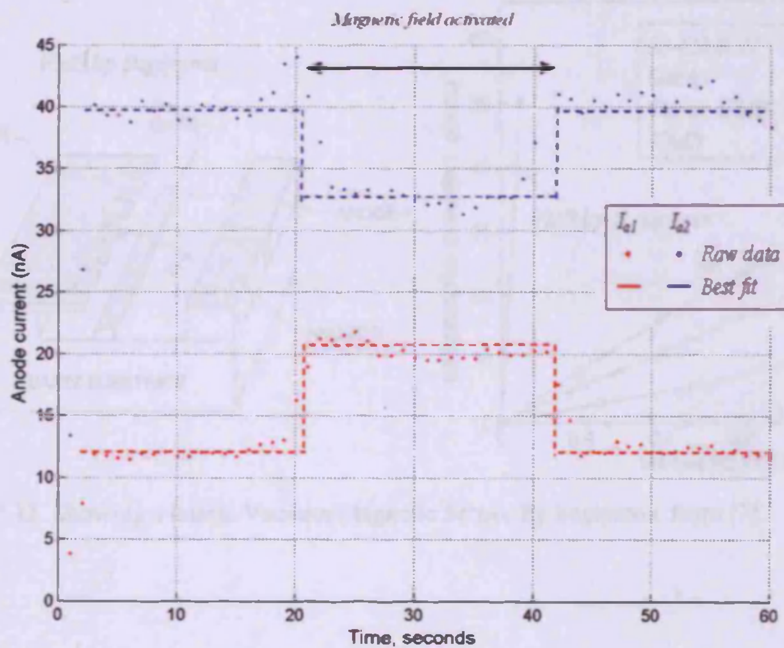

Figure 5.11. Showing anode current response over time with a pulse of magnetic field (of 3 mT) applied for approximately 20 seconds for the device presented above.

Overall, the results obtained are of a similar form to those predicted in simulations, and it was found that the substrate voltage is a powerful factor in electron trajectory and has a powerful influence over electron trajectories. The recorded sensitivity for the device presented is the highest on record with extremely high linearity.

The sensitivity measured in the device presented may be compared against an alternative lateral Vacuum Magnetic Sensor developed by Sugiyama [7], and other magnetic sensing technologies. As seen in figure 5.12, Sugiyama's device sensitivity is 1,000 %/T for an anode-cathode spacing of the order of 1 mm [7 p. 1081], which is small when comparison to the device sensitivity per anode-gap presented here (3,960 %/T over 500 μm). Comparison with solid state, split anode, magnetic sensors technologies shows an even greater difference, with approximately tens %/T for other solid state magnetometers. The reason for the greater sensitivity for devices presented here is characterisation and maximising of the anode current, whilst not compromising device sensitivity; figure 5.10 supports this by showing minimal e-beam width, created by minimal anode voltage to draw all emitted electrons, significantly increases device sensitivity.

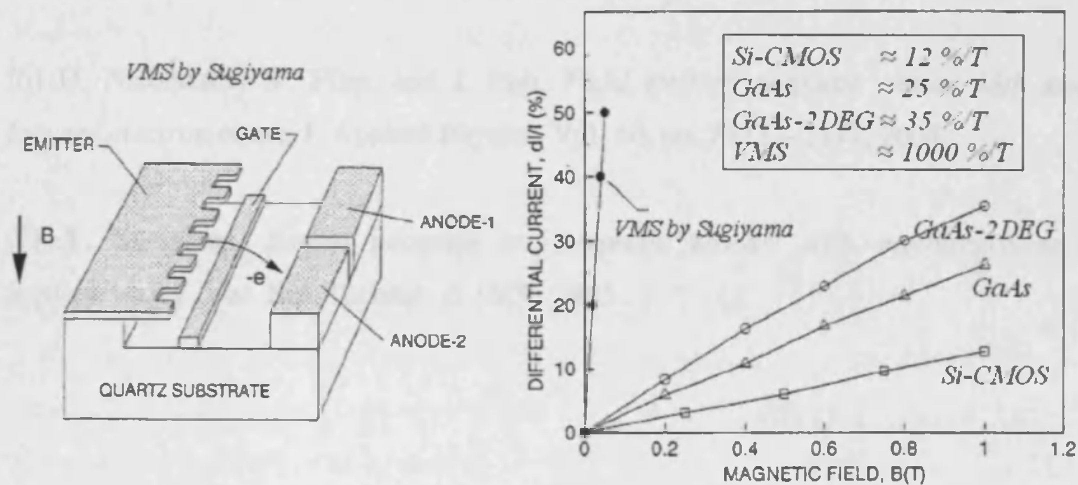

Figure 5.12. Showing a lateral Vacuum Magnetic Sensor by Sugiyama, from [7].

5.4. References

[1] H. Busta, *Review of Vacuum microelectronics*, Amoco Research Centre, 1992.

[2] R. Gomer, *Field Emission and Field Ionization*, Oxford University Press, London, 1961.

[3] N. Miyamoto, H. Adachi, H. Nakane, and K. Yamane, *Emission stability of a field emitter array observed by an emission microscope*, (JVST B) Microelectronics and Nanometre Structures, 2003.

[4] D. Nicolaescu and V. Filip, *Modelling of a magnetic sensor based on vacuum field emission*, Applied Surface Science 94/95, pp. 87-93, 1996.

[5] J. Itoh, K. Uemura, and S. Kanemaru, *Three-dimensional vacuum magnetic sensor with a Si emitter tip*, J. Vac. Sci. Technol. B 16.3., 1998.

[6] D. Nicolaescu, V. Filip, and J. Itoh, *Field emitter magnetic sensor with steered focused electron beam*, J. Applied Physics, Vol. 40, pp. 2173 – 2177, 2001.

[7] Y. Sugiyama, *Recent progress on magnetic sensors with nanostructures and applications*, J. Vac. Sci. Technol. B 13(3), 1995.

Chapter 6

Conclusions

6.1. Achievements of this work

This thesis describes current research on the development of field-emission magnetic sensors undertaken at the Department of Electronic and Electrical Engineering in University College London. Each of the chapters is devoted to development of the sensor with plans for future work also being presented where necessary.

The first chapter gives a literature review of current magnetometer technologies which was undertaken for two reasons; to lay the foundation for the field emission magnetic sensor, and to find a suitable reference magnetometer for the project. The fundamentals of the field emission magnetometer are then introduced in the second chapter, where an account of field emission magnetometer operation and alternative designs is given. Within this chapter, different types of electron emission are discussed with attention paid to field emission and the Fowler Nordheim equation, allowing for the cathode emitting radius to be found by empirical means. Factors affecting field emission are also investigated at this stage, with stochastic processes found to govern emitted current within the device. Scanning Electron Microscope images are used throughout the text to confirm emitter sizes and the nature of cathode tip changes.

The third chapter gives an account of the experimental setup in the laboratory and magnetometer evolution. The experimental setup for testing is given in which the triaxial Helmholtz coil system is documented which is used to cancel the Earth's magnetic field including any local field variations. Device evolution is then documented with attention paid to the cathode tip, the design of which involved empirically optimisation in which a series of experiments leads to the conclusion that extremely sharp tips (or cathode radii under 10 nm) causes device failure by Joule heating, indicated in figure 6.1(top), and devices that are not sharp enough (or cathode radii that are greater than 100 nm), are insufficiently sharp to instigate field emission. This narrow band of cathode radii of

approximately, 10 nm < r_k < 100 nm, not only appears to be sufficient to generate field emitted electrons using the voltage range available within the laboratory, which of the order of 100 Volts, but was found to be reproducible as indicated in chapter two, figure 2.4.

First generation sample
Radius of curvature: ~10 nm

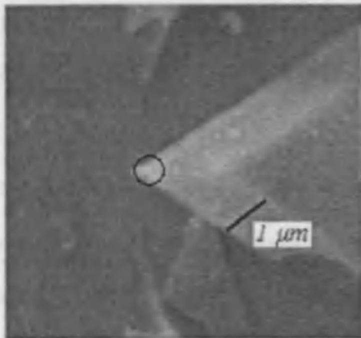

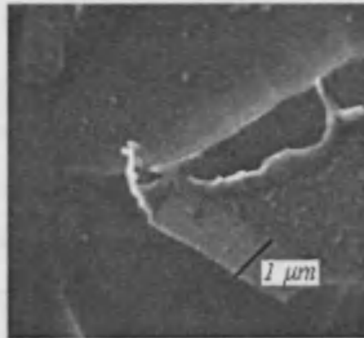

Second generation samples
Radius of curvature: ~100 nm

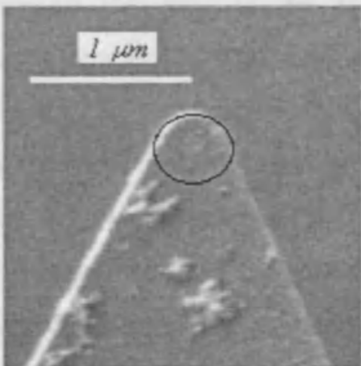

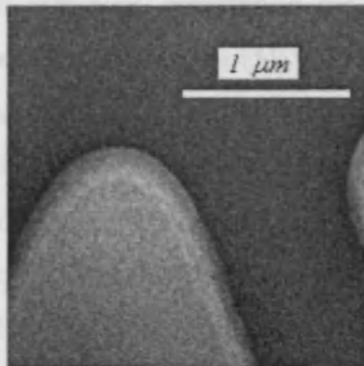

Figure 6.1. Showing the development of the cathode tip for the first generation of devices, which also show thermal failure (top left and right respectively), and samples from the second generation of devices (bottom). All radii of curvature in the above images are not to scale.

Other fabrication issues investigated were fractal-like edges of cathode tips found at the submicron level within the first set of devices. In order to investigate edge roughness within devices, the Hausdorff Dimension dimensional scale was employed to give a quantitative measure of roughness by the box counting algorithm. This algorithm, developed in MATLAB, functioned by uploading Scanning Electron Microscope images of the devices which gave detail at a submicron level, and using the box counting method

gave the Hausdorff Dimension as described in chapter three. By this method it was found that images of the first generation of cathode tips are largely self-similar and scale invariant or fractal in nature. It is believed that this is the first time that the Hausdorff Dimension dimensional scale was used in fractal analysis for lateral field emitters, and has been shown to give excellent quantitative measure of roughness as demonstrated in the third chapter.

Analytic and numerical models are presented in the fourth chapter, where device behaviour is modelled, and device characterisation is given based on the empirical results of the previous chapters. This is compared in the fifth chapter that gives, firstly, device optimisation using the models previously developed to maximise the anode current for a single device, and then shows device response to a magnetic field. The characteristics showed high linearity over the applied magnetic field range of up to 2.5 mT, and a sensitivity of 3,960 %/T was measured from this experiment. The predicted sensitivity by the model was 3,660 %/T, indicating a high degree of accuracy for the model. It is believed that this is the highest recorded sensitivity for a lateral field emission magnetometer [5], with similar devices reported (see [5]) having sensitivities of the order of 1,000 %/T as indicated in the previous chapter.

One issue within the devices is that of e-beam skew under quiescent magnetic fields (figure 5.9). It is believed the cause is nanoprotrusions on the cathode surface at the point of emission (caused by either poor processing or ion bombardment), and may be easily rectified by adjusting the anode voltages to compensate for the skew. Another experiment shown in this chapter is device response to a pulsed magnetic field (figure 5.11). Anode current is shown before, during, and after, a magnetic pulse cycle over time, and shows proportional changes over the period that the magnetic field is applied.

The field emission magnetometer presented is highly linear with the highest recorded sensitivity for a magnetic sensing device based on field emission of a similar structure. This is due to control of the anode current, where the substrate and anodes have been used to maximise anode current without compromising deice sensitivity. However, because extremely sharp emitters are fractal-like in nature, care must be taken when designing the cathode structure otherwise ambiguous results such as e-beam skew and other issues arise, as discussed in previous chapters.

It is for this reason that, unless control electronics are used to eliminate unfavourable factors, it is suggested that field emitters of the type discussed here - relatively thin (300 nm thick), highly doped, lateral, silicon emitter which are of the Spindt-emitter form - are consigned to applications in which the stochastic nature of the cathode tip has little effect upon the system, such as ion sources and Field Emission Electric Propulsion systems as discussed in chapter two.

Overall, it is felt that although a great deal of research into field emitters is still required, a number of analytical and semi-numerical approaches have been adopted and used that successfully investigate the properties of silicon field emitters and field emission magnetometer design, as well as investigating the uses of field emission for other technologies.

6.2. Future work

Ideas for the near and far future are presented for future development of the field emitter magnetometer, and an overview of field emission used in other technologies is given. It has been demonstrated that vacuum microelectronics is a new field which is yet to be utilised to its full potential. The following paragraphs illustrate this with firstly, field emitter magnetometer developments, and secondly, field emission used in other technologies reflecting the use of field emission used across other applications.

Field emitter magnetometer developments: Model Improvements

Far greater improvements to the field emission magnetometer may be achieved by higher order models to estimate factors such as device operation and cathode tip stability. One modification introduced to the model is to fully model the emitted electron energy. All models within this thesis have assumed that all emitted electrons have energies equal to that of the work function, Φ. Although this is a reasonable approximation, as the variance of energy is low for cold cathode emitters [8]. Young [7] has shown that the emitted electron energy distribution is Maxwellian in nature, and therefore the emitted electrons are continuous in position and energy distributions. Figure 6.2 shows the continuous position and energy distributions. In addition to this the red bars represent the discretised versions of these distributions in which electrons of given position and energy are divided into a number of bins.
In this scenario the total emitted energy is the sum of the number of electrons in each bin times the energy of the electrons in that bin, and represents a more accurate model of field emission.

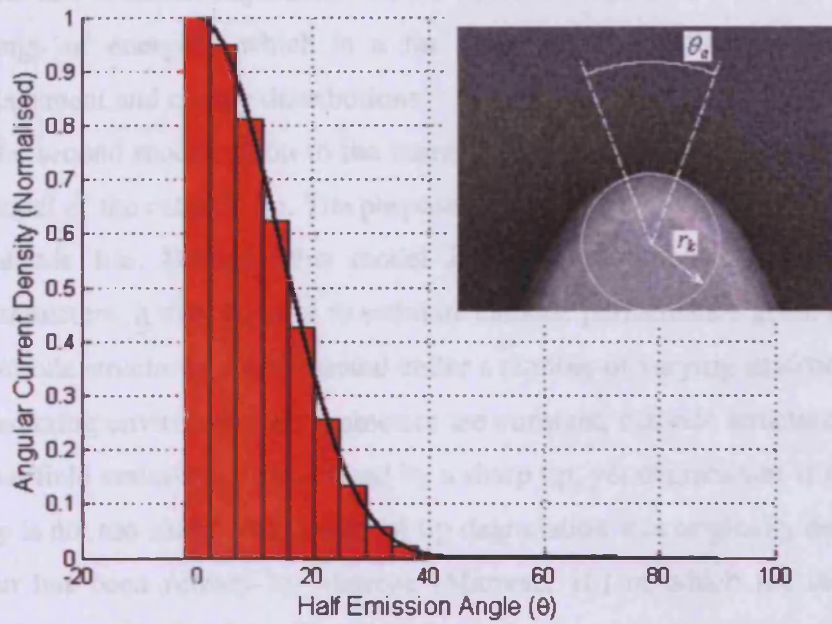

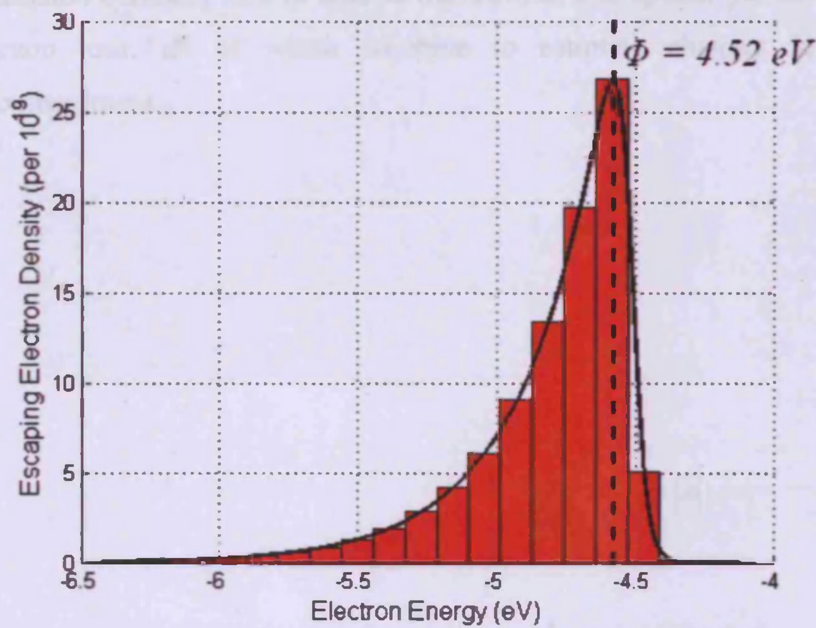

Figure 6.2. Electron density distribution (top) and energy spread (bottom).

The above model adjustment would cover a range of electron positions with a range a range of energies, which is a far more accurate reflection of the emitted electron placement and energy distributions.

The second modification to the numerical model is that of the addition of a degradation model of the cathode tip. The purpose of this is to study cathode tip stability and estimate cathode life. Because this model is based on empirical results and environmental parameters, it may be used to estimate cathode performance given cathode structures, i.e. cathode structures may be tested under a number of varying environmental parameters, or assuming environmental parameters are constant, cathode structure may be optimised so that field emission is maximized by a sharp tip, yet degradation is minimized because the tip is not too sharp. This model of tip degradation was originally developed by Brodie [9] but has been refined by Marrese [Marrese, 10] in which the model predicts cathode emission currents, flux of ions to the surface, and sputter yields of cathode materials by xenon ions, all of which combine to estimate changes in tip radius from ion bombardment.

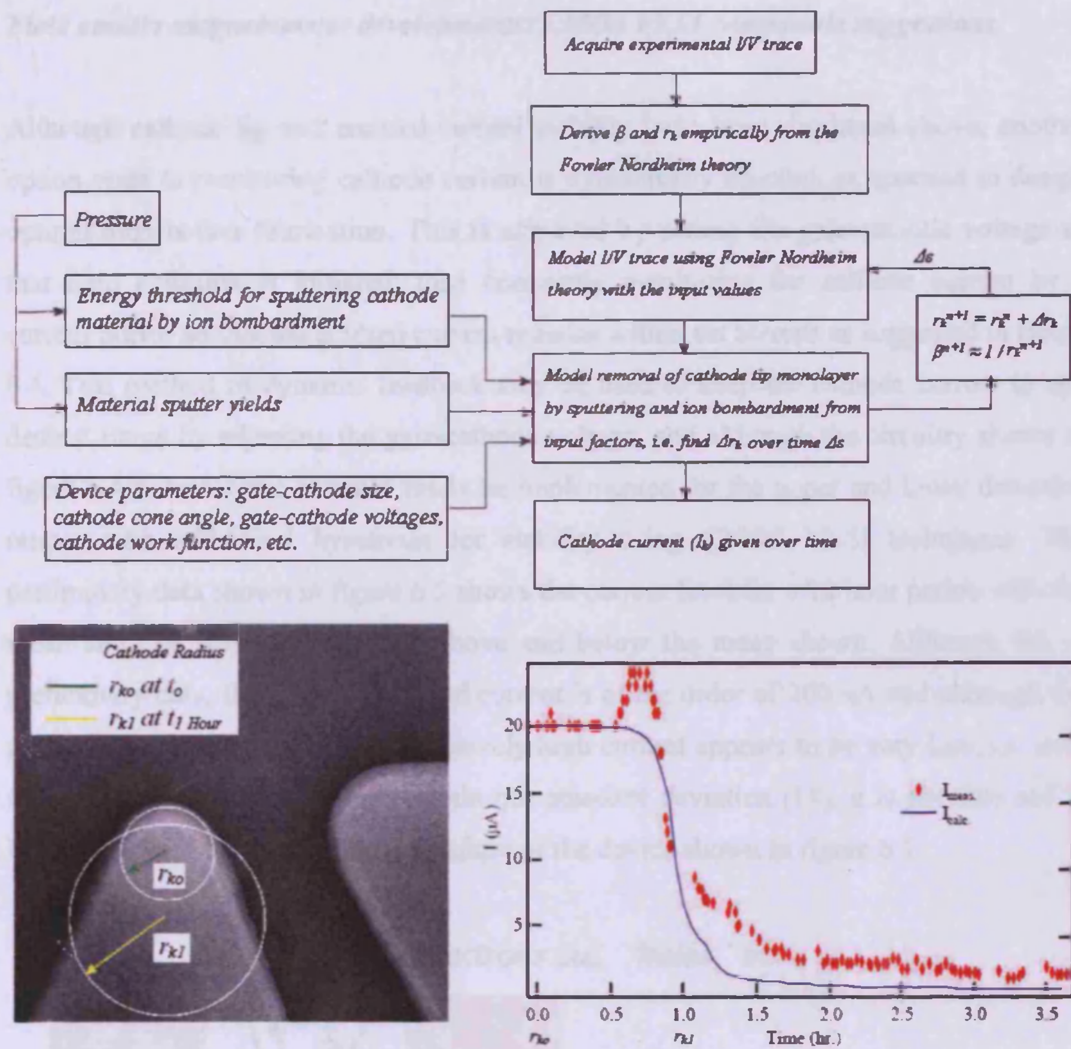

Figure 6.3. Showing (top) the degradation model based on research by Marrese [10], a schematic of how the model would operate (bottom, left) and Marrese's result of empirical and predicated results for a field emitter device of similar structure (bottom, right).

Although the above model is a simplified version of the tip degradation model developed by Marrese, a number of difficulties exist in implementing the above model. It is envisaged that a combination of numerical simulation and appropriate assumptions will be used to accurately predict the behaviour of the cathode with time in the form of electron–solid interactions by stochastic processes [10]. Due to the complexities involved and the time constraints of this project implementation of the above model is not currently possible.

Field emitter magnetometer developments: CMOS VLSI compatible suggestions

Although cathode tip and emitted current stability have been discussed above, another option open to monitoring cathode current is dynamically on-chip, as opposed to design optimisation before fabrication. This is achieved by setting the gate-cathode voltage so that field emission is initiated, then constantly monitoring the cathode current by a current mirror so that the emitted current remains within set bounds as suggested in figure 6.4. This method of dynamic feedback may be used to keep the cathode current to any desired range by adjusting the gate-cathode voltage, and although the circuitry shown in figure 6.4 is first order, it could easily be implemented for the upper and lower detection ranges with additional hysteresis for stability using CMOS VLSI techniques. The preliminary data shown in figure 6.5 shows the current level for a 12 hour period with the mean and one standard deviation above and below the mean shown. Although this is preliminary data, the range of emitted current is of the order of 200 nA and although the probability (in this data set) of excessively high current appears to be very low, i.e. over 68% of the dataset is contained within one standard deviation [11], it is possible and is believed to be the cause of thermal failure of the device shown in figure 6.1.

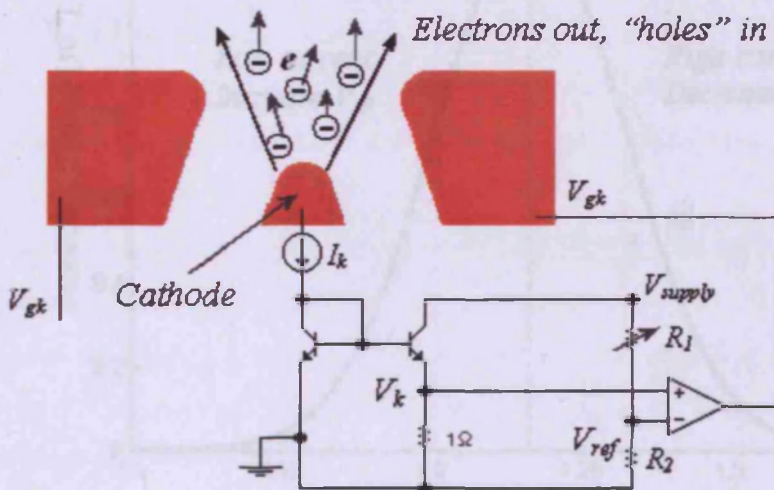

Figure 6.4. Showing the basic schematic for dynamic feedback in controlling the cathode current.

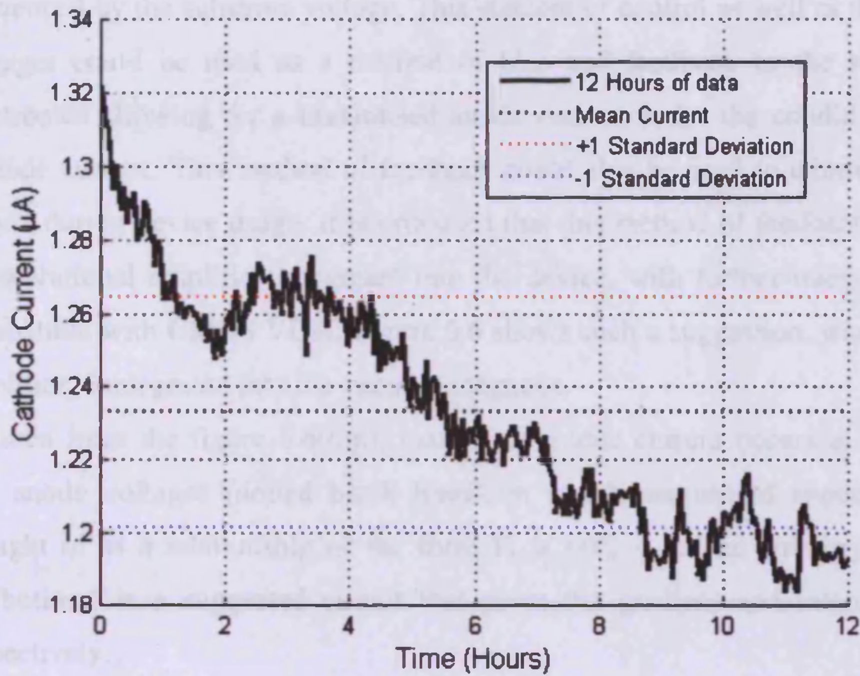

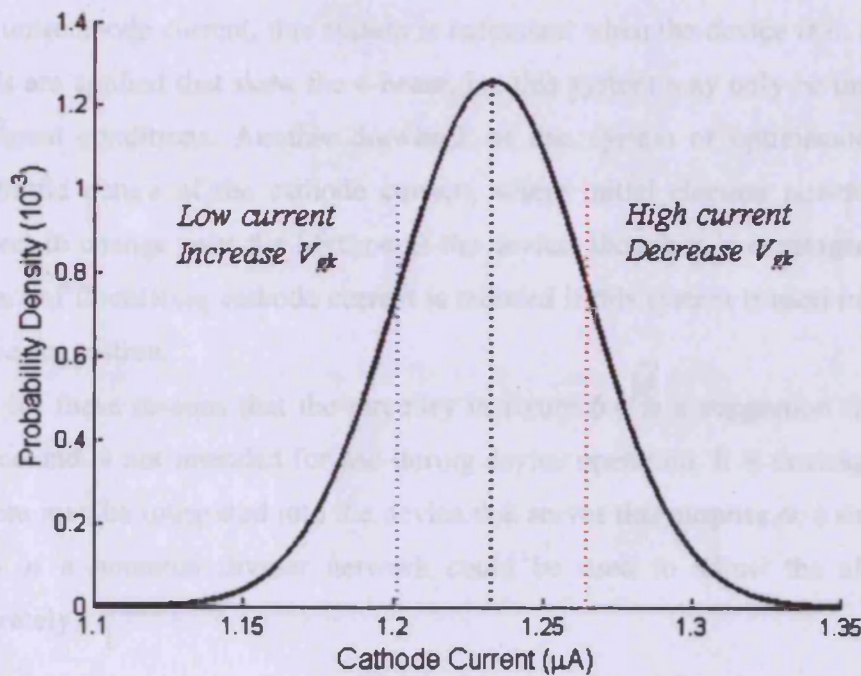

Figure 6.5. Showing the stochastic nature of emitted current over time (top), and the probability density function of the above curve, indicating where the gate voltage should change (bottom).

Research has previously shown that the emitted electron beam may be strongly influenced by the substrate voltage. This element of control as well as the gate and anode voltages could be used as a method of bias and feedback to the sensor via control electronics allowing for a maximised anode current under the conditions of a dynamic cathode current. This method of feedback could also be used to eliminate any drift that occurs during device usage. It is proposed that this method of feedback and control uses an operational amplifier integrated into the device, with further integration of circuitry compatible with CMOS VLSI. Figure 6.6 shows such a suggestion, where an operational amplifier is integrated into the vacuum magnetic.

As seen from the figure 6.6(top), maximised anode current occurs at specific substrate and anode voltages (dotted black lines), in which maximised anode current may be thought of as a relationship of the form $V_s = mV_a + c$. The circuitry shown in figure 6.6(bottom) is a suggested circuit that gives the gradient and intercept of, m and c respectively.

Although this could easily be integrated on chip and would provide dynamic feedback to maximise anode current, this system is redundant when the device is in use and magnetic fields are applied that skew the e-beam, i.e. this system may only be implemented under quiescent conditions. Another drawback of this system of optimisation is that of the stochastic nature of the cathode current, where initial electron position and energy is subject to change over the lifetime of the device, though it is envisaged that the overall impact of fluctuating cathode current is reduced if this system is used in parallel with the above suggestion.

It is for these reasons that the circuitry in figure 6.6 is a suggestion for optimising the device and is not intended for use during device operation. It is envisaged that a similar system may be integrated into the device that serves this purpose or a simplified circuitry such as a potential divider network could be used to adjust the electrode voltages separately.

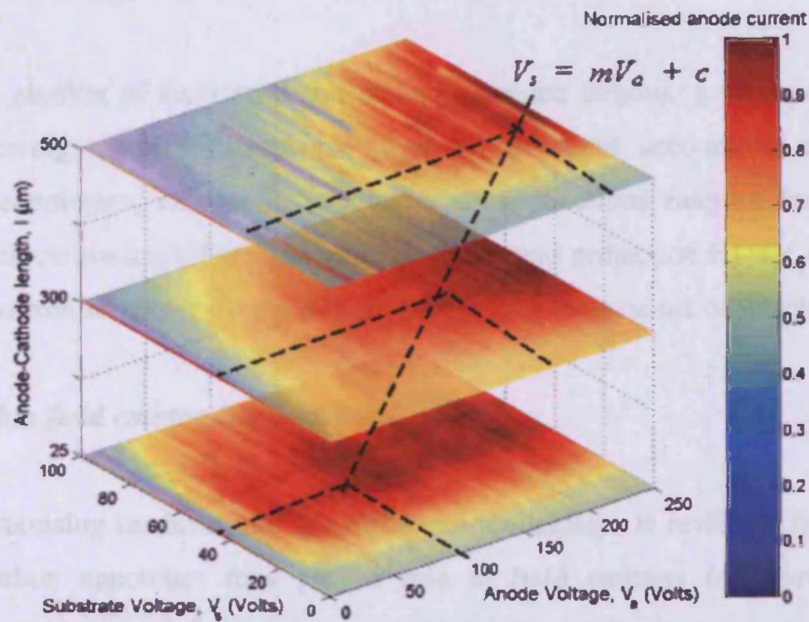

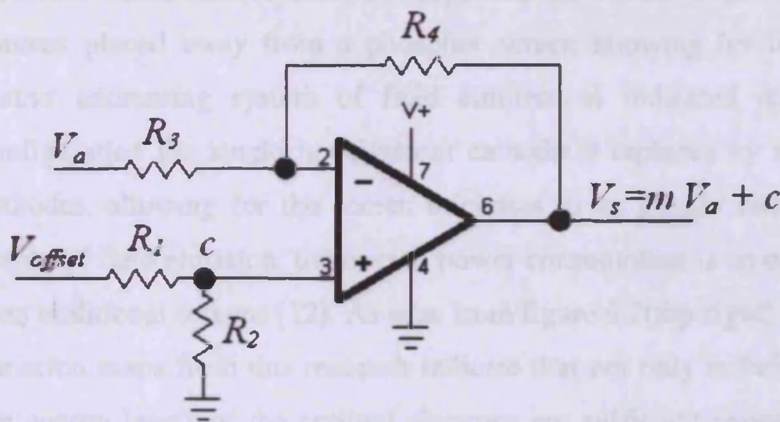

Figure 6.6. Showing anode current over V_s and V_a for different anode-cathode spacings (top) and a schematic of the circuitry that may be used for simplifying device operation.

Field Emission used in other technologies

A number of field emission technologies are beginning to appear in research and are nearing maturity. Busta [5] gives an excellent account of uses of field emission technologies, envisaging a number of applications ranging from; ultra-fast switches, microwave amplifiers and generators flat and projection HDTV display devices, intense electron/ion sources, and e-beam lithography tools, some of which are discussed below.

Thin field emitter displays

Promising research into thin field emitter displays is reviewed by Marsh [12], in which carbon nanotubes may play a role as field emitters for television screens. Carbon nanotube-based field emitters are deposited on a back screen with the array of electron-sources placed away from a phosphor screen allowing for images to be shown by a matrix addressing system of field emitters as indicated in figure 6.7(top). In this configuration the single hot filament cathode is replaced by a series of miniature cold cathodes, allowing for the screen thickness to be greatly reduced and, because of the nature of field emission, the overall power consumption is an order of magnitude smaller than traditional screens [12]. As seen from figure 6.7(top-right), images produced by field emission maps from this research indicate that not only is field emission occurring, but the energy levels of the emitted electrons are sufficient enough to excite the phosphor screen.

Field emission pressure sensors

Exploiting dependence of emission currents on pressure for use in pressure sensors shows promising results, where an inverse relationship between detected anode current and pressure is given in [13] for triode field emission devices. Such a device essentially relates to the vacuum level by measuring the displacement of a anode diaphragm as illustrated in figure 6.7(middle-left), where the anode is physically moved with respect to the cathode in response to outside pressure. Figure 6.7(middle-right) shows the result of a preliminary experiment from one of our devices in which gate current is monitored over pressure. The relationship between gate current and pressure is non-linear, though may still prove useful in pressure sensor devices.

Electron-Beam-Induced Deposition (EBID)

One further area of interest for field emission is that of nanolithography techniques for nanostructuring and nanosoldering [14]. Specifically, a review of Electron-Beam-Induced Deposition (EBID) has been conducted by Rack *et. al.* [15]. EBID is a process by which an electron beam is used to stimulate a gaseous precursor that forms a solid deposit on a substrate. Figure 6.7(bottom) shows a submicron device fabricated by EBID as reviewed by Rack's group. In this work the field emission device is constructed from platinum nanofibers which give excellent field emission characteristics, including cathode tip radii of the order of 7 nm [15, p. 84], allowing for much lower gate-cathode voltages to initiate electron emission.

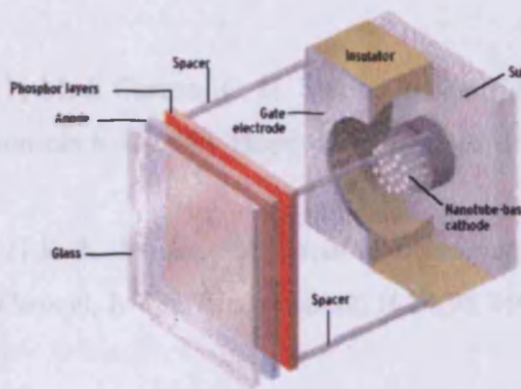

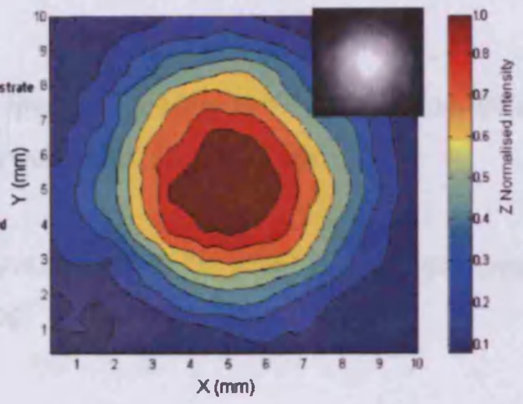

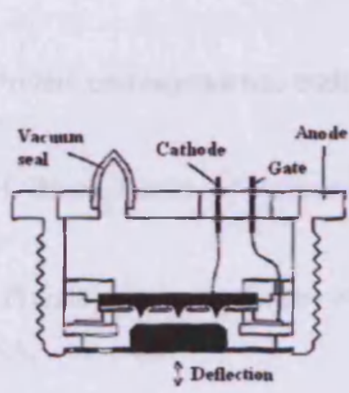

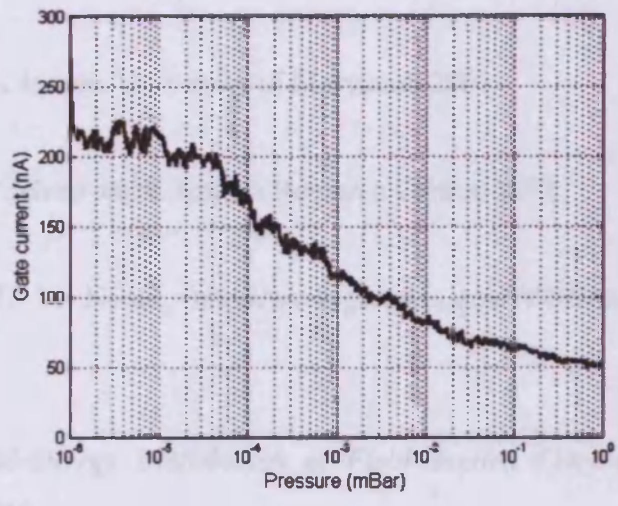

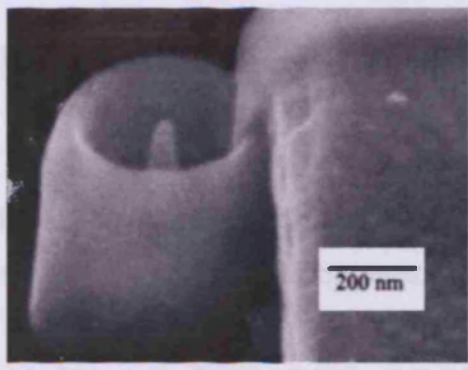

Figure 6.7. Showing uses of field emission in flat screens (top-left from [12]), pressure sensors (middle-left, from [5]) and nanolithography (bottom, from [15]).

6.3. References

[1] M. J. Caruso, C. H. Smith, *A New Perspective on Magnetic Field Sensing*, Magnetic sensors tutorial by Honeywell, www.honeywell.co.uk, October 2000.

[2] K. L. Jensen, *Analytical and seminumerical models for gated field emitter arrays (I. Theory)*, J. Vac. Sci. Technol. B 14(3), 1996.

[3] K. L. Jensen, *An Introduction to Electron Emission Physics and Applications, lecture notes: Beam Physics Course*, Inst. Res. El. & Appl. Phys, University of Maryland, 2005

[4] Private correspondence with K. L. Jensen, University of Maryland, 2007.

[5] H. Busta, *Review of Vacuum microelectronics*, Amoco Research Centre, 1992.

[6] Private correspondence with J. V. Noord, http://www.grc.nasa.gov/WWW/ion/, NASA.

[7] R. D. Young, *Theoretical Total-Energy Distribution of Field-Emitted Electrons*, Physical Review, Vol. 113, No. 1, 1958.

[8] R. Gomer, *Field Emission and Field Ionization*, Oxford University Press, London, 1961.

[9] Brodie, I., *Bombardment of Field-Emission Cathodes by Positive Ions Formed on the Inter-electrode Region*, Int. J. Electronics, 38(4), 1975.

[10] C. M. Marrese, *Compatibility of field emission cathode and electric propulsion technologies*, submitted for Ph.D. Thesis at the University of Michigan, Aerospace Engineering, 1999.

[11] A. Croft, M. Hargreaves, R. Davison, *Engineering Mathematics*, Prentice-Hall, 2001.

[12] P. Marsh, *High-tech vision for cheap flat-screen TV's*, Financial Times, 26th August 2003.

[13] A. Angelcscu Et. Al. *Technology for Field Emission Pressure Sensors*, http://ieeexplore.ieee.org/iel5/7142/19237/00889126.pdf?arnumber=889126

[14] H. W.P. Koops, C. Schossler, *Construction of a three-dimensional microtriode by nanolithography with electron-beam induced deposition*, 9th International Vacuum Microelectronics Conference, 1996.

[15] S. J. Randolph, J. D. Fowlkes, and P. D. Rack, Focused, *Nanoscale Electron-Beam-Induced Deposition and Etching*, Critical Reviews in Solid State and Materials Sciences Vol. 31, pp. 55–89, 2006.

Appendix A

A.1. Matlab scripts

```
%%%%%%%%%%%%
% Used to find the Hausdorff Dimension via the box counting method
% email: p.french@ee.ucl.ac.uk
% web: www.ee.ucl.ac.uk/~pfrench
%%%%%%%%%%%%
clear all
close all
table =[,2];

% load up original image and convert to gray-scale
p = imread(ImageName.jpg');
%p = rgb2gray(P);

figure(1)
imshow(p)

% detect the edge of image 'p' using the Canny algorithm
% this gives edge as 'e2'
bw = im2bw(p, graythresh(p));
e  = edge(double(bw));
fi = imfill(bw, 'holes');
op = imerode(fi,strel('disk',4));
e2 = edge(double(op));

figure(2)
imshow(e2)


% once we have e2, set up a grid of blocks across the image
% and scan each bloch too see if the edge occupies any of the blocks.
% If a block is occupied then flag it and record it in boxCount --
% store both size of blocks (numBlocks) and no of occupied boxes (boxCount)
% in table()
Nx = size(e2,1);
Ny = size(e2,2);

for numBlocks = 1:20

  sizeBlocks_x = floor(Nx./numBlocks);
  sizeBlocks_y = floor(Ny./numBlocks);

  flag = zeros(numBlocks,numBlocks);
  for i = 1:numBlocks
    for j = 1:numBlocks
      xStart = (i-1)*sizeBlocks_x + 1;
      xEnd   = i*sizeBlocks_x;

      yStart = (j-1)*sizeBlocks_y + 1;
      yEnd   = j*sizeBlocks_y;

      block = e2(xStart:xEnd, yStart:yEnd);

      flag(i,j) = any(block(:)); %mark this if ANY part of block is true
    end
  end
  boxCount = nnz(flag);
  table(numBlocks,1)   = numBlocks;
  table(numBlocks,2)   = boxCount;
end
table
```

```
N = length(table);
% from the above table of discrete points, take a line of best fit and plot
% the raw data (ro) and line of best fit (r-)
x     = table(1:N,1);   % x is numBlocks
y     = table(1:N,2);   % y is boxCount

%x = x1(3:length(x1));
%y = y1(3:length(x1));

p     = polyfit(x,y,1);
BestFit = polyval(p,x);

figure(3)
hold on
grid on
plot(x,y,      'bo','LineWidth',1)
plot(x,BestFit, 'b-','LineWidth',2)
xlabel('Number of blocks, N','FontSize',12)
ylabel('Box Count, N(s)','FontSize',12)


% calculate Hausdorff Dimension
x2 = log(x);
y2 = log(y);

p2     = polyfit(x2,y2,1);
BestFit2 = polyval(p2,x2);

figure(4)
hold on
grid on
plot(x2,y2,      'bo','LineWidth',1)
plot(x2,BestFit2, 'b-','LineWidth',2)
xlabel('Number of blocks, log N','FontSize',12)
ylabel('Box Count, log N(s)'    ,'FontSize',12)
legend('First generation sample: 1.343', 'Second generation sample: 1.022')

HausdorffDimension = p2(:,1)
```

```
%%%%%%%%%%%
% Method of uploading, processing, and displaying raw data from LabVIEW
% email: p.french@ee.ucl.ac.uk
% web: www.ee.ucl.ac.uk/~pfrench
%%%%%%%%%%%

clear all
files = dir('lanode_Vs*.txt');

Va  = 0:5:250;
Vs  = 0:5:100;
Va_sweep_Vs=[];

for i = 1:length(files)
   eval(['DATA = load (''' files(i).name ''');'])
   Va_sweep_Vs = [Va_sweep_Vs DATA(length(Va)+1:length(DATA))];
end

[x,y] = meshgrid(Va, Vs);
z = Va_sweep_Vs';

% Filter and normalise image
windowSize = 4;
QQ     = filter(ones(1,windowSize)/windowSize,1,z)
rangeQQ = max(max(QQ)) - min(min(QQ));
QQ     = (QQ - min(min(QQ)))./rangeQQ;

figure(1)
contourf(x,y,QQ)
hold on
grid on
colorbar
xlabel('Anode Voltage (V)','FontSize',12)
ylabel('Substrate Voltage (V)','FontSize',12)
```

A.2. Publications arising from this thesis

Journal publications

D. M. Garner, G. Hui, A. Fung, and P. J. French, *Design of a CMOS-Compatible Field-Emission Magnetic Sensor with Adjustable Sensitivity*, Technical Digest of 16th International Vacuum Microelectronics Conference, pages 71-72, 2003.

D.M. Garner, P.J. French, G. Hui and A. Fund, *Design of complementary-metal-oxide-semiconductor-compatible field-emission magnetic sensor with adjustable sensitivity*, Journal Vacuum Science and Technology, B, 22, p. 1202, 2004

P. J. French, A. J. Kenyon and D. M. Garner, *A planar CMOS field-emission vacuum magnetic sensor,* IEEE Electron Device Letters, 2008 (submitted).

Conference publications

D. M. Garner, P. J. French and G. Ensell, *Field Emission Magnetic Sensors*, Nanomaterials and Nanomanufacturing Conference, University of Tokyo, 2003.

D. M. Garner and P. J. French, *Field Emission Magnetic Sensors*, IEEE Sensors Conference, University of Vienna, 2004.

D. M. Garner and P. J. French, *Practical Realisation of a Field-Emission-Based Magnetic Sensor*, International Vacuum Nanoelectronics Conference, 2004.

P. J. French and D. M. Garner, *Field-Emission Magnetic Sensors*, Postgraduate Research Conference in Electronics, Photonics, Communications & Networks, and Computing Science, University College London, 2004.

A. J. Kenyon, P. J. French, and D. M. Garner, *Field-Emission Magnetic Sensors*, Postgraduate Research Conference in Electronics, Photonics, Communications & Networks, and Computing Science, University College London, 2005.

Awards

P. J. French, *Field Emission Magnetic Sensors*, Annual Achievement Award given by the Worshipful Company of Scientific Instrument Makers, London, 2004.

P. J. French, *Field Emission for use in pressure sensing*, Annual Achievement Award given by the Worshipful Company of Scientific Instrument Makers, London, 2006.